

**Image-guided High Intensity Focused Ultrasound-based
Boiling Histotripsy for Treatment of Neuroblastoma**

Avinash Eranki

© copyright Avinash Eranki, Maastricht 2019

Printing: ProefschriftMaken || www.proefschriftmaken.nl

ISBN 978 94 6380 547 6

Image on the cover page shows neuroblastoma cells expressing PD-L1 after HIFU therapy

All rights reserved. No part of this publication may be reproduced, stored in a retrieval system or transmitted, in any form or by any means, electronic, mechanical, photocopying, recording or otherwise, without prior permission of the author or the copyright-owning journals for previous published chapters.

Image-Guided High Intensity Focused Ultrasound-based Boiling Histotripsy for Treatment of Neuroblastoma

Beeldgeleide, op hoge intensiteit gerichte,
op ultrageluid gebaseerde kookhistotripsie
voor de behandeling van neuroblastoom

(met een samenvatting in het Nederlands)

PROEFSCHRIFT

ter verkrijging van de graad van doctor aan de Universiteit Utrecht
op gezag van derector magnificus,
prof.dr. H.R.B.M. Kummeling,
ingevolge het besluit van het college voor promoties
in het openbaar te verdedigen op

woensdag 30 oktober 2019 des avonds te 6.00 uur

door

Avinash Eranki

geboren op 3 december 1984
te Ravulapalem, Andhra Pradesh, India

Promotor:

Prof. dr. C.T.W. Moonen

Copromotor:

Dr.M.G.Ries

Work presented in this dissertation is a combination of multiple manuscripts, supported in part or full by funding from these institutions and grants:

- Sheikh Zayed Institute for Pediatric Surgical Innovation, Children's National Medical Center.
- Joseph E. Robert, Jr. Center for Surgical Care, Children's National Medical Center.
- Center for Interventional Oncology and Intramural Research Program of the National Institutes of Health (NIH) and by NIH and National Cancer Institute grants ZID# BC011242, CL040015, and ZID BC 011242- 08.
- National Institutes of Health-NCI grant 1U01CA202947-01A1.

To my Mother, Father, and my Beloved Wife

Table of Contents

Chapter 1	
Introduction and thesis outline	13
1.1 Prevalence and staging of neuroblastoma	14
1.2 Immune characteristics of neuroblastoma	15
1.3 Treatment options for children with low and high-risk neuroblastoma	17
1.3.1 Surgical treatment of neuroblastoma	18
1.3.2 Minimally and non-invasive treatment options	18
1.4 Boiling histotripsy and immunotherapy for neuroblastoma therapy	21
1.5 References	24
Chapter 2	
Boiling histotripsy lesion characterization on a clinical magnetic resonance imaging-guided high intensity focused ultrasound system	29
2.1 Abstract	30
2.2 Introduction	31
2.3 Methods & materials	33
2.3.1 Experimental setup	33
2.3.2 Hydrophone measurements	34
2.3.3 Tissue mimicking phantom & <i>ex vivo</i> tissue preparation	35
2.3.4 MRI treatment planning and monitoring	36
2.3.5 HIFU sonication parameters	37
2.3.7 3d lesion segmentation	39
2.3.8 MRI temperature & thermal dose data analysis	40
2.3.9 Histology	40
2.3.10 Statistical analysis	40
2.4 Results	41
2.4.1 HIFU field assessment	41
2.4.2 Effect of BH sonication parameters on lesion volume	42
2.4.3 Effect of BH sonication parameters on temperature elevation	45
2.4.4 Comparing temperature dynamics at different locations at the focal zone	45
2.4.5 Effect of sonication parameters on focal temperature dynamics	47
2.4.6 Spatial temperature distribution at different sonication parameters	47

2.4.7 Boiling histotripsy lesions in <i>ex vivo</i> porcine tissues	51
2.5.1 Mri monitoring of <i>ex vivo</i> tissue destruction	55
2.5 Discussion	56
2.6 Conclusion	62
2.7 References	63
Chapter 3	
Mechanical fractionation of tissues using microsecond-long hifu pulses on a clinical mr-hifu system	67
3.1 Abstract	68
3.2 Introduction	69
3.3 Methods & materials	71
3.3.1 Experiment setup	71
3.3.2 <i>Ex vivo</i> tissue preparation	72
3.3.3 MRI-based sonication planning and monitoring	73
3.3.4 HIFU sonication parameters	73
3.3.5 Histology	75
3.3.6 Temperature & thermal dose data analysis	76
3.3.7 Statistical analysis	76
3.4 Results	77
3.4.1 Effect of sonication parameters on lesion appearance and structure	77
3.4.2 Tissue viability post sonication: comparison of H&E and vimentin staining	80
3.4.3 Dependence of tissue type on lesion production	82
3.4.4 Effect of sonication parameters on temperature and thermal dose	83
3.4.5 Changes in T2 relaxation time and lesion appearance on MRI	85
3.5 Discussion	87
3.6 Conclusion	92
3.7 References	94
Chapter 4	
Tissue-mimicking thermochromic phantom for characterization of HIFU devices and applications	97
4.1 Abstract	98
4.2 Introduction	99
4.3 Methods & materials	101
4.3.1 TMTCP preparation	101

4.3.2 Measurement of TMTCP properties	102
4.3.3 Characterization of TMTCP color change	103
4.3.4 Clinical and preclinical HIFU systems	103
4.3.5 Experimental setup and HIFU sonication parameters	105
4.3.6 MRI-based quantification of temperatures and T2 relaxation times	107
4.4 Results	108
4.4.1 Properties of TMTCP	108
4.4.2 Formulation dependence of TMTCP color change	109
4.4.3 Correspondence of TMTCP color change with MRI	111
4.4.4 TMTCP assessment on a preclinical us-HIFU system	113
4.4.5 TMTCP HIFU applications	115
4.5 Discussion	116
4.6 Conclusion	120
4.7 References	121
Chapter 5	
Mechanical hifu-triggered immune sensitization of refractory murine neuroblastoma for checkpoint inhibitor therapy	123
5.1 Abstract	124
5.2 Introduction	125
5.3 Methods & materials	127
5.3.1 Mouse neuroblastoma cell culture & checkpoint inhibitor antibodies	127
5.3.2 Study design	127
5.3.3 Ultrasound-guided HIFU tumor fractionation	128
5.3.4 Statistical analysis	129
5.3.5 Time to boil	129
5.3.6 ELISA	130
5.3.7 Flow cytometry	131
5.3.8 Immunohistochemistry	131
5.3.9 Gene expression & qRT-PCR	132
5.4 Results	133
5.4.1 HIFU in combination with act1a-4 + apd-l1 cures refractory, unilateral neuroblastoma tumors, leading to significant long-term survival	133
5.4.2 Local HIFU treatment alone induces systemic cellular, cytokine, and gene response	135

5.4.3 Systemic immune effects are sustained after HIFU in combination with actla-4 + apd-l1 and results in systemic 'abscopal' effect and, prolonged survival	141
5.4.4 HIFU mediated tumor fractionation combined with checkpoint inhibitor using actla-4 + apd-l1 induces effector memory cells	146
5.5 Discussion	148
5.6 Conclusion	151
5.7 References	152

Chapter 6

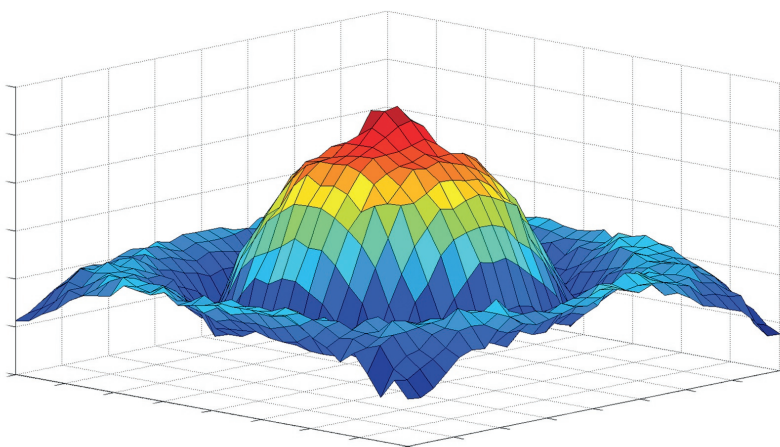
Technical aspects of osteoid osteoma ablation in children using MR-guided high intensity focused ultrasound

Technical aspects of osteoid osteoma ablation in children using MR-guided high intensity focused ultrasound	155
6.1 Abstract	156
6.2 Introduction	157
6.3 Methods & materials	158
6.3.1 Patients	158
6.3.2 MR imaging	158
6.3.3 MR-HIFU treatment	159
6.3.4 Technical feasibility assessment	160
6.4 Results	161
6.4.1 Technical feasibility	162
6.4.2 Patient positioning	162
6.4.3 Ultrasound coupling	163
6.4.4 Duration of the procedure and its components	163
6.4.5 Thermometry, energy and spatial definition of target	167
6.4.6 Near field heating/cooling	168
6.4.7 Treatment safety and imaging findings	171
6.5 Discussion	172
6.5.1 Technical feasibility	172
6.5.2 Design of MR-HIFU: tabletop	173
6.5.2 Choice of sonication power and duration	175
6.5.3 Initial safety findings and future directions	177
6.6 Conclusion	178
6.7 References	179

Chapter 7	
Summary and general discussion	181
Review committee	187
Acknowledgements	189
Publications	191
Author biography	193

Chapter 1

Introduction and Thesis Outline



1.1 Prevalence and Staging of Neuroblastoma

Prognosis for children and young adults with metastatic, relapsed, or refractory solid tumors remains unacceptably poor and has not improved significantly over the past three decades despite multimodality treatment including surgery, radiation, and chemotherapy¹⁻³. Neuroblastoma is a solid tumor that is presented as an embryonal tumor of the autonomous nervous system. The origin is thought to be a developing and incompletely differentiated precursor cells derived from neural-crest tissues⁴. Since this is a disease of developing tissues, neuroblastomas generally occur in very young children, with median age of 17 months at diagnosis⁵. The tumors arise in tissues of the sympathetic nervous system, most often in the adrenal medulla or paraspinal ganglia, and thus can present as mass lesions in the neck, chest, abdomen, or pelvis. Clinical presentation of neuroblastoma can be variable, ranging from an asymptomatic tumor to a primary tumor that causes critical illness because of local invasion, and oligometastatic disease. Current approaches have reached the limits of maximal dose intensification, and the acute and late effects of combination therapy are substantial¹. Recurrence at metastatic sites occurred in 60% to 95% of children with localized solid tumors after local therapy without the use of adjuvant chemotherapy⁶. The occurrence of local relapse in high-risk patients has unfavorable impact upon survival^{7,8}. The risk of toxicities during treatment and in an effort to prevent recurrence due to insufficient treatment could lead to undesirable impact on anti-cancer drug efficiency⁹. The staging system for neuroblastoma based on international neuroblastoma staging system (INSS)¹⁰. The INSS suggests complete surgical removal of neuroblastoma tumors that are visible for stage 1. However, there may be residual microscopic tumor residue post-surgery. In addition, in this stage the lymph nodes are unaffected, although nodes that are enclosed by the tumor may contain some tumor cells. In stage 2A, the cancer is localized to the area of origin and to one side of the body. Not all tumor can be removed by surgical excision. In this stage, lymph nodes outside the tumor are free of neuroblastoma cells.

Stage 2B is characterized by unilateral tumor, which may or may not be removed completely by surgical intervention. Proximal lymph nodes outside the tumor contain tumor-bearing cells, but the spread contained and not found in other lymph nodes. INSS stage 3 is described as tumor spread is still localized and not towards distant parts of the body. In addition, either the cancer cannot be surgically removed and crossed the midline of spine, or it has spread to contralateral lymph nodes relatively near to the tumor origin, or tumors are growing bilaterally and cannot be surgically excised. The terminal stage, stage 4, is characterized by spread of cancer cells to distal sites such as lymph nodes, bone marrow, liver, skin or other organs. The incidence of neuroblastoma is 10.2 cases per million children under 15 years of age; it is the most common cancer diagnosed during the first year of life ¹¹. For over a century, researchers have noted that neuroblastomas exhibit diverse with often debilitating clinical effects. As a consequence, neuroblastoma accounts for disproportionate morbidity and mortality among the cancers of childhood; counterintuitively, it is nevertheless associated with one of the highest proportions of spontaneous and complete regression of all human cancers ¹²⁻¹⁴. Outcomes in patients with neuroblastoma have improved, with 5-year survival rates increasing from 52% during the period from 1975 through 1977 to 74% during the period from 1999 through 2005, according to the Surveillance, Epidemiology, and End Results (SEER) databases ¹⁵. This improvement, however, is attributable mainly to increased cure rates among patients with the more benign form of the disease; the rates among children with high-risk neuroblastoma have shown only modest improvement, despite dramatic escalations in the intensity of therapy provided ¹⁶.

1.2 Immune Characteristics of Neuroblastoma

Active adaptive immunity against neuroblastoma has been challenging to obtain, especially in high-risk populations. This is primarily due to remarkably bulky primary and secondary tumors and their rapid proliferation, which overwhelms the child's underdeveloped immune system ^{17,18}. There is also a significant paucity of somatic mutations in these tumor

Chapter 1

making them poorly immunogenic. In addition, this type of tumor develops a sophisticated immunosuppressive microenvironment to evade effective T-cell immunity and function. Neuroblastoma cells evade T-cells and natural killer (NK) cells by down-regulating human leukocyte antigen (HLA) ¹⁹⁻²¹. Furthermore, NB tumor cells frequently express or release proteins to inhibit ²²⁻²⁴, and to kill, T-cells and NK cells²⁵. They additionally recruit tissue-specific macrophages to disable T-cell action²⁶. Neuroblastoma cell surface have been shown to have high levels of ganglioside and sialic acid-containing sugars and proteins²⁷, which have been demonstrated to be vital for migration, and metastasis. Innately occurring antibodies against neuroblastoma are rare, with the possible exception of IgM102. Natural anti-ganglioside antibodies *in vivo* are further rarer, thereby allowing these tumor cells to survive in circulation. Neuroblastoma tumors escape the immune system, entering sanctuaries such as the CNS, which is not directly accessible to circulating antibodies. In fact, the increasing frequency of relapses in CNS, lymphatic system, and bone marrow, demonstrate curative challenge even in the era of monoclonal antibody therapy²⁸. Anti- disialoganglioside (GD2) monoclonal antibody is an established treatment approach for children with neuroblastoma. GD2 belongs to a unique class of antigens that are independent of lymphocytes, consisting of membrane proximity, homogeneity within and across tumor cells²⁹, and over 5-6 million/cell are expressed on neuroblastoma cells, making it an attractive target for immunotherapy. Dinutuximab and Dinutuximab beta are anti-GD2 antibodies that are FDA approved and in second-line of treatment for high-risk neuroblastoma. Dinutuximab in combination with chemotherapy is also being explored as an alternative therapy (NCT01767194). Adoptive cell therapy using allogenic hematopoietic or bone marrow transplant is also used, however has seen substantial toxicities and found to be ineffective³⁰. Neuroblastoma cells evade traditional T-cell surveillance by downregulating MHC and costimulatory molecules on tumor cell surface³¹. Therefore, T-cell therapy approaches that are unhindered by lack of MHC-downregulation have are being considered as a viable therapeutic option. One the biggest challenges of immunotherapeutic treatment of neuroblastoma is

fundamentally pivoted on the lack of sufficient tumor mutations and presence of tumor specific antigens. Ability to release tumor specific antigen *in situ* could help improve the efficacy of immunotherapy against NB.

1.3 Treatment Options for Children with Low and High-Risk Neuroblastoma

Despite recent NB treatment advances, 50 to 60% of patients with high-risk neuroblastoma have a relapse, and to date there are no salvage treatment regimens known to be curative. Over the past decade, however, several highly active agents have been identified that may help such patients, and it appears likely that these treatments are increasing the number of patients whose survival is prolonged³². In contrast to the approach at the time of the initial diagnosis, when the focus is to provide intensive therapy within as short a time as feasible, the approach to relapse needs to focus on neuroblastoma as a chronic disease that can often be managed for years. Treatment of patients with neuroblastoma surviving after relapse is a delicate management for clinicians; it is necessary to offer hope for a cure but also to acknowledge that, at least until recently, long-term disease-free survival after a relapse was rarely seen, if ever. The hope lies in the possibility that recent advances in our understanding of the molecular basis of high-risk neuroblastoma have identified tractable therapeutic targets that may respond to novel agents with unprecedented antitumor activity when studied in the clinical setting. Therefore, approaches to maximize effects of current therapy without increasing acute and late effects are key in improving our current therapeutic approaches to these pediatric malignancies.

Patients with low- or intermediate-risk neuroblastoma have excellent outcomes³³, and a series of cooperative group trials evaluating reductions in therapy using risk-based treatment approaches for these children has led to decreased therapy-related toxicities and improved outcome^{34,35}. However, for patients with high-risk disease (patients with MYCN amplification and/or those >18 months of age with INRG Stage M disease) a multi-modal treatment may be

Chapter 1

needed^{32,35}. Currently, this includes surgery, chemotherapy followed by stem-cell harvest, myeloablative chemotherapy, radiation, and immunotherapy.

1.3.1 Surgical Treatment of Neuroblastoma

Although surgical resection of localized neuroblastoma alone yielded promising results in the LNESG1³⁴ and CCG studies³⁶, the risk of relapse in these patients were found to be higher in patients with MYCN amplification or other unfavorable histology³⁴. Supplementary treatment was suggested to be necessary in 10% of stage 1 patients and in 20% of Stage 2 patients with additional risk factors³⁴. Patients suffering from stage 3 disease, the approach of resection affects the survival outcomes³⁷. However, when the surgical resection is complete, there is a significant difference in the overall survival when compared to incomplete excision³⁷. In a single-institutional study at Memorial Sloan-Kettering Cancer Centre between 1991 -2007, total resection without damage or sacrifice of vital organs showed slightly improved survival in patients without MYCN amplification, as does a complete resection combined with chemotherapy. Patients with neuroblastoma expressing MYCN amplification required an intensified treatment of chemotherapy, surgery, radiotherapy, and immunotherapy to obtain a similar survival rate³⁸. This suggests that surgery alone is insufficient of managing and controlling neuroblastoma > stage 2.

1.3.2 Minimally and Non-Invasive Treatment Options

Most oncology approaches focus on therapies with little or no emphasis on tumor specific antigen release. Local and regional treatment approaches may circumvent this and control of oligometastatic disease could be achieved, with combinations with systemic immunotherapies such as checkpoint inhibitors, and T-cell therapies. Options for local treatment include both invasive surgical approaches and minimally invasive therapies. Minimally invasive therapies include radiofrequency (RFA)^{39,40}, cryo⁴¹, microwave⁴², laser ablation^{43,44}, and percutaneous ethanol injection^{45,46}, and irreversible electroporation⁴⁷. RFA and cryoablation have been used to treat different tumors in combination with different immunotherapeutic agents to treat cancer⁴⁸⁻⁵¹.

These ablative modalities, in some cases, have shown improved value as an adjuvant therapy to standard immunotherapy^{48,50}. Success of these ablative treatments are most often assessed by measuring the non-perfused volume post-treatment. These ablative methods are all invasive and sometimes need multiple punctures. This becomes a significant issue in pediatric patients, due to their size and iatrogenic effects^{52,53}. Non-invasive treatment methods such as high intensity focused ultrasound (HIFU) could overcome some of these issues. HIFU is a non-invasive technique that can noninvasively ablate target tissue with high spatial precision. HIFU is being explored for various clinical indications to improve management of local disease by reducing pain, risk of infection, collateral damage to intervening and surrounding tissues, and overall hospital costs. HIFU uses focused acoustic waves to deposit ultrasound energy within the target tissue location. Deposition of this ultrasound energy may have thermal and or mechanical effects. Thermal ablation is an approach which increases target tissue temperature to greater than 60°C and has been the most common method of tissue destruction using HIFU⁵⁴. This approach has been used to treat a wide variety of clinical indications such as uterine fibroids^{55,56}, liver tumors^{57,58}, kidney tumors^{57,59}, bone tumors^{60,61}, and prostate cancer^{62,63}. In addition to thermal ablation, HIFU has also been used to achieve mild hyperthermia (40–45°C)⁶⁴, which is currently under evaluation for local drug delivery strategies, and to cause mechanical destruction of tissue, also known as histotripsy⁶⁵⁻⁶⁷. Magnetic resonance imaging (MRI)⁶⁸ and ultrasound imaging⁶⁹ are currently used in planning, guiding, and monitoring HIFU ablation. Despite these advances in HIFU therapy, HIFU thermal ablation, similar to most of the other ablative techniques have limitations including heat-associated tissue fixation, loss of blood supply into the tumor, and denaturation of proteins and antigens⁷⁰. In addition, near-field heating and/or collateral damage of tissue adjacent to the treated region that may limit its clinical applicability⁷¹. While MR-thermometry may enable therapy planning and temperature feedback, heat diffusion and off-target heating may still cause iatrogenic effects^{63,72}. Furthermore, ablative temperatures may not be easily attainable in highly perfused organs without damage to intervening tissues. Treatment

Chapter 1

approaches that do not entirely rely on temperature-associated ablation may thus circumvent certain limitations of thermally ablative technologies, such as denaturation of tumor specific antigens and proteins.

Lately, HIFU methods termed cavitation histotripsy^{67,73,74} and boiling histotripsy (BH)^{75,76} have been used to mechanically disrupt target tissues, such as tumors. Unlike thermal HIFU that often uses continuous wave or high duty cycle pulsed wave ultrasound, histotripsy uses pulsed regimes at lower duty cycles. Cavitation histotripsy fractionates target tissues using a dense bubble cloud, created using microsecond-long pulses at higher pulse repetition frequency (PRF). This technique has been validated *in vitro* and *in vivo* for a variety of medical applications^{67,77,78}. However, cavitation histotripsy faces some challenges such as unexpected interruption of cavitation activity during the course of treatment due to the stochastic behavior⁷⁴. It may be valuable to develop HIFU mechanical fractionation techniques that are more predictable and controllable. BH is an alternative HIFU mechanical fractionation technique, which is more predictable compared to cavitation histotripsy⁷⁹. BH generates a submillimeter-sized boiling bubble, which upon collapse results in near instantaneous tissue emulsification. Unlike cavitation histotripsy, BH utilizes millisecond-long pulses, with lower PRF. The acoustic waves produce shock fronts that comprise of several high order harmonics of the fundamental frequency, leading to increased absorption of energy at the focal region, further enhancing heating to approximately 100°C in a few milliseconds. These localized and explosive boiling effects and its further interaction with subsequent shock fronts results in instantaneous tissue fractionation and necrosis⁶⁶. Since this explosive boiling takes place in the order of milliseconds, the impact of heat diffusion to surrounding tissues is minimal and resulting in negligible collateral thermal injury, allowing for greater spatial precision of the target tissue treatment. In addition, the fact that BH utilizes lower PRF, and longer pulse lengths, it is easily implemented on a clinical MR-HIFU system^{75,80}, compared to HIFU regimes using tens-of-microsecond-long pulse lengths, allowing for relatively

easier clinical translation. In addition, lower total temperature accumulation within the tumor, may help retain tumor specific antigens and proteins.

1.4 Boiling Histotripsy and Immunotherapy for Neuroblastoma Therapy

Immunotherapy promises unprecedented benefits to cancer patients. However, majority of cancer types including high-risk neuroblastoma remain immunologically unresponsive, due to the lack of *in situ* tumor-specific antigens. Lack of tumor specific antigen targets making these tumors unresponsive or 'cold' to immunotherapy, leading to poor therapeutic response, and outcomes. High intensity focused ultrasound (HIFU) is a non-invasive technique that can mechanically fractionate tumors potentially transforming immunologically 'cold' tumors into responsive 'hot' tumors. This thesis systematically develops novel BH sonication methods on a clinical HIFU system, laying a foundation to HIFU sonication parameters that can produce desired tissue-specific effects and explores its effect in a large, refractory neuroblastoma model. In addition, this thesis presents approaches to perform ultrasound-guided HIFU treatment-associated temperature characterization, and alternative approaches to treat pediatric patients with the existing MR-HIFU system.

Chapter 2 characterizes the effect of a broad BH sonication parameter sets using a clinical MR-HIFU system. One of the biggest obstacles of novel HIFU techniques to treat cancer is the inability to implement them into a clinical HIFU system, and clinical translate these innovative therapies. This makes clinical translation of newer HIFU technologies challenging. This chapter details the role of sonication-dependent fractionation and temperature effects in a tissue-mimicking phantom using a clinical MR-HIFU system.

Solid tumors can vastly vary in terms of their microstructure and mechanical properties, needing a tumor-specific sonication parameter set to obtain a suitable systemic immune response. Chapter 3 builds upon the knowledge from chapter 2, and details sonication parameter

Chapter 1

specific mechanical and thermal effects in liver, kidney and cardiac tissues, using a clinical MR-HIFU system.

While there was significant value addition to using MRI guidance in assessing BH-associated temperature changes, most academic, and research centers lack MRI access. In addition, MRI imaging can significantly add to patient-related costs, while BH can be performed via ultrasound imaging guidance, and therefore can be more practicable and relatively cheaper. Chapter 4 describes a novel thermochromic phantom that could circumvent some the issues associated with the lack of MRI thermometry, and allowing for volumetric temperature assessment post HIFU or BH sonications for systems relying on ultrasound imaging guidance for therapy planning and execution.

Based on the mechanical effects and type of lesion created, we further tested the effect of BH in a large, refractory murine neuroblastoma model using sonication parameters tested in chapters 2 and 3 in chapter 5. These sonication parameters are known to produce consistent tissue lysis, with sharp boundaries and little thermal effects, potentially leading to tumor-specific antigen release and systemic immune response. In addition, we used an ultrasound-guided system in this murine work (chapter 5), and tested the sonication parameter's temperature effects using the thermochromic phantom detailed in chapter 4. Chapter 5 details the effects of BH on the systemic immune response in a refractory murine neuroblastoma model, studying cellular, cytokine, and genetic changes before and after BH. In addition, this chapter details the effect of BH in combination with checkpoint inhibitors (α CTLA-4 and α PD-L1) in the systemic immune response and overall survival.

Chapter 6 demonstrates the ability to treat bone tumor using a clinical MR-HIFU system. Tumors that were located predominantly in the limbs were treat using this system. This study provided significant experience and knowledge in helping position patient with tumors that are not in the peritoneal space (HIFU system originally designed for treating uterine fibroids). This study

inform us in pediatric patient positioning for neuroblastoma treatments in the extremities and helps reduce overall treatment time.

Finally, chapter 7 summarizes BH methods for murine neuroblastoma treatment and provides future perspectives for clinical translation as well as suggestions for treating other tumors.

1.5 References

- 1 Fox, E. & Adamson, P. in *Handbook of anticancer drug development* (eds D Budman, A Calvert, & E Rowinsky) 309-318 (Lippincott Williams&Wilkins, 2003).
- 2 Ray, A. & Huh, W. W. Current state-of-the-art systemic therapy for pediatric soft tissue sarcomas. *Curr Oncol Rep* **14**, 311-319, doi:10.1007/s11912-012-0243-y (2012).
- 3 Esiashvili, N., Goodman, M. & Marcus, R. B., Jr. Changes in incidence and survival of Ewing sarcoma patients over the past 3 decades: Surveillance Epidemiology and End Results data. *J Pediatr Hematol Oncol* **30**, 425-430, doi:10.1097/MPH.0b013e31816e22f3 (2008).
- 4 Hoehner, J. C. *et al.* A developmental model of neuroblastoma: differentiating stroma-poor tumors' progress along an extra-adrenal chromaffin lineage. *Laboratory investigation; a journal of technical methods and pathology* **75**, 659-675 (1996).
- 5 London, W. *et al.* Evidence for an age cutoff greater than 365 days for neuroblastoma risk group stratification in the Children's Oncology Group. *Journal of clinical oncology* **23**, 6459-6465 (2005).
- 6 Adamson, P. C., Bagatell, R., Balis, F. M. & Blaney, S. in *Principles and Practice of Pediatric Oncology* Vol. 6th ed. (eds Phillip A. Pizzo & David G. Poplock) 279-336 (Lippincott Williams & Wilkins Health, 2011).
- 7 Singer, S., Corson, J. M., Gonin, R., Labow, B. & Eberlein, T. J. Prognostic factors predictive of survival and local recurrence for extremity soft tissue sarcoma. *Annals of surgery* **219**, 165-173 (1994).
- 8 Lewis, J. J., Leung, D., Heslin, M., Woodruff, J. M. & Brennan, M. F. Association of local recurrence with subsequent survival in extremity soft tissue sarcoma. *J Clin Oncol* **15**, 646-652 (1997).
- 9 Foote, M. The Importance of Planned Dose of Chemotherapy on Time: Do We Need to Change Our Clinical Practice? *Oncologist* **3**, 365-368 (1998).
- 10 Brodeur, G. M. *et al.* Revisions of the international criteria for neuroblastoma diagnosis, staging, and response to treatment. *Journal of clinical oncology* **11**, 1466-1477 (1993).
- 11 Ries, L. A. G. *et al.* Cancer incidence and survival among children and adolescents. *United States SEER Program 1975-1995* (1999).
- 12 Carlsen, N. How frequent is spontaneous remission of neuroblastomas? Implications for screening. *British journal of cancer* **61**, 441 (1990).
- 13 Everson, T. C. & Cole, W. H. Spontaneous regression of cancer: preliminary report. *Annals of surgery* **144**, 366 (1956).
- 14 Yamamoto, K. *et al.* Spontaneous regression of localized neuroblastoma detected by mass screening. *Journal of Clinical Oncology* **16**, 1265-1269 (1998).
- 15 Hayat, M. J., Howlader, N., Reichman, M. E. & Edwards, B. K. Cancer statistics, trends, and multiple primary cancer analyses from the Surveillance, Epidemiology, and End Results (SEER) Program. *The oncologist* **12**, 20-37 (2007).
- 16 Maris, J., Hogarty, M. & Bagatell, R. Vol. 369 2106–2120 (Lancet, 2007).
- 17 Cheung, N.-K. V. & Dyer, M. A. Neuroblastoma: developmental biology, cancer genomics and immunotherapy. *Nature Reviews Cancer* **13**, 397 (2013).
- 18 Brodeur, G. M. Neuroblastoma: biological insights into a clinical enigma. *Nature Reviews Cancer* **3**, 203 (2003).
- 19 Raffaghello, L. *et al.* Mechanisms of immune evasion of human neuroblastoma. *Cancer letters* **228**, 155-161 (2005).
- 20 Coughlin, C. M. *et al.* Immunosurveillance and survivin-specific T-cell immunity in children with high-risk neuroblastoma. *Journal of clinical oncology* **24**, 5725-5734 (2006).
- 21 Foreman, N., Rill, D., Coustan-Smith, E., Douglass, E. & Brenner, M. Mechanisms of selective killing of neuroblastoma cells by natural killer cells and lymphokine activated killer cells. Potential for residual disease eradication. *British journal of cancer* **67**, 933 (1993).
- 22 Castriconi, R. *et al.* Identification of 4Ig-B7-H3 as a neuroblastoma-associated molecule that exerts a protective role from an NK cell-mediated lysis. *Proceedings of the National Academy of Sciences* **101**, 12640-12645 (2004).
- 23 Morandi, F. *et al.* Bone marrow-infiltrating human neuroblastoma cells express high levels of calprotectin and HLA-G proteins. *PloS one* **7**, e29922 (2012).

- 24 Asgharzadeh, S. *et al.* Prognostic significance of gene expression profiles of metastatic neuroblastomas lacking MYCN gene amplification. *Journal of the National Cancer Institute* **98**, 1193-1203 (2006).
- 25 Shurin, G. V., Gerein, V., Lotze, M. T. & Barksdale Jr, E. M. Apoptosis induced in T cells by human neuroblastoma cells: role of Fas ligand. *Natural immunity* **16**, 263-274 (1998).
- 26 Liu, D. *et al.* IL-15 protects NKT cells from inhibition by tumor-associated macrophages and enhances antimetastatic activity. *The Journal of clinical investigation* **122**, 2221-2233 (2012).
- 27 Shochat, S. J., Abt, A. B. & Schengrund, C.-L. VCN-releasable sialic acid and gangliosides in human neuroblastomas. *Journal of pediatric surgery* **12**, 413-418 (1977).
- 28 Cheung, N.-K. V. *et al.* Murine anti-GD2 monoclonal antibody 3F8 combined with granulocyte-macrophage colony-stimulating factor and 13-cis-retinoic acid in high-risk patients with stage 4 neuroblastoma in first remission. *Journal of clinical oncology : official journal of the American Society of Clinical Oncology* **30**, 3264-3270, doi:10.1200/JCO.2011.41.3807 (2012).
- 29 Kramer, K. *et al.* Disialoganglioside G(D2) loss following monoclonal antibody therapy is rare in neuroblastoma. *Clinical Cancer Research* **4**, 2135-2139 (1998).
- 30 Matthay, K. *et al.* Comparison of autologous and allogeneic bone marrow transplantation for neuroblastoma. *Progress in clinical and biological research* **385**, 301-307 (1994).
- 31 Töpfer, K. *et al.* Tumor evasion from T cell surveillance. *BioMed Research International* **2011** (2011).
- 32 Esposito, M. R., Aveic, S., Seydel, A. & Tonini, G. P. Neuroblastoma treatment in the post-genomic era. *Journal of biomedical science* **24**, 14 (2017).
- 33 Park, J. R., Eggert, A. & Caron, H. Neuroblastoma: biology, prognosis, and treatment. *Pediatric clinics of North America* **55**, 97-120 (2008).
- 34 De Bernardi, B. *et al.* Treatment of localised resectable neuroblastoma. Results of the LNESG1 study by the SIOP Europe Neuroblastoma Group. *British journal of cancer* **99**, 1027 (2008).
- 35 Pinto, N. R. *et al.* Advances in risk classification and treatment strategies for neuroblastoma. *Journal of clinical oncology* **33**, 3008 (2015).
- 36 Perez, C. A. *et al.* Biologic variables in the outcome of stages I and II neuroblastoma treated with surgery as primary therapy: a children's cancer group study. *Journal of Clinical Oncology* **18**, 18-18 (2000).
- 37 Powis, M. R., Imeson, J. D. & Holmes, S. K. The effect of complete excision on stage III neuroblastoma: a report of the European Neuroblastoma Study Group. *Journal of pediatric surgery* **31**, 516-519 (1996).
- 38 Modak, S., Kushner, B. H., LaQuaglia, M. P., Kramer, K. & Cheung, N.-K. V. Management and outcome of stage 3 neuroblastoma. *European Journal of Cancer* **45**, 90-98 (2009).
- 39 Dupuy, D. E. *et al.* Percutaneous radiofrequency ablation of malignancies in the lung. *American Journal of Roentgenology* **174**, 57-59 (2000).
- 40 Gervais, D. A. *et al.* Radio-frequency Ablation of Renal Cell Carcinoma: Early Clinical Experience 1. *Radiology* **217**, 665-672 (2000).
- 41 Gill, I. S. *et al.* Renal cryoablation: outcome at 3 years. *The Journal of urology* **173**, 1903-1907 (2005).
- 42 Wright, A. S., Lee Jr, F. T. & Mahvi, D. M. Hepatic microwave ablation with multiple antennae results in synergistically larger zones of coagulation necrosis. *Annals of Surgical Oncology* **10**, 275-283 (2003).
- 43 Gangi, A. *et al.* Osteoid Osteoma: Percutaneous Laser Ablation and Follow-up in 114 Patients 1. *Radiology* **242**, 293-301 (2007).
- 44 Pacella, C. M. *et al.* Thyroid tissue: us-guided percutaneous interstitial laser ablation—a feasibility study 1. *Radiology* **217**, 673-677 (2000).
- 45 Ebara, M. *et al.* Percutaneous ethanol injection for the treatment of small hepatocellular carcinoma. Study of 95 patients. *Journal of gastroenterology and hepatology* **5**, 616-626 (1990).
- 46 Livraghi, T. *et al.* Hepatocellular carcinoma and cirrhosis in 746 patients: long-term results of percutaneous ethanol injection. *Radiology* **197**, 101-108 (1995).
- 47 Al-Sakere, B. *et al.* Tumor ablation with irreversible electroporation. *PloS one* **2**, e1135 (2007).
- 48 Cui, J. *et al.* Combination of radiofrequency ablation and sequential cellular immunotherapy improves progression-free survival for patients with hepatocellular carcinoma. *International journal of cancer* **134**, 342-351 (2014).

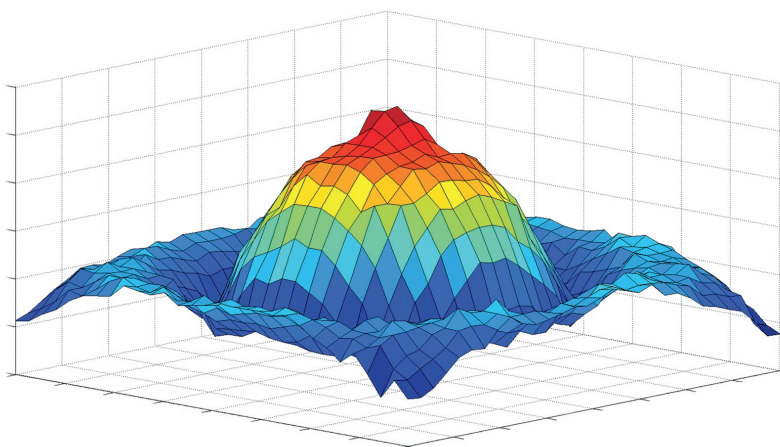
Chapter 1

- 49 Gameiro, S. R. *et al.* Combination therapy with local radiofrequency ablation and systemic vaccine enhances antitumor immunity and mediates local and distal tumor regression. *PLoS one* **8**, e70417 (2013).
- 50 Duffy, A. G. *et al.* Tremelimumab in combination with ablation in patients with advanced hepatocellular carcinoma. *Journal of hepatology* **66**, 545-551 (2017).
- 51 Waitz, R. *et al.* Potent induction of tumor immunity by combining tumor cryoablation with anti-CTLA-4 therapy. *Cancer research* **72**, 430-439 (2012).
- 52 Chin, J. L. *et al.* Results of salvage cryoablation of the prostate after radiation: identifying predictors of treatment failure and complications. *The Journal of urology* **165**, 1937-1942 (2001).
- 53 Rhim, H. *et al.* Radiofrequency Thermal Ablation of Abdominal Tumors: Lessons Learned from Complications 1. *Radiographics* **24**, 41-52 (2004).
- 54 Bailey, M., Khokhlova, V., Sapozhnikov, O., Kargl, S. & Crum, L. Physical mechanisms of the therapeutic effect of ultrasound (a review). *Acoustical Physics* **49**, 369-388 (2003).
- 55 Chapman, A. & Ter Haar, G. Thermal ablation of uterine fibroids using MR-guided focused ultrasound-a truly non-invasive treatment modality. *European radiology* **17**, 2505-2511 (2007).
- 56 Kim, Y.-s. *et al.* Volumetric MR-HIFU ablation of uterine fibroids: role of treatment cell size in the improvement of energy efficiency. *European journal of radiology* **81**, 3652-3659 (2012).
- 57 Illing, R. *et al.* The safety and feasibility of extracorporeal high-intensity focused ultrasound (HIFU) for the treatment of liver and kidney tumours in a Western population. *British journal of cancer* **93**, 890-895 (2005).
- 58 Kennedy, J. *et al.* High-intensity focused ultrasound for the treatment of liver tumours. *Ultrasonics* **42**, 931-935 (2004).
- 59 Watkin, N. A., Morris, S. B., Rivens, I. H. & Haar, G. R. t. High-intensity focused ultrasound ablation of the kidney in a large animal model. *Journal of Endourology* **11**, 191-196 (1997).
- 60 Chen, W. & Zhou, K. High-intensity focused ultrasound ablation: a new strategy to manage primary bone tumors. *Current Opinion in Orthopaedics* **16**, 494-500 (2005).
- 61 Huisman, M. *et al.* Feasibility of volumetric MRI-guided high intensity focused ultrasound (MR-HIFU) for painful bone metastases. *J Ther Ultrasound* **2**, b51 (2014).
- 62 Gelet, A. *et al.* Transrectal high-intensity focused ultrasound: minimally invasive therapy of localized prostate cancer. *Journal of Endourology* **14**, 519-528 (2000).
- 63 Poissonnier, L. *et al.* Control of prostate cancer by transrectal HIFU in 227 patients. *European urology* **51**, 381-387 (2007).
- 64 Partanen, A. *et al.* Mild hyperthermia with magnetic resonance-guided high-intensity focused ultrasound for applications in drug delivery. *International journal of hyperthermia* **28**, 320-336 (2012).
- 65 Canney, M. S., Khokhlova, V. A., Bessonova, O. V., Bailey, M. R. & Crum, L. A. Shock-induced heating and millisecond boiling in gels and tissue due to high intensity focused ultrasound. *Ultrasound in medicine & biology* **36**, 250-267 (2010).
- 66 Khokhlova, T. D. *et al.* Controlled tissue emulsification produced by high intensity focused ultrasound shock waves and millisecond boiling. *The Journal of the Acoustical Society of America* **130**, 3498-3510 (2011).
- 67 Vlaisavljevich, E. *et al.* Histotripsy-induced cavitation cloud initiation thresholds in tissues of different mechanical properties. *Ultrasonics, Ferroelectrics, and Frequency Control, IEEE Transactions on* **61**, 341-352 (2014).
- 68 Hesley, G. K., Gorny, K. R., Henrichsen, T. L., Woodrum, D. A. & Brown, D. L. A clinical review of focused ultrasound ablation with magnetic resonance guidance: an option for treating uterine fibroids. *Ultrasound quarterly* **24**, 131-139 (2008).
- 69 Wu, F. *et al.* Extracorporeal high intensity focused ultrasound ablation in the treatment of patients with large hepatocellular carcinoma. *Annals of surgical oncology* **11**, 1061-1069 (2004).
- 70 Van Leenders, G., Beerlage, H., Ruijter, E. T., De La Rosette, J. & Van De Kaa, C. Histopathological changes associated with high intensity focused ultrasound (HIFU) treatment for localised adenocarcinoma of the prostate. *Journal of clinical pathology* **53**, 391-394 (2000).
- 71 Hwang, J. H. *et al.* Preclinical in vivo evaluation of an extracorporeal HIFU device for ablation of pancreatic tumors. *Ultrasound in medicine & biology* **35**, 967-975 (2009).
- 72 Chaussy, C. & Thüroff, S. Results and side effects of high-intensity focused ultrasound in localized prostate cancer. *Journal of Endourology* **15**, 437-440 (2001).

- 73 Xu, J., Bigelow, T. A. & Whitley, E. M. Assessment of ultrasound histotripsy-induced damage to ex vivo porcine muscle. *Journal of ultrasound in medicine : official journal of the American Institute of Ultrasound in Medicine* **32**, 69-82 (2013).
- 74 Xu, Z., Hall, T. L., Fowlkes, J. B. & Cain, C. A. Effects of acoustic parameters on bubble cloud dynamics in ultrasound tissue erosion (histotripsy). *The Journal of the Acoustical Society of America* **122**, 229-236 (2007).
- 75 Eranki, A. *et al.* Boiling histotripsy lesion characterization on a clinical magnetic resonance imaging-guided high intensity focused ultrasound system. *PloS one* **12**, e0173867 (2017).
- 76 Khokhlova, V. A. *et al.* Histotripsy methods in mechanical disintegration of tissue: Towards clinical applications. *International Journal of Hyperthermia* **31**, 145-162 (2015).
- 77 Hall, T. L. *et al.* Histotripsy of rabbit renal tissue in vivo: temporal histologic trends. *Journal of Endourology* **21**, 1159-1166 (2007).
- 78 Xu, Z., Owens, G., Gordon, D., Cain, C. & Ludomirsky, A. Noninvasive creation of an atrial septal defect by histotripsy in a canine model. *Circulation* **121**, 742-749 (2010).
- 79 Simon, J. C. *et al.* Ultrasonic atomization of tissue and its role in tissue fractionation by high intensity focused ultrasound. *Physics in medicine and biology* **57**, 8061 (2012).
- 80 Partanen, A. *et al.* in *International Symposium for Therapeutic Ultrasound*.

Chapter 2

Boiling histotripsy lesion characterization on a clinical magnetic resonance imaging-guided high intensity focused ultrasound system



This chapter is based on:

Eranki, Avinash, et al. "Boiling histotripsy lesion characterization on a clinical magnetic resonance imaging-guided high intensity focused ultrasound system." *PloS one* 12.3 (2017): e0173867.

Eranki, Avinash, et al. "Volumetric and Thermal Characterization of Boiling Histotripsy Lesions Based on a Clinical MR-HIFU System" *International Symposium for Therapeutic Ultrasound* (2016).

Chapter 2

2.1 Abstract

Purpose: High intensity focused ultrasound (HIFU) is a non-invasive therapeutic technique that can thermally ablate tumors. Boiling histotripsy (BH) is a HIFU approach that can emulsify tissue in a few milliseconds. Lesion volume and temperature effects for different BH sonication parameters in tissue-mimicking phantoms are currently not well characterized. In this work, lesion volume, temperature distribution, and area of lethal thermal dose were characterized for varying BH sonication parameters in tissue-mimicking phantoms (TMP) and demonstrated in ex vivo tissues.

Methods: The following BH sonication parameters were varied using a clinical MR-HIFU system (Sonalleve V2, Philips, Vantaa, Finland): acoustic power, number of cycles/pulse, total sonication time, and pulse repetition frequency (PRF). A 3×3×3 pattern was sonicated inside TMP's and ex vivo tissues. Post sonication, lesion volumes were quantified using 3D ultrasonography and temperature and thermal dose distributions were analyzed offline. Ex vivo tissues were sectioned and stained with H&E post sonication to assess tissue damage.

Results: Significant increase in lesion volume was observed while increasing the number of cycles/ pulse and PRF. Other sonication parameters had no significant effect on lesion volume. Temperature full width at half maximum at the end of sonication increased significantly with all parameters except total sonication time. Positive correlation was also found between lethal thermal dose and lesion volume for all parameters except number of cycles/pulse. Gross pathology of ex vivo tissues post sonication displayed either completely or partially damaged tissue at the focal region. Surrounding tissues presented sharp boundaries, with little or no structural damage to adjacent critical structures such as bile duct and nerves.

Conclusion: Our characterization of effects of HIFU sonication parameters on the resulting lesion demonstrates the ability to control lesion morphologic and thermal characteristics with a clinical MR-HIFU system in TMP's and ex vivo tissues. We demonstrate that this system can produce

spatially precise lesions in both phantoms and ex vivo tissues. The results provide guidance on a preliminary set of BH sonication parameters for this system, with a potential to facilitate BH translation to the clinic.

2.2 Introduction

The current standard of care in treatment of benign and malignant tumors involves a multimodal approach¹. While most oncology approaches focus on systemic therapies, local and regional control may be important in the case of oligometastatic disease, locally contained disease, and potential future combinations with systemic immunotherapies such as checkpoint inhibitors. Options for local treatment include both invasive surgical approaches and minimally invasive therapies. Minimally invasive therapies include radiofrequency (RF)^{2,3}, cryo⁴, microwave (MW)⁵, and laser ablation^{6,7}, and percutaneous ethanol injection^{8,9}. However, even minimally invasive techniques risk collateral tissue damage and procedure-related complications¹⁰⁻¹⁴. Treatment approaches that are effective, non-invasive, spatially precise, and relatively quick to perform have the potential to improve management of local disease by reducing pain, risk of infection, collateral damage to intervening and surrounding tissues, and overall hospital costs.

One non-invasive technique that can address shortcomings of invasive approaches for local therapy is high intensity focused ultrasound (HIFU). HIFU uses acoustic waves to precisely focus ultrasound energy within the body. Deposition of this ultrasound energy may have mechanical and thermal effects. Thermal ablation (>60°C) increases tissue temperature at the focal zone and has been the most common method of tissue destruction using HIFU¹⁵. This approach has been used to treat a wide variety of tumors including uterine fibroids^{16,17}, liver tumors^{18,19}, kidney tumors^{18,20}, bone tumors^{21,22}, and prostate cancer^{23,24}. In addition to thermal ablation, HIFU has also been used to achieve mild hyperthermia (40-45°C)^{25,26} and to cause mechanical destruction of tissue, also known as histotripsy²⁷. Magnetic resonance imaging (MRI)²⁸⁻³⁰ and ultrasound imaging^{31,32} are currently used in planning, guiding, and monitoring HIFU

Chapter 2

therapies. Despite real-time monitoring methods such as MRI thermometry, HIFU thermal ablation has limitations including near field heating or collateral damage of tissue adjacent to the treated region that may limit its clinical applicability³³. While MR-thermometry may provide both therapy monitoring and closed loop feedback control³⁴, heat diffusion and off-target heating may cause iatrogenic peri-target tissue injury^{24,35}. Furthermore, ablative temperatures may not be easily attainable in highly perfused organs without damage to intervening tissues. Treatment approaches that do not entirely rely on temperature rise may thus circumvent certain limitations of HIFU thermal ablation.

Recently, HIFU methods termed cavitation histotripsy^{36,37} and boiling histotripsy (BH)^{38,39} have been used to create mechanical disruption of tissue. Unlike traditional HIFU thermal ablation that typically uses continuous wave or high duty cycle pulsed wave ultrasound, histotripsy employs pulsing regimes at much lower duty cycles (even lower than conventional 10-20% duty cycle “pulsed HIFU”). Cavitation histotripsy fractionates tissue via a dense bubble cloud, created using microsecond-long pulses at high pulse repetition frequency (PRF). This technique has been demonstrated *in vitro* and *in vivo* for a variety of medical applications^{36,40-42}. However, cavitation histotripsy has several challenges such as unexpected interruption of cavitation activity during the course of treatment due to the stochastic behavior³⁷. It is therefore important to develop histotripsy methods that are more predictable and controllable.

BH is a more predictable technique compared to cavitation histotripsy³⁸. BH generates a millimeter-size boiling bubble, causing near instantaneous tissue emulsification. Unlike cavitation histotripsy, BH employs millisecond-long pulses, with lower PRF. In this method, high amplitude acoustic wave creates a boiling bubble at the focus. This wave also produces shock fronts consisting of several high order harmonics of the fundamental frequency, causing increased absorption of energy and further enhancing heating to approximately 100°C in milliseconds. This highly localized explosive boiling and its further interaction with subsequent shock fronts results in instant tissue death. Since this explosive boiling takes place in the order of milliseconds, the

impact of heat accumulation is minimal and results in negligible collateral thermal injury, thereby potentially allowing for greater spatial precision of the treatment.

Currently, no clinical HIFU system has been characterized to accurately study the effects of various BH parameters, an important step to facilitate translation of BH to the clinic. The purpose of this study was to characterize lesion volume, temperature distribution, and thermal dose using BH delivered by a commercially available clinical MRI-guided HIFU system (MR-HIFU) in both tissue-mimicking gel phantoms and in *ex vivo* porcine liver and cardiac muscle.

2.3 Methods & Materials

2.3.1 Experimental Setup

A clinical HIFU system (Sonalleve V2, Philips, Vantaa, Finland) integrated with a MRI scanner (Achieva 1.5T, Philips, Vantaa, Finland) was used to perform the BH experiments. The system is capable of accurately delivering acoustic energy, and consists of a generator cabinet and a patient tabletop that houses an ultrasound transducer attached to a positioning system with 5 degrees of freedom, submerged in a sealed oil tank. Both the transducer positioning and the generators are controlled using a dedicated therapy planning console. The transducer is a 256-element spherical shell phased array operating at 1.2 MHz and with a focal length of 14 cm. The ultrasound beam propagates through a sealed acoustically hypoechoic window and produces an ellipsoidal focal point of approximately $1.6 \times 1.6 \times 10$ mm in size (-6 dB of positive pressure)²⁶. The MR-HIFU system also includes MRI receive coils, consisting of two integrated elements within the tabletop and a three-element pelvic coil.

The overall arrangement used for the BH experiment is depicted in Fig 1. A cylindrical water bath filled with deionized and degassed water at room temperature (23°C) and sealed with an acoustically hypoechoic Mylar membrane on one end was placed on an acrylic base plate designed to position the water bath over the acoustic window. A custom, 3D-printed phantom holder was designed to position a phantom within the water bath. The holder consisted of a plastic

box with openings at the bottom and top surfaces to facilitate sonication and exiting beam path. The phantom material was inserted into this plastic holder, and removed after each experiment. An acoustic absorber pad was placed 2 cm from the top of the phantom holder to prevent reflections within the water bath.

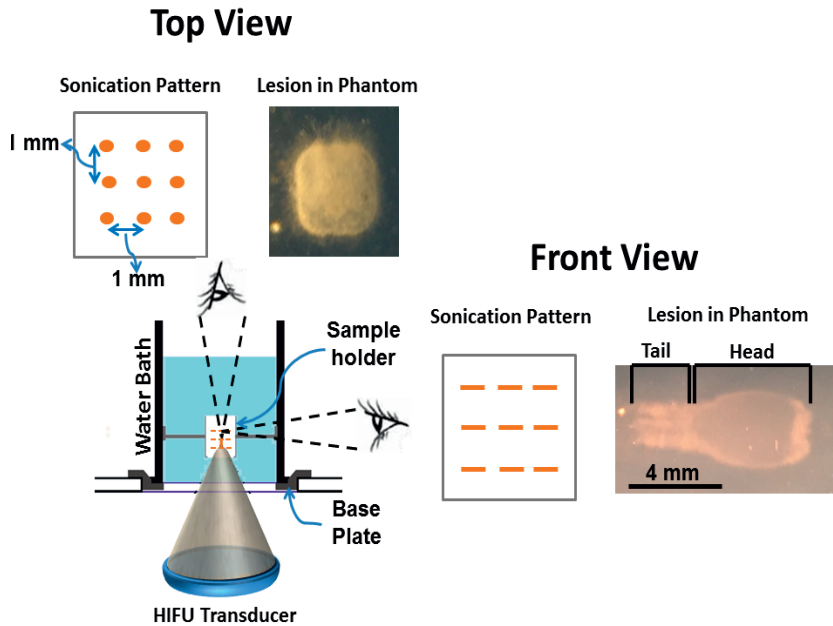


Fig 1. Diagram showing the experimental setup used to produce BH lesions on a clinical MR-HIFU system in both tissue mimicking phantom and ex vivo tissue. The setup consists of a water bath, filled with degassed water. This water bath was placed on an acoustically hypoechoic membrane. This membrane made it possible for the HIFU beam to pass through and into the water bath. The sonication pattern is a $3 \times 3 \times 3$ cube with 1 mm spacing between each point in either direction. The lesion in top view, looks like a square, and appears 'tad-pole' shaped in any plane parallel to the HIFU beam.

2.3.2 Hydrophone Measurements

Hydrophone measurements were made across a range of power levels to assess changes in acoustic pressures. A custom-made water tank with an inner diameter of 260 mm and

a height of 610 mm was placed on top of the patient table and filled with deionized and degassed water. A fiber optic hydrophone (HFO-690, Onda Corporation, Sunnyvale, CA, USA) was attached to a 3-D positioner (Velmex Inc., Bloomfield, NY, USA). A custom MATLAB (MathWorks, Natick, MA, USA) program was used to control the 3-D positioner, acquire hydrophone signals using a digitizer (Gage Applied Technologies Inc., Lockport, IL, USA), synchronize data acquisition, and process the acquired data. The HIFU system was controlled to generate ultrasound pulses with different acoustic powers (500, 550, 600, or 650 W) at 1.2 MHz frequency, 10 Hz PRF, and 40 cycles/pulse. The lower power threshold was selected based on the ability to produce repeatable lesions at the lowest acoustic power, while the higher power threshold was selected to ensure the continuous safe operation of the HIFU transducer. The 3-D positioner was controlled to locate the HIFU focus, and three repeated pressure measurements were performed at the focus for each power value to obtain average peak positive and peak negative pressure values.

2.3.3 Tissue Mimicking Phantom & *Ex Vivo* Tissue Preparation

Tissue mimicking phantoms for *in vitro* histotripsy lesion volume characterization experiments were prepared as previously reported⁴³⁻⁴⁵. Briefly, a commercially available aqueous solution of acrylamide bisacrylamide (40% w/v) with a feed ratio of acrylamide/ bisacrylamide 19:1, was mixed with degassed water and placed in a vacuum chamber for 15-20 minutes. Then, the solution was mixed with tetramethylethylenediamine (TEMED) and ammonium persulfate (APS) solution, immediately transferred to rectangular containers (6 × 6 × 10 cm) to match the phantom holder size, and left to cure at room temperature. The density of this phantom material was measured to be 1.0200 ± 0.0014 g/cm³ using a commercially available apparatus (density kit for XS precision balances, Mettler Toledo, Columbia, MD, USA), i.e., within the range of healthy human liver and spleen tissues⁴⁶. Additionally, the formulation of our phantom is similar to the one reported previously by Zell *et al.*⁴⁷. Therefore, the attenuation and speed of sound of our

Chapter 2

tissue mimicking phantom closely matches 0.7 ± 0.1 dB/cm at 5MHz and $1.58 \pm 0.03 \times 10^3$ m/s respectively.

Tissues were obtained after euthanasia of a healthy adult 150 kg pig on an unrelated Animal Care and Use Committee approved protocol of the National Institutes of Health. Liver and cardiac muscle tissues were obtained within one hour and samples immediately prepared to fit the tissue holder. These tissues were selected due to their diverse structural organization and biochemical composition. Values of attenuation of the liver and cardiac muscle tissue were derived from literature for calculations (0.676 and 0.8 dB/cm/MHz, respectively)⁴⁸. The prepared tissues were transported in a bag of phosphate buffered saline (PBS, 1x) on ice. This approach retains tissue function and viability for up to three days⁴⁹. All tissue samples were degassed for two hours in a vacuum desiccant chamber. Once degassed, the tissues were again placed in PBS on ice and transported to the MRI suite.

2.3.4 MRI Treatment Planning and Monitoring

After positioning the sample and absorber pad within the water bath and strapping the pelvic coil over the bath, a survey scan was performed to localize the phantom (Turbo Field Echo (TFE) 3D; field of view (FOV): $300 \times 300 \times 120$ mm³; voxel Size: $1.46 \times 1.73 \times 12$ mm³; stacks: 2; number of slices 12/5). This scan was followed by susceptibility sensitive 3D steady state fast field echo (FFE) sequence; repetition time (TR)/echo time (TE): 150/15 ms; FOV: $280 \times 280 \times 25$ mm³; voxel size: $1.2 \times 1.2 \times 2.5$ mm³; acquisition time: 76 seconds) to check for air bubbles in the ultrasound beam path. HIFU exposures were planned on a T2-weighted image set acquired using an FFE pulse sequence ; TR/TE: 680/35 ms; flip angle (FA): 20°; FOV: $250 \times 250 \times 75$ mm³; voxel size: $1.2 \times 1.3 \times 1.5$ mm³; parallel imaging (SENSE) factor: 2 (in RL direction); orientation: coronal; slices 20; acquisition time: 12 min). T1W image set was acquired prior to start of the sonication (number of signal averages (NSA) = 2; 3D FFE ; FOV: $200 \times 250 \times 81$ mm³; Voxel size: $1.3 \times 1.5 \times 1.3$ mm³; TR/TE: 20/4.6 ms). The MRI temperature mapping sequence was a 2D echo planar

FFE (FFE-EPI) pulse sequence (TR/TE: 36/19 ms; EPI factor = 11; FA = 20°; FOV = 160 × 121 mm²; voxel size = 2.5 × 2.5 × 7 mm³; 4 slices: 3 coronal and 1 sagittal; dynamic scan time = 1.8 s. Temperature and thermal dose maps were calculated in real time using the MRI phase images and the proton resonance frequency shift (PRFS) thermometry method ⁵⁰, overlaid over the magnitude images, and displayed on the therapy planning console. For the *ex vivo* experiments, the T2W and T1W MRI sequences were repeated post HIFU to visualize and characterize the lesions.

2.3.5 HIFU Sonication Parameters

Sonication planning was performed on the therapy planning console based on MR images. A location 30 mm deep within the phantom or tissue was selected to produce a pattern consisting of 27 locations spatially separated by 1 mm (in between each focal point), in a 3 × 3 × 3 grid. A schematic figure of planned sonication pattern is shown in Fig 1. To relate the experiments conducted at room temperature to *in vivo* studies, reference temperature for MR-thermometry was set to 37.5°C, and temperature was calculated relative to this baseline temperature. The sonication parameters used in TMP's are detailed in Table 1.

Ex vivo porcine liver and cardiac tissues were sonicated with the following parameters:

- i. 5 Hz PRF, 600 W and 15,000 cycles/pulse
- ii. 1 Hz PRF, 600 W and 20,000 cycles/pulse

Chapter 2

Table 1. List of all sonication parameters used in BH characterization experiments. Four sonication parameters were selected for this experimental study. While each of these parameters are varied (in bold font), other three parameters are kept constant.

Acoustic Power (W)	Number of cycles/pulse	Pulse Length (ms)	Total Sonication Time (seconds)	Pulse Repetition Frequency (Hz)
500	15,000	12.5	902	1
550				
600				
650				
600	10,000	8.3	~902	1
	12,000	10		
	14,000	11.6		
	16,000	13.3		
	18,000	15		
	20,000	16.6		
600	15,000	12.5	137	1
			274	
			410	
			574	
			684	
			820	
600	16,000	13.3	800	0.5 (0.66% DC^a)
			400	1 (1.33% DC)
			200	2 (2.66% DC)
			133	3 (4.00% DC)
			100	4 (5.33% DC)
			80	5 (6.66% DC)

^aDC = Duty Cycle. The cube was sonicated 15 times while varying PRF.

2.3.6 Estimating Time-to-Boil

The parameter time-to-boil was estimated for all acoustic powers applied in our experiments. The ultrasound waves at the focus induced heating, the rate of which can be calculated using weak shock theory ⁵¹:

$$H = \frac{\beta f_o A_s^3}{6\rho_o^2 c_o^4}$$

where H is the heating rate, f_o is the ultrasound frequency, A_s is the *in situ* shock amplitude, ρ_o is the density of the medium and c_o is the speed of sound. If the heating rate is sufficiently high, the effect of heat conduction to surrounding regions can be low and neglected. Using the heating rate, the time-to-boil can be calculated as:

$$t_b = \frac{\Delta T c_v}{H}$$

where ΔT is the difference between 100°C and local temperature and c_v is the heat capacity/volume. We used the following constants to calculate both heating rate and time-to-boil in the tissue-mimicking phantom: $\beta = 4$, $f_o = 1.2$ MHz, $\rho_o = 1.02$ g/cm³, $c_o = 1544$ m/s, $c_v = 5.3 \times 10^6$ J/m³/°C.

2.3.7 3D Lesion Segmentation

Post sonication, the lesions were individually scanned using a clinical diagnostic ultrasound scanner (iU22, Philips, Bothell, WA, USA) equipped with a 3D transducer (X6-1) with elements arranged in a matrix array, operating at 6 MHz. All phantoms were oriented along the same direction with respect to the transducer during scanning. An acoustic absorber pad was placed under each phantom to prevent reverberation. Post scanning, 3D DICOM images of the lesions were stored for further analysis, and the phantoms were bisected along the beam axis (MRI sagittal plane) to observe gross damage. A semiautomatic segmentation software (TurtleSeg, The University of British Columbia, Canada) based on gradient magnitude, gradient direction, and Canny edge detection, was used to obtain lesion volumes ^{52,53}. Briefly, sparse

Chapter 2

number of slices along the sagittal plane was manually contoured and the software was able to automatically connect the remaining slices to provide a lesion volume estimate.

2.3.8 MRI Temperature & Thermal Dose Data Analysis

The MRI temperature maps were analyzed using MATLAB (MathWorks, Natick, MA, USA). A 40 × 30 mm region of interest (ROI) was centered on the targeted region and the maximum temperature values within this ROI were obtained over the entire duration of the sonication. Full width at half maximum (FWHM) of temperature elevation was calculated as a standardized quantitative measure of temperature distribution within the ROI. Cumulative equivalent minutes at 43°C (CEM43) was used as a metric for thermal dose assessment since it correlates well with thermal tissue damage^{54,55}. Area of thermal dose >240 CEM43 was computed for every sonication in tissue mimicking phantom.

2.3.9 Histology

Post sonication, the tissues were fixed in 10% neutral buffered formalin for histological processing. Tissues were embedded with paraffin and sectioned perpendicular to the HIFU beam path, into 5µm thick slices. Subsequently, tissues were stained with hematoxylin and eosin (H&E) and imaged at 4x, 10x, and 40x magnification (Olympus BX 51-P, Waltham, MA, USA).

2.3.10 Statistical Analysis

Quantitative results were reported as mean ± standard deviation (SD) for all experiments conducted on tissue mimicking phantoms (N = 3 each sonication parameter). Comparisons amongst parameter groups were performed using one way ANOVA subject to Bonferroni correction using GraphPad Prism (Version 5.01, GraphPad Software Inc., La Jolla, CA). For all tests, two tailed p-values were obtained, and differences were considered significant if p≤0.05. Correlation was performed between variables and Pearson's coefficient was computed.

2.4 Results

2.4.1 HIFU Field Assessment

Acoustic pressures were measured at four acoustic power levels. Increasing acoustic power from 500 W to 650 W increased peak positive pressure from 65.97 to 76.26 MPa and reduced peak negative pressure from -10.98 to -12.16 MPa (Fig 2, Table 2). High pressure shock fronts become more noticeable with increasing power. This in turn reduced the time-to-boil, causing quicker heating and breakdown of tissue. Increase in these shock fronts also enhances the heating rate⁵¹.

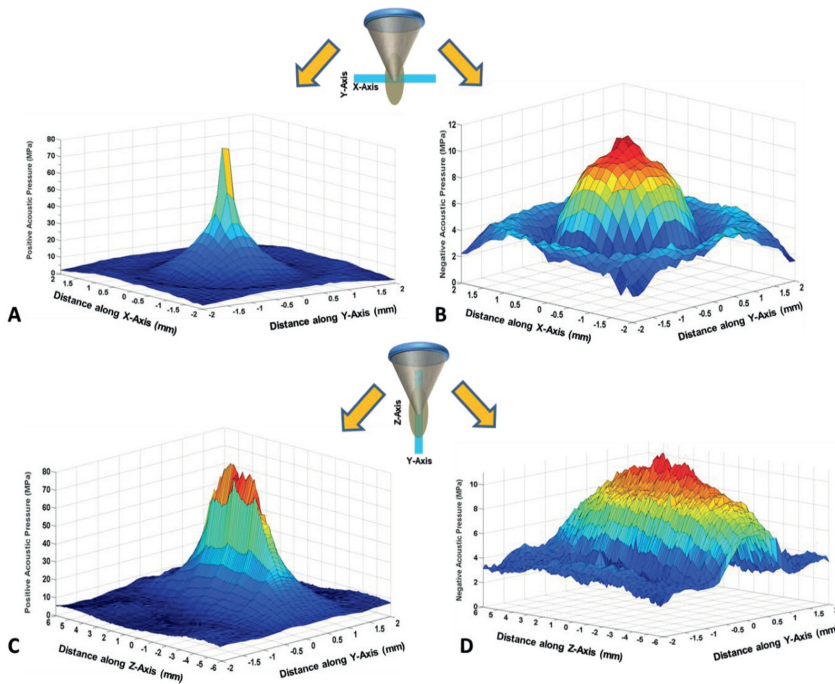


Fig 2. HIFU positive and negative pressure waveforms displayed in 3D at 500 W (free field), across (A & B) and along (C & D) the plane of the HIFU beam propagation. At this acoustic power, the peak positive pressure was 65.97 ± 4.42 and peak negative pressure of 10.98 ± 0.45 . Additionally, the beam width along the HIFU beam propagation is greater than the across the HIFU beam axis.

Chapter 2

Table 2. Peak positive and negative pressures measured at varying acoustic powers using a fiber optic hydrophone.

Acoustic Power (W)	Peak Positive Pressure (MPa)	Peak Negative Pressure (MPa)
500	65.97±4.42	10.98±0.45
550	70.20±4.81	10.65±0.86
600	72.65±4.53	10.98±0.76
650	76.26±5.67	12.16±0.70

2.4.2 Effect of BH Sonication Parameters on Lesion Volume

Sonications were performed while varying parameters (Table 1) to examine their effects on lesion volume in tissue mimicking phantoms and in *ex vivo* tissue. The time-to-boil was estimated to be 5.45, 4.70, 4.25, and 3.59 ms for acoustic powers of 500, 550, 600, and 650 W, respectively. Resulting lesions were mechanically fractionated and had a characteristic 'tadpole' shape with all tested parameters as seen in Fig 1. Lesions created with sonication parameters greater than 12,000 cycles/pulse, 550 W, 1 Hz, and 274 seconds resulted in a void filled with semi solid phantom debris at the focal zone, with little or no fractionation outside this region. Other parameters resulted in minimal fractionation of the phantom material at the focal zone, also with little or no damage outside this region.

Acoustic Power

Upon gross visual analysis, the lesions appeared to increase in size with increasing acoustic power. Based on 3D ultrasound data, the average lesion volume increased linearly ($R^2 = 0.71$), from $1180 \pm 150 \text{ mm}^3$ to $1440 \pm 180 \text{ mm}^3$ as acoustic power increased from 500 to 650 W (Fig 3a), though one way ANOVA revealed no significant differences in lesion volumes (overall ANOVA $p = 0.106$).

Number of Cycles/Pulse

Across the studied range of cycles/pulse, linear increase ($R^2 = 0.86$) in lesion volume was obtained with overall significant difference (overall ANOVA $p = 0.0025$, Fig 3b). Lesion volume ($1080 \pm 140 \text{ mm}^3$) obtained at 10,000 cycles/pulse differed significantly from volumes obtained at both 18,000 and 20,000 cycles/pulse ($1640 \pm 180 \text{ mm}^3$ and $1780 \pm 140 \text{ mm}^3$, $p \leq 0.05$ and $p \leq 0.01$, respectively.). Lesion volumes were similar for 12,000, 14,000, and 16,000 pulses/pulse at 1450 ± 190 , 1460 ± 160 , and $1480 \pm 80 \text{ mm}^3$, respectively ($p > 0.05$).

Total Sonication Time

The 27-point cubical pattern (Fig 1) was sonicated 5 to 30 times, thus varying the total sonication time. Visual inspection of slices perpendicular to the beam axis revealed three distinct planes of nine point lesions for both 137 and 274-second long sonications. Longer total sonication times resulted in lesions that resembled a single large void. The entire lesion had a 'tadpole' shape along the beam axis for all total sonication times. Across the range of sonication times, lesion volumes increased linearly ($R^2 = 0.74$) from $1020 \pm 140 \text{ mm}^3$ to $1490 \pm 230 \text{ mm}^3$, though without significant differences (overall ANOVA, $p = 0.076$, Fig 3c).

Pulse Repetition Frequency (PRF)

With all other sonication parameters kept constant, measurements of lesion volume exhibited significant differences with varying PRF (ANOVA $p \leq 0.0001$, Fig 3d). Following sonications at 4 and 5 Hz PRF, the lesion head consisted of liquefied phantom debris. Lesion volumes increased linearly ($R^2 = 0.97$) with increasing PRF. Pairwise comparisons reveal similar lesion volumes for 0.5 and 1 Hz, 0.5 and 2 Hz, 1 and 2 Hz, 2 and 3 Hz, and between 3 and 4 Hz PRF ($p > 0.05$). All other lesion volume comparisons resulted in significant differences ($p \leq 0.05$), as seen in Fig 3d.

Chapter 2

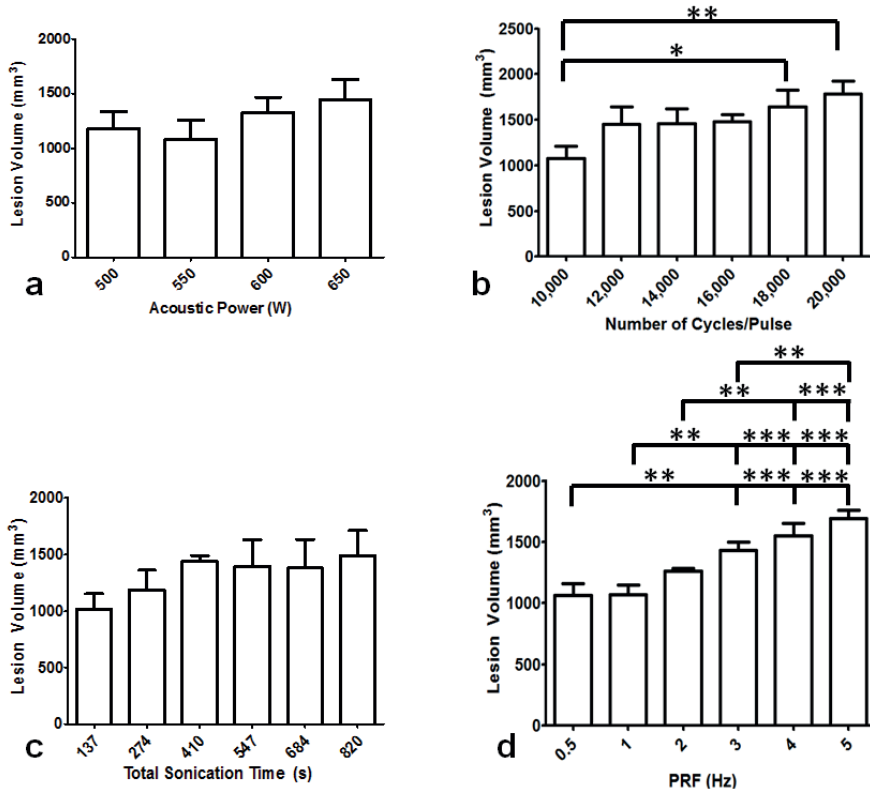


Fig 3. Lesion volume in tissue mimicking phantom for varying BH sonication parameters. **a.** Lesion volume did not vary significantly for acoustic power 500-650 W at constant PRF of 1 Hz ($p > 0.05$, ANOVA). **b.** Lesion volume with varying cycles/pulse. Significant differences ($p \leq 0.05$) in lesion volumes were found between 10,000 and 18,000 cycles/pulse as well as 10,000 and 20,000 cycles/pulse. **c.** Varying total sonication time between 137 to 820 seconds resulted in no significant differences ($p \leq 0.05$). **d.** Pulse repetition frequency (PRF) was varied from 0.5 to 5 Hz. The lesion volumes were significantly different between 0.5 and 3, 4, and 5 Hz ($p \leq 0.05$). Similar differences were found between 1 and 3, 4 and 5 Hz, as well as between 2 and 4 and 5 Hz ($p \leq 0.05$).

2.4.3 Effect of BH Sonication Parameters on Temperature Elevation

Understanding temperature changes at or near the focal region provides insight on the effect of varying BH sonication parameters. Three coronal slices and one sagittal slice centered on the focal region were used to measure temperature changes relative to baseline during each sonication. Slices along both orientations were compared for each sonication. Additionally, temperature elevation for two different sonications (e.g., PRF of 0.5 and 5 Hz) was compared. FWHM was calculated from the temperature maps as a measure of temperature distribution for all sonication parameters.

2.4.4 Comparing Temperature Dynamics at Different Locations at the Focal Zone

Fig 4a shows a comparison of temperature in first coronal (placed at the center of focus), second coronal (placed 7 mm from the center of focus), and sagittal slices for a sonication at 4 Hz PRF, 15,000 cycles/pulse, and 600 W acoustic power. The first coronal slice shows a rapid exponential increase in temperature until 100 seconds. At the end of sonication, a peak temperature of 87°C was attained. The sagittal slice displayed a similar peak temperature and trend in temperature. Post sonication, the temperature in both slices exponentially dropped to 46°C within 120 seconds. The second coronal slice demonstrated minimal temperature increase when compared to first coronal and sagittal slices. The maximum temperature in the second coronal slice was 49°C. Fig 4b shows a temperature comparison for all slices for a total sonication time of 684 seconds at 1Hz PRF and 600 W acoustic power. The first coronal slice indicated a rapid exponential temperature increase until 100 seconds; a similar result as observed in Fig 4a. Between 100 and 684 seconds, the temperature continued to increase, but at a lower rate. At the end of sonication, the peak temperature was 63°C. The sagittal slice showed a similar trend in observed temperature; a peak temperature of 57°C. Post sonication, the temperature within the ROI exponentially dropped to 43°C within 120 seconds. The second coronal slice in this case also

Chapter 2

displayed a minimal temperature increase when compared to first coronal and sagittal slices. The maximum temperature in the second coronal slice was 43°C.

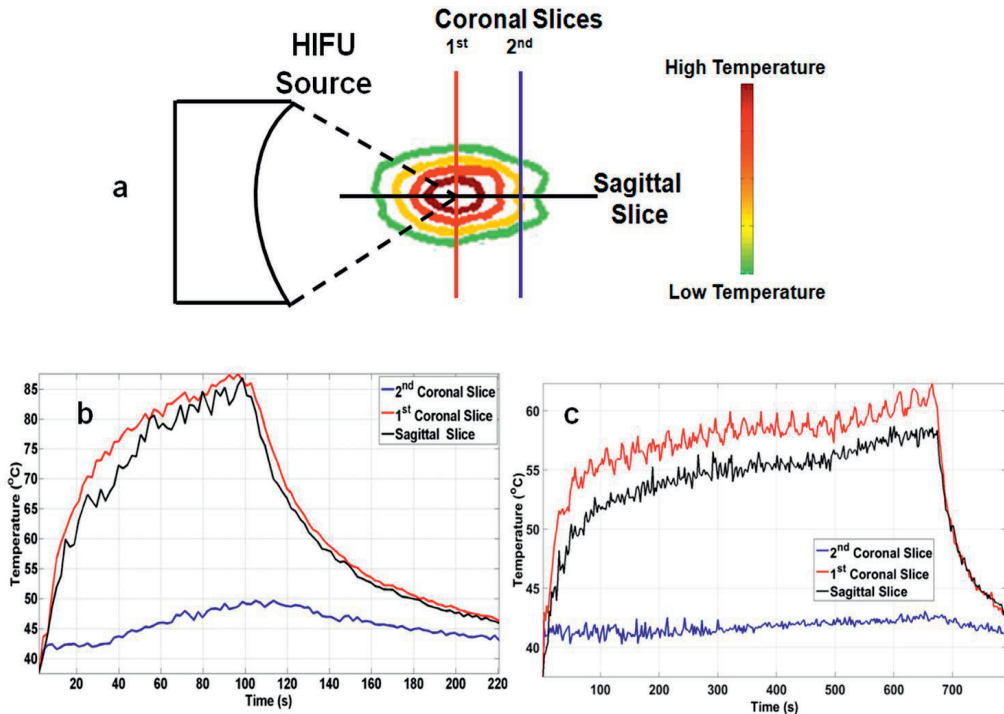


Fig 4. a. Illustration of temperature contours due to heat accumulating at focus. The position of coronal and sagittal MRI thermometry slices at which real time temperature measurements are made, is also marked. **b.** Sonication performed at 600 W of acoustic power, 4 Hz PRF, and 15,000 cycles/pulse. Sagittal and first coronal slices had similar characteristics, reaching a peak temperature of 87°C. The second coronal slice had a maximum temperature of 46°C, throughout the entire sonication. **c.** Sonication performed at 600 W of acoustic power, at 1 Hz PRF for 684 seconds. Both first coronal and sagittal slices had similar temperature curve shapes, while the second coronal slice has marginal change in temperature, with a peak temperature of 63°C, 57°C, and 43°C respectively.

2.4.5 Effect of Sonication Parameters on Focal Temperature Dynamics

Temperature curves from the first coronal slice were compared for acoustic powers of 550, 600, and 650 W, with other parameters kept constant (Fig 5a). All three curves indicated different rates of temperature increase, with temperatures plateauing at 52°C, 57°C, and 63°C respectively, after 200 seconds of sonication. Peak temperature was attained towards the end of the sonication and observed to be 53°C for 500 W, 60°C for 600 W, and 65°C for 650 W. A similar result is seen in Fig 5b for temperature comparison for sonications at 0.5, 2, and 5 Hz PRF, keeping other parameters constant. Temperature did not increase beyond 50°C at 0.5 Hz PRF. In addition, the rate of temperature increase between the three PRF values was different. Peak temperatures of 49°C, 72°C, and 95°C for 0.5, 2, and 5 Hz, respectively, were obtained. Peak temperature for 2 and 5 Hz PRF was attained in less than 70 and 150 seconds respectively.

2.4.6 Spatial Temperature Distribution at Different Sonication Parameters

Exponential increase in temperature FWHM with increasing acoustic power was observed ($R^2 = 0.95$). Significant differences in FWHM across all acoustic power values were found (overall ANOVA $p \leq 0.0001$). Post-hoc test revealed no differences in FWHM between 500 and 550W, or between 550 and 600W ($p > 0.05$). All other acoustic powers were significantly different from each other ($p \leq 0.05$, Fig 6a) in terms of temperature FWHM. While comparing FWHM across the number of cycles/pulse parameter, there was a linear increase in FWHM ($R^2 = 0.82$), with overall significant differences (overall ANOVA $p = 0.048$). Significant difference between 10,000 and 20,000 cycles/pulse were found using post-hoc test ($p \leq 0.05$). However, there was no significant difference in FWHM between any other parameters as observed in Fig 6b. Fig 6c shows that while extending total sonication time from 137 to 820 seconds and keeping other parameters constant, no significant difference was found in the FWHM between any parameters ($p = 0.235$). Exponential increase in FWHM was also observed with increasing PRF ($R^2 = 0.80$). Significant differences were found across PRF values (overall ANOVA $p = 0.0001$). Post-hoc tests revealed

Chapter 2

no differences between 2 and 3, 4 or, 5 Hz nor between 3 and 4 or 5 Hz ($p > 0.05$). All other comparisons presented significant differences ($p \leq 0.05$, Fig 6d).

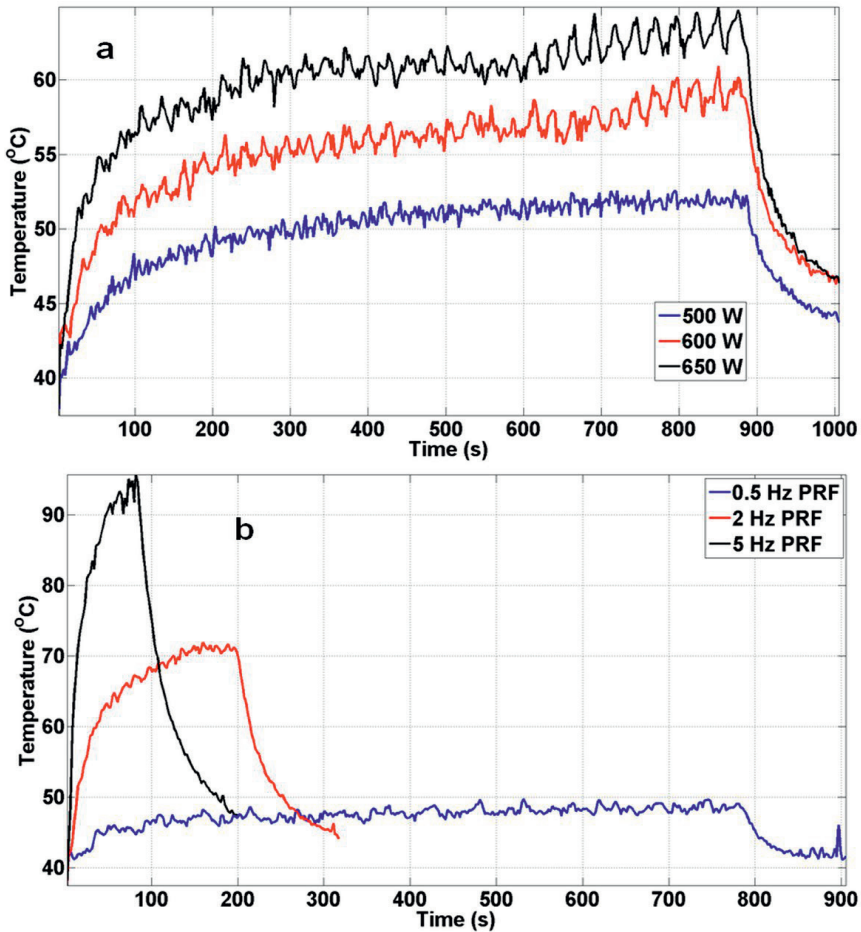


Fig 5. First coronal temperature slice was compared against first coronal temperature slices at different sonication parameters. **a.** Maximum temperature in tissue mimicking phantoms compared at 500, 600, and 650 W of acoustic power. All three power settings produced similar exponential temperature increase and decrease, with different peak temperatures. **b.** Temperature curves obtained while sonicating at 0.5, 2, and 5 Hz PRF. The peak temperatures obtained were 50°C, 72°C, and 95°C for PRF of 0.5, 2, and 5 Hz, respectively.

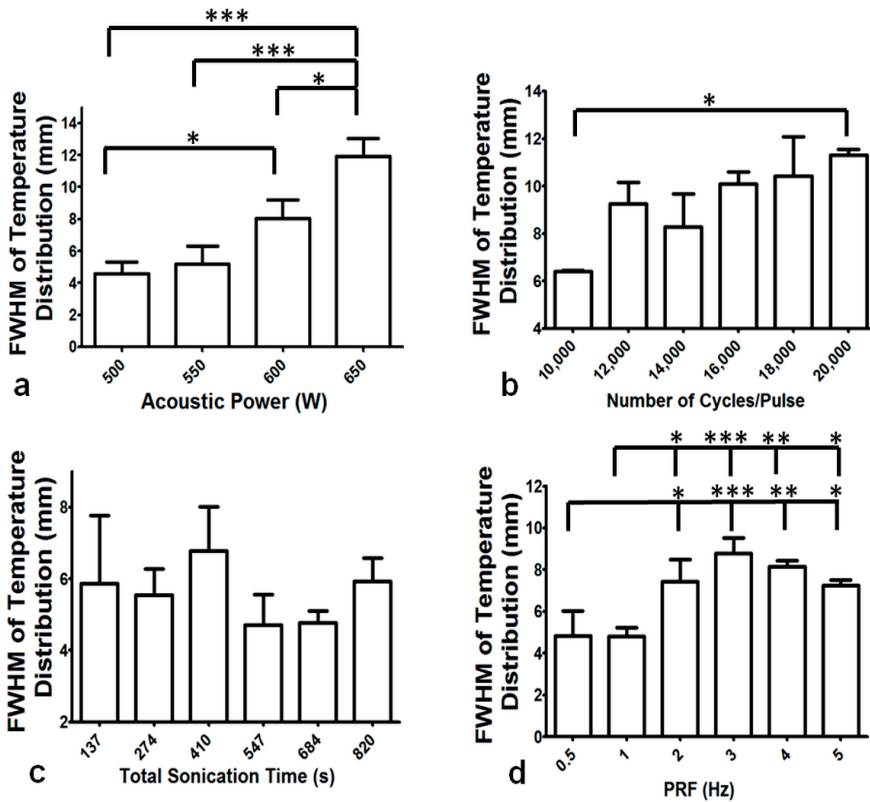


Fig 6. Full width at half maximum (FWHM) was calculated as a measure of temperature distribution at the end of each sonication in tissue mimicking phantoms. **a.** Varying acoustic power, significant differences in FWHM were found between 550 and 650 W, as well as for 600 and 650 W ($p \leq 0.05$). **b.** Comparing the number of cycles/pulse, significant differences were found between 10,000 cycles/pulse and 20,000 cycles/pulse ($p = 0.042$). Other parameters showed no differences in FWHM. **c.** Total sonication was varied from 137 to 820 seconds and no significant difference was found in the FWHM between any parameters ($p > 0.05$). **d.** Varying PRF from 0.5 Hz to 5 Hz resulted in significant differences in FWHM between 0.5 and 2, 3, 4, and 5 Hz. Similarly, significant differences were found between 1 and 2, 3, 4, and 5 Hz ($p \leq 0.05$). No significant differences were found between any other parameters.

Area of Lethal Thermal Dose

Correlations between lesion volume and area of thermal dose provided insight to the relationship between these two variables based on varying sonication parameters. Acoustic power and area of lethal thermal dose > 240 CEM43 had a positive (Pearson $r = 0.52$) but insignificant correlation ($p = 0.087$, Fig 7a). Area of lethal thermal dose did not correlate with lesion volume for the number of cycles/pulse parameter ($p = 0.97$; Pearson $r = -0.009$), as seen in Fig 7b. However, total sonication time and PRF correlated well with lesion volume; the Pearson r was 0.58 and 0.80 with $p=0.012$ and $p \leq 0.0001$, respectively for both sonication parameters (Fig 7c & d).

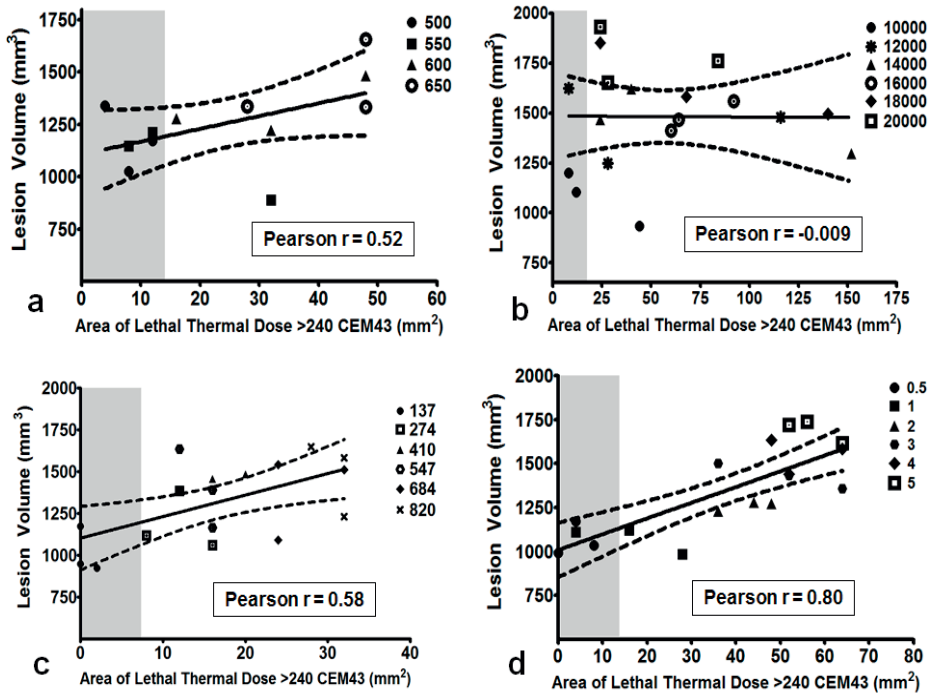


Fig 7. Correlation between lesion volume and area of lethal thermal dose greater than 240 CEM43. Grey area corresponds to 13 mm², which is the area of each sonication layer. Any data point within this gray area corresponds to sonication parameters that produce thermal dose in an area equal to or less than the target

Boiling histotripsy lesion characterization

area (13 mm²). **a.** Positive, insignificant correlation (Pearson $r = 0.52$, $p = 0.08$) was found between the two variables while varying acoustic power. **b.** No correlation was found while varying the number of cycles/pulse (Pearson $r = -0.009$, $p = 0.97$). **c.** Positive, strong correlation was found while varying total sonication time (Pearson $r = 0.58$, $p \leq 0.001$). **d.** Correlation between lesion volume and area of lethal thermal dose while varying PRF was also significantly positive (Pearson $r = 0.80$, $p \leq 0.001$).

2.4.7 Boiling Histotripsy Lesions in *Ex vivo* Porcine Tissues

We additionally demonstrated the ability of this clinical MR-HIFU system to perform BH in *ex vivo* tissues, with the ultimate intent to apply BH *in vivo*. Temperature data were similar between two consecutive liver sonications at 600 W acoustic power at 1 Hz PRF (Fig 8a). The post sonication H&E images are shown alongside the corresponding gross pathology photographs in Figs 9, 10 and 11. Gross morphological analysis showed similar lesions for sonications repeated with same parameters. Differences in qualitative morphological parameters such as lesion shape and size were observed between sonication at 1 Hz PRF, 600 W, and 20,000 cycles/pulse and sonication at 5 Hz PRF, 600 W, and 15,000 cycles/pulse.

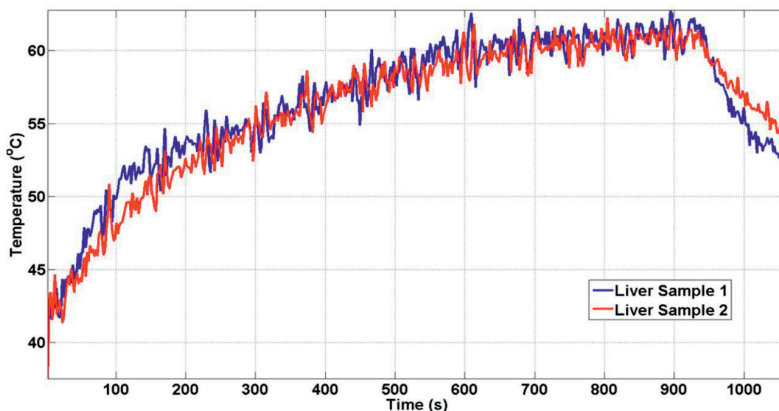


Fig 8. Temperature change measured at the first coronal slice for separate liver samples. The sonication parameters for both liver samples were 650 W of acoustic power, 15,000 cycles/pulse at 1 Hz PRF. The peak temperature was reached at the end of the sonication (64°C). Both temperature curves show similar dynamics.

Chapter 2

Sonicated porcine liver with 20,000 cycles/pulse, 600 W acoustic power at 1 Hz PRF, formed a large lesion with its contents completely liquefied, as observed in top panel of Fig 9. The lesion had sharp boundaries with thermal damage (red arrowhead, Fig 9a). The corresponding H&E slide shows negligible necrosis on one side, while there is evidence of necrosis on the opposite side (Fig 9b & 9c). Closer examination of the H&E slide reveals the necrotic region to be less than 400 microns in diameter, with a sharp lesion boundary (red arrowhead, Fig 9b & 9c). Critical structures such as bile ducts (red dotted margin) and nerves (yellow dotted margin) appeared physically intact 2 mm away from the focal region (Fig 11). Fig 9d shows a photograph of sonicated cardiac tissue with an 8 mm diameter lesion filled with liquefied tissue (blue dotted circle). The lesion had a white concentric band, possibly due to thermal denaturation. The cardiac tissue H&E slide shows a corresponding necrotic band of tissue around the lesion with a sharp boundary, similar to the liver tissue (Figs 9e & f).

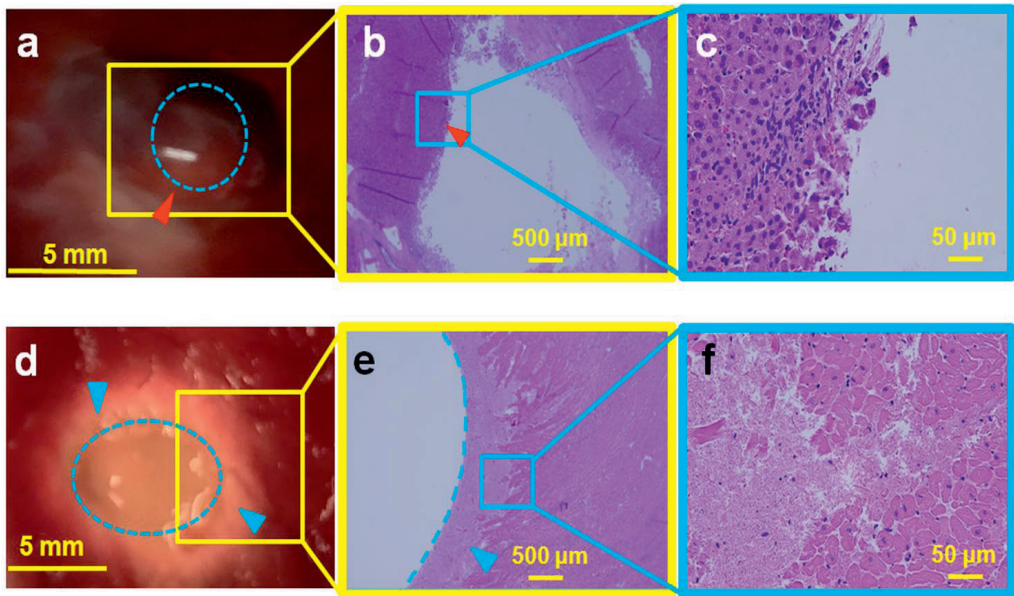


Fig 9. Ex vivo porcine liver (top panel) and cardiac muscle (bottom panel) sonicated at 600 W acoustic power at 1 Hz PRF and 20,000 cycles/pulse. **a.** Gross pathology of the liver tissue with the lesion in the

center (red arrowhead), showing minimal thermal damage with a liquefied central void (blue dotted circle). **b.** H&E slide showing the entire lesion with sharp boundaries (red arrowhead). **c.** Magnification (4X) of the Fig 9b, presenting intact cell structures at the periphery of the lesion. **d.** Gross pathology of the cardiac tissue with a large void in the center (blue dotted oval). A concentric ring of necrosis (blue arrowheads) surrounds the central void. **e.** H&E slide, with the void outlined by the blue dotted line and the blue arrowhead pointing to the region of necrosis. **f.** Magnified image (40X) of Fig 9e show regions of both necrosis and intact cellular structures.

To determine the effect of higher PRF at 15,000 cycles/pulse and 600 W acoustic power, porcine liver was sonicated using these parameters at 5 Hz PRF. The resultant liver lesion had a whitish, disc shaped region, 8 mm in diameter (Fig 10a). This region appeared thermally denatured with no structural integrity. While preparing the tissue for H&E stain, the thermally denatured region at times disintegrated into paste-like debris, leaving behind a hole. H&E slides show tissue completely fractionated with no intact cells at the focal region (Figs 10b & c). Fig 10d shows the gross pathology of cardiac tissue, displaying a hole at the center of the focal region filled with liquefied tissue debris. The boundary of this lesion has a thin white rim, possibly providing some evidence of marginal thermal denaturation (red arrowhead). The corresponding H&E stain shows a hole with a sharp boundary (red arrowhead, Fig 10e). The boundary also contains a small necrotic region, while the rest of the tissue appears intact with no signs of necrosis, as seen in the magnified image (Fig 10f).

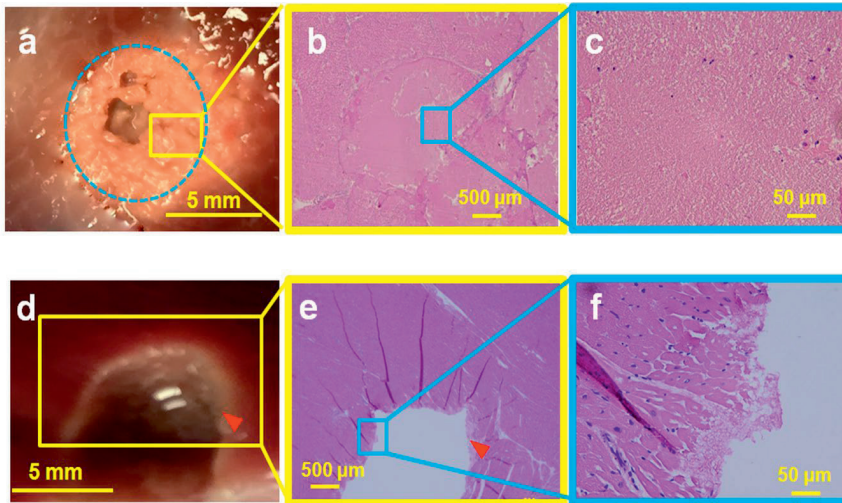


Fig 10. Ex vivo porcine liver (top panel) and cardiac muscle tissue (bottom panel) sonicated with 600 W at 5 Hz PRF. **Top Panel:** **a.** Gross pathology of the lesion appeared thermally denatured, with a diameter of 8 mm (blue dotted circle). This area was not structurally intact and disintegrated during pathological stain preparation process. **b.** H&E slide showing diffuse thermal effects, with little cellular structure. **c.** Magnification (40X) of the Fig 10b with parts of the lesion showing absence of cellular structure, representing homogenization of tissue. **Bottom Panel:** **d.** Cardiac muscle with a liquefied void in the center of the lesion with sharp boundary with negligible thermal effects (red arrowhead). **e.** H&E slide of the lesion shows that cellular structure around the void was intact, with no evidence of thermal damage. The lesion also has sharp boundaries (red arrowhead). **f.** Magnification (40X) of the lesion boundary, with most of the boundary tissue intact.

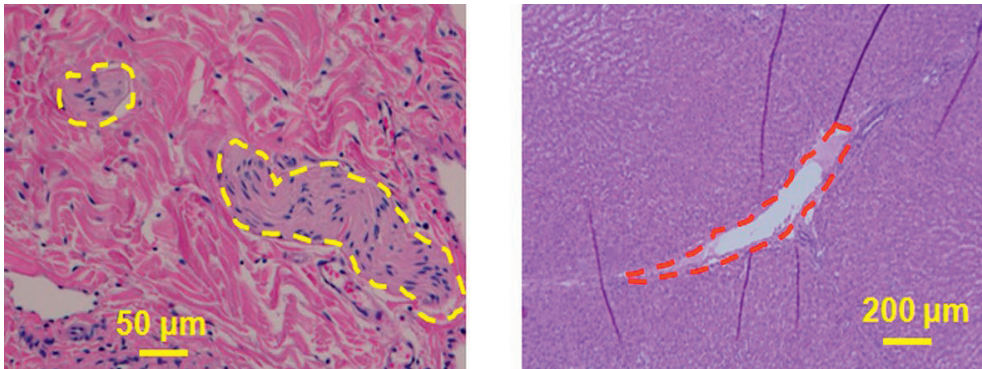


Fig 11. Liver tissue was sonicated with 650 W at 1 Hz PRF. **a.** Dotted yellow margins represent the nerves in liver tissue that were intact post sonication. These nerves were situated less than 300 μm from the focal region, showing the ability of BH to spare nerves. **b.** Bile ducts located less than 500 μm from the focal region were also structurally intact (red dotted margin) post sonication. Tissue surrounding the bile duct was also intact and did not have any signs of necrosis.

2.5.1 MRI Monitoring of *Ex Vivo* Tissue Destruction

Post sonication T1W imaging of the liver after BH revealed a hypointense region (red dotted circle, Fig 12b). Both the lesion boundaries and the tail of the lesion are clearly detectable (Fig 12c). Fig 12e shows a post sonication T2W coronal image with a visible lesion (yellow arrow). The subtraction image of pre and post-sonication images shown in Fig 12f demonstrates the lesion from top view (blue box) and adjacent blood vessels (blue arrowhead).

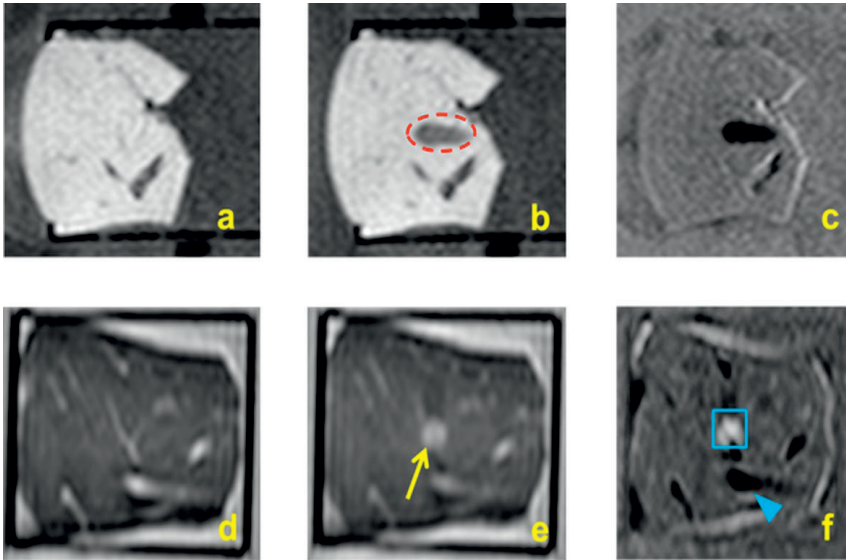


Fig 12. a. T1W imaging of porcine liver using fast field echo 3D used for planning HIFU sonications b. T1W imaging of the liver tissue post sonication shows a hypointense signal of a tadpole-shaped lesion created using BH (red dotted circle) c. Subtraction of pre-sonication from post-sonication (Fig 12b minus Fig 12a) images highlights the BH lesion. d. T2W imaging using turbo spin echo 3D were also performed e. T2W imaging post sonication showing the BH lesion along the coronal plane f. Subtraction of pre-sonication from post-sonication images (Fig 12e minus Fig 12d) highlighting the lesion (blue box) and surrounding blood vessels (blue arrowhead).

2.5 Discussion

This experimental work focuses on characterization of the effect of BH sonication parameters on resulting lesion volume, temperature distribution, and thermal dose. Such characterization is necessary to define the extent of BH lesion formation with mechanical damage, thermal effect, or a combination of both. Thermal and mechanical effects in tissue mimicking and *ex vivo* tissue due to BH have been briefly described by Khokhlova *et al*⁵⁶. In order to characterize the effect of several additional BH sonication parameters such as acoustic power, number of cycles/pulse,

total sonication time, and PRF on lesion characteristics, we examined lesion volume, temperature distribution, and thermal dose.

The current experimental work produced lesion volumes greater than 1 cm³ both in TMP's and *ex-vivo* tissues, suggesting that a clinical MR-HIFU system can produce large, clinically relevant BH lesion volumes. Table 3 provides a synopsis of the effect of sonication parameters on lesion volume, temperature distribution and area of lethal thermal dose. Considering that the 'head' part of the tadpole-shaped lesion is the largest contributor to lesion volume, the segmentation results did not show a significant change with increasing acoustic power. Comparison of pulse length between 10,000 cycles/pulse to 18,000 cycles/pulse and, 20,000 cycles/pulse did however increase lesion volume. This is due to increase in energy deposition, causing greater damage to the tissue mimicking phantom. Our results also show that if pulse length, power and PRF are kept constant, the lesion volume does not vary much with increasing total sonication time.

Increasing acoustic power produced a significant increase in temperature distribution. This could be due to increased incident acoustic pressure reducing the time-to-boil causing quicker and enhanced heating at the focal region. In addition, the lack of perfusion complements this effect in both tissue mimicking phantoms and *ex-vivo* tissues. Thus, this model, using the weak shock theory to calculate time-to-boil, may not perfectly represent changes *in vivo* tissue. To obtain the time-to-boil more accurately for *in vivo* experiments, a model that considers diffusion effects needs to be explored in the future. A similar difference in temperature distribution between 10,000 cycles/pulse and 20,000 cycles/pulse was observed, likely due to an increase in total energy deposited which is known to increase both focal region temperature and lesion volume. Increase in total sonication time shows that there is a threshold total sonication time or number of pulses per location, beyond which lesion volume or temperature no longer increase. Prior studies have shown an increase in PRF or DC causing an increase in rate of energy deposition at the

Chapter 2

focal region⁵⁶. This is also reflected in our results with a significant increase in temperature FWHM and lesion volume while increasing PRF.

Table 3. Effect of each of the four BH sonication parameters on significant increase in lesion volume and focal region temperature are summarized. Increasing acoustic power did not result in an increase in lesion volume, whereas temperature distribution and area of lethal thermal dose increased. While increasing number of cycles/pulse, both lesion volume and temperature distribution increased. No increase in either lesion volume or temperature distribution was observed while increasing total sonication time, but area of lethal thermal dose increased. Varying pulse repetition frequency resulted in increased lesion volume and temperature distribution and area of lethal thermal dose.

Acoustic Power (W)	Number of cycles/pulse	Pulse Length (ms)	Total Sonication Time (seconds)
Acoustic Power	No	Yes	Yes
Number of Cycles/Pulse	Yes	Yes	No
Total Sonication Time	No	No	Yes
PRF	Yes	Yes	Yes

Correlation between lesion volume and area of lethal thermal dose provided valuable information on the effect of sonication parameters on tissue mimicking phantoms. Our experiments show that for both 500 and 550 W acoustic powers, the lethal thermal dose was contained within the targeted sonication area (13 mm², grey region in Fig 6). Although strong correlation was not found between area of lethal thermal dose and lesion volume while varying number of cycles/pulse, there is some evidence that 20,000 cycles/pulse could produce larger lesion volumes than 10,000 cycles/pulse yet yield a similar area of lethal thermal dose. This could have valuable clinical implications and may need to be studied further. Lower total sonication times and PRF values contained the lethal thermal dose within the targeted sonication area. Depending on the application and the target location, table 3 and Figs 2, 5, and 6 provide a basic pathway in selecting sonication parameters for future BH studies.

The relatively low spatiotemporal resolution of MRI thermometry may result in peak temperature measurement inaccuracies when monitoring boiling that occurs on the order of milliseconds. However, unlike in HIFU thermal ablation, macroscopic temperature changes as

Chapter 2

produced by the BH technique are slow due to low applied duty cycles. MRI provides a measurement of the mean temperature within a voxel. However, the peak intra voxel temperature can be higher, depending on the spatial acquisition resolution. In this study, the size of the focal point ($1.6 \times 1.6 \times 10$ mm) was smaller than the MRI voxel size ($2.5 \times 2.5 \times 7$ mm), which can lead to inaccuracies in temperature and thermal dose measurements. While the Sonalleve therapy planning software compensates for temperature standard deviation in thermal dose calculations, it does not compensate for intra voxel spatial temperature variations. This does not pose a substantial issue in our study, however, since we only compare the differences in temperature and thermal dose with varying sonication parameters; not accurately characterize the cumulative thermal dose.

To relate to clinical HIFU therapy, we placed three MRI thermometry slices along the coronal plane and one slice along the sagittal plane, to monitor temperature related effects throughout the focal region. As expected, the temperature-time series data at the sagittal plane was similar to the temperature-time series data from the first coronal slice, which was at the middle of the sonication zone. Temperature measured at the second coronal slice for all sonication parameters was well under 50°C , explained by the fact that this slice was 7 mm away from the focus. This result could be influential in future *in vivo* applications, including local temperature triggered, tumor specific drug release, immunomodulation and other bio-effects. Temperature curves for sonications performed at 1 Hz PRF had a characteristic cyclic variation in temperature that lasted for 27 seconds. This follows the sonication pattern where the 27-point cube is sonicated at one location per second. As the sonication proceeded, the bottom and middle layer (nearest to the transducer) broke down first causing a drop in temperatures. The top layer (farthest from transducer) and phantom material beyond was still intact and therefore the temperature continued to rise. The other factor that may have caused this effect is the location of the sonication layer being farther away from the center of the temperature-mapping slice. This causes the

measured temperatures to be slightly lower than the temperature measured at the center of the temperature-mapping slice.

Ex vivo tissues were sonicated to demonstrate the capability of this clinical MR-HIFU system to perform BH *in vivo*. Porcine liver and cardiac muscle that were sonicated with identical parameters yielded lesions that were visually different. Lesion in the liver tissue appeared to be larger, with greater tissue destruction compared to the cardiac muscle, possibly attributable to the differing mechanical properties of the tissues. At 600 W, 1 Hz PRF, and 20,000 cycles/pulse, the liver tissue was mechanically disrupted, with a large visible void at the focal region. The lesion had some thermal effects on one side of the lesion, possibly due to increased thermal dose at that region. For the same set of sonication parameters, the cardiac tissue had a hole at the center of the focal region surrounded by concentric ring of tissue necrosis around the lesion (Fig 9). The concentric ring was due to uniform heating at the middle of the 'head' of the BH lesion causing thermal damage to tissue. Sonicating liver tissue at 5 Hz PRF, 15,000 cycles/pulse, and 600 W, the focal region had a paste-like circular lesion, indicating significant thermal effects. In contrast, cardiac tissue at these parameters has a void filled with liquefied tissue. There was also no evidence of thermal denaturation beyond this void. This interesting finding shows the variability in lesion formation in different tissue types for the same BH sonication parameters. BH may therefore need to be characterized or calibrated on a tissue or organ specific basis. Additionally, our data show the ability of BH to retain adjacent tissue structure for long sonication periods, high acoustic powers, or PRFs (Fig 11). This finding is vital for future *in vivo* experiments since it shows the ability for vital vessel or structure-sparing using a clinical HIFU system, thus potentially opening new preclinical and clinical avenues. In addition, the ability to visualize BH lesions on MRI indicates that an MRI contrast agent may not be required *in vivo*. However, MRI contrast agents used *in vivo* may further benefit MR imaging of BH lesions post sonication, which needs to be explored further.

Chapter 2

2.6 Conclusion

This experimental work characterizes and quantifies the effect of varying BH sonication parameters using a commercially available clinical MR-HIFU system. The effects quantified include temperature, thermal dose, and lesion volume. Experiments were performed utilizing tissue-mimicking phantoms and *ex vivo* tissues. Results indicate varying lesion volumes and temperature effects for different BH sonication parameters. Future work may need to characterize BH effects *in vivo* in different tissues and organs. Such a characterization may facilitate clinical translation of BH. Our results also provide parameter recommendations for future BH experiments. In the future, it may be useful to test the short and long-term effects of varying these sonication parameters extensively *in vivo* using this MR-HIFU system. Additionally, it will be imperative to assess the effects of tissue perfusion on lesion formation, lesion volumes, and temperature elevation.

2.7 References

- 1 Lal, D. R. *et al.* Results of multimodal treatment for desmoplastic small round cell tumors. *Journal of pediatric surgery* **40**, 251-255 (2005).
- 2 Dupuy, D. E. *et al.* Percutaneous radiofrequency ablation of malignancies in the lung. *American Journal of Roentgenology* **174**, 57-59 (2000).
- 3 Gervais, D. A. *et al.* Radio-frequency Ablation of Renal Cell Carcinoma: Early Clinical Experience 1. *Radiology* **217**, 665-672 (2000).
- 4 Gill, I. S. *et al.* Renal cryoablation: outcome at 3 years. *The Journal of urology* **173**, 1903-1907 (2005).
- 5 Wright, A. S., Lee Jr, F. T. & Mahvi, D. M. Hepatic microwave ablation with multiple antennae results in synergistically larger zones of coagulation necrosis. *Annals of Surgical Oncology* **10**, 275-283 (2003).
- 6 Gangi, A. *et al.* Osteoid Osteoma: Percutaneous Laser Ablation and Follow-up in 114 Patients 1. *Radiology* **242**, 293-301 (2007).
- 7 Pacella, C. M. *et al.* Thyroid tissue: us-guided percutaneous interstitial laser ablation—a feasibility study 1. *Radiology* **217**, 673-677 (2000).
- 8 Ebara, M. *et al.* Percutaneous ethanol injection for the treatment of small hepatocellular carcinoma. Study of 95 patients. *Journal of gastroenterology and hepatology* **5**, 616-626 (1990).
- 9 Livraghi, T. *et al.* Hepatocellular carcinoma and cirrhosis in 746 patients: long-term results of percutaneous ethanol injection. *Radiology* **197**, 101-108 (1995).
- 10 Chin, J. L. *et al.* Results of salvage cryoablation of the prostate after radiation: identifying predictors of treatment failure and complications. *The Journal of urology* **165**, 1937-1942 (2001).
- 11 Johnson, D. B. *et al.* Defining the complications of cryoablation and radio frequency ablation of small renal tumors: a multi-institutional review. *The Journal of urology* **172**, 874-877 (2004).
- 12 Liang, P., Wang, Y., Yu, X. & Dong, B. Malignant liver tumors: Treatment with percutaneous microwave ablation—complications among cohort of 1136 patients 1. *Radiology* **251**, 933-940 (2009).
- 13 Livraghi, T. *et al.* Treatment of Focal Liver Tumors with Percutaneous Radio-frequency Ablation: Complications Encountered in a Multicenter Study 1. *Radiology* **226**, 441-451 (2003).
- 14 Rhim, H. *et al.* Radiofrequency Thermal Ablation of Abdominal Tumors: Lessons Learned from Complications 1. *Radiographics* **24**, 41-52 (2004).
- 15 Bailey, M., Khokhlova, V., Sapozhnikov, O., Kargl, S. & Crum, L. Physical mechanisms of the therapeutic effect of ultrasound (a review). *Acoustical Physics* **49**, 369-388 (2003).
- 16 Chapman, A. & Ter Haar, G. Thermal ablation of uterine fibroids using MR-guided focused ultrasound—a truly non-invasive treatment modality. *European radiology* **17**, 2505-2511 (2007).
- 17 Kim, Y.-s. *et al.* Volumetric MR-HIFU ablation of uterine fibroids: role of treatment cell size in the improvement of energy efficiency. *European journal of radiology* **81**, 3652-3659 (2012).
- 18 Illing, R. *et al.* The safety and feasibility of extracorporeal high-intensity focused ultrasound (HIFU) for the treatment of liver and kidney tumours in a Western population. *British journal of cancer* **93**, 890-895 (2005).
- 19 Kennedy, J. *et al.* High-intensity focused ultrasound for the treatment of liver tumours. *Ultrasonics* **42**, 931-935 (2004).
- 20 Watkin, N. A., Morris, S. B., Rivens, I. H. & Haar, G. R. t. High-intensity focused ultrasound ablation of the kidney in a large animal model. *Journal of Endourology* **11**, 191-196 (1997).
- 21 Chen, W. & Zhou, K. High-intensity focused ultrasound ablation: a new strategy to manage primary bone tumors. *Current Opinion in Orthopaedics* **16**, 494-500 (2005).
- 22 Huisman, M. *et al.* Feasibility of volumetric MRI-guided high intensity focused ultrasound (MR-HIFU) for painful bone metastases. *J Ther Ultrasound* **2**, b51 (2014).
- 23 Gelet, A. *et al.* Transrectal high-intensity focused ultrasound: minimally invasive therapy of localized prostate cancer. *Journal of Endourology* **14**, 519-528 (2000).
- 24 Poissonnier, L. *et al.* Control of prostate cancer by transrectal HIFU in 227 patients. *European urology* **51**, 381-387 (2007).
- 25 Li, L. *et al.* Mild hyperthermia triggered doxorubicin release from optimized stealth thermosensitive liposomes improves intratumoral drug delivery and efficacy. *Journal of Controlled Release* **168**, 142-150 (2013).

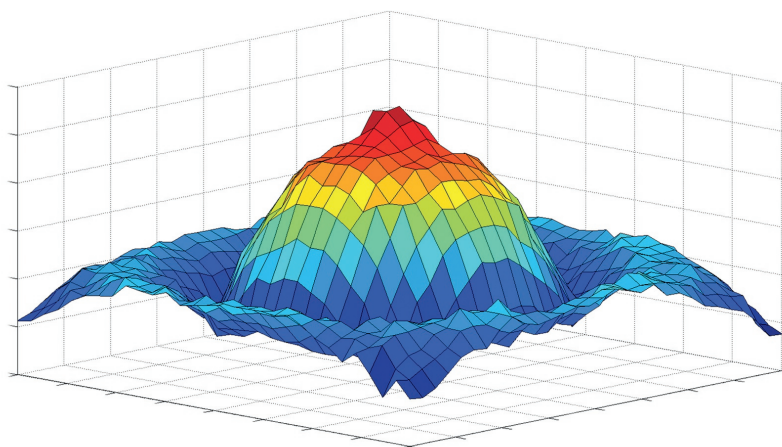
Chapter 2

- 26 Partanen, A. *et al.* Mild hyperthermia with magnetic resonance-guided high-intensity focused ultrasound for applications in drug delivery. *International journal of hyperthermia* **28**, 320-336 (2012).
- 27 Roberts, W. W. Development and translation of histotripsy: current status and future directions. *Current opinion in urology* **24**, 104 (2014).
- 28 Köhler, M. O. *et al.* Volumetric HIFU ablation under 3D guidance of rapid MRI thermometry. *Medical physics* **36**, 3521-3535 (2009).
- 29 Quesson, B. *et al.* A method for MRI guidance of intercostal high intensity focused ultrasound ablation in the liver. *Medical physics* **37**, 2533-2540 (2010).
- 30 Hesley, G. K., Gorny, K. R., Henrichsen, T. L., Woodrum, D. A. & Brown, D. L. A clinical review of focused ultrasound ablation with magnetic resonance guidance: an option for treating uterine fibroids. *Ultrasound quarterly* **24**, 131-139 (2008).
- 31 Rabkin, B. A., Zderic, V. & Vaezy, S. Hyperecho in ultrasound images of HIFU therapy: involvement of cavitation. *Ultrasound in medicine & biology* **31**, 947-956 (2005).
- 32 Vaezy, S. *et al.* Real-time visualization of high-intensity focused ultrasound treatment using ultrasound imaging. *Ultrasound in medicine & biology* **27**, 33-42 (2001).
- 33 Hwang, J. H. *et al.* Preclinical in vivo evaluation of an extracorporeal HIFU device for ablation of pancreatic tumors. *Ultrasound in medicine & biology* **35**, 967-975 (2009).
- 34 Rieke, V. & Butts Pauly, K. MR thermometry. *Journal of Magnetic Resonance Imaging* **27**, 376-390 (2008).
- 35 Chaussy, C. & Thüroff, S. Results and side effects of high-intensity focused ultrasound in localized prostate cancer. *Journal of Endourology* **15**, 437-440 (2001).
- 36 Vlasisavljevich, E. *et al.* Histotripsy-induced cavitation cloud initiation thresholds in tissues of different mechanical properties. *Ultrasonics, Ferroelectrics, and Frequency Control, IEEE Transactions on* **61**, 341-352 (2014).
- 37 Xu, Z., Hall, T. L., Fowlkes, J. B. & Cain, C. A. Effects of acoustic parameters on bubble cloud dynamics in ultrasound tissue erosion (histotripsy). *The Journal of the Acoustical Society of America* **122**, 229-236 (2007).
- 38 Simon, J. C. *et al.* Ultrasonic atomization of tissue and its role in tissue fractionation by high intensity focused ultrasound. *Physics in medicine and biology* **57**, 8061 (2012).
- 39 Khokhlova, T. D. *et al.* Ultrasound-guided tissue fractionation by high intensity focused ultrasound in an in vivo porcine liver model. *Proceedings of the National Academy of Sciences* **111**, 8161-8166 (2014).
- 40 Hempel, C. R. *et al.* Histotripsy fractionation of prostate tissue: local effects and systemic response in a canine model. *The Journal of urology* **185**, 1484-1489 (2011).
- 41 Hall, T. L. *et al.* Histotripsy of rabbit renal tissue in vivo: temporal histologic trends. *Journal of Endourology* **21**, 1159-1166 (2007).
- 42 Xu, Z., Owens, G., Gordon, D., Cain, C. & Ludomirsky, A. Noninvasive creation of an atrial septal defect by histotripsy in a canine model. *Circulation* **121**, 742-749 (2010).
- 43 Bini, M. G. *et al.* The polyacrylamide as a phantom material for electromagnetic hyperthermia studies. *IEEE Trans Biomed Eng* **31**, 317-322 (1984).
- 44 Lafon, C. *et al.* Gel phantom for use in high-intensity focused ultrasound dosimetry. *Ultrasound Med Biol* **31**, 1383-1389 (2005).
- 45 Oppermann, W., Rose, S. & Rehage, G. The elastic behaviour of hydrogels. *British polymer journal* **17**, 175-180 (1985).
- 46 Stingl, J. *et al.* Morphology and some biomechanical properties of human liver and spleen. *Surgical and Radiologic Anatomy* **24**, 285-289 (2002).
- 47 Zell, K., Sperl, J., Vogel, M., Niessner, R. & Haisch, C. Acoustical properties of selected tissue phantom materials for ultrasound imaging. *Physics in medicine and biology* **52**, N475 (2007).
- 48 Duck, F. A. *Physical properties of tissues: a comprehensive reference book.* (Academic press, 2013).
- 49 Lam, F., Mavor, A., Potts, D. & Giles, G. Improved 72-hour renal preservation with phosphate-buffered sucrose. *Transplantation* **47**, 767-770 (1989).
- 50 Quesson, B., de Zwart, J. A. & Moonen, C. T. Magnetic resonance temperature imaging for guidance of thermotherapy. *Journal of Magnetic Resonance Imaging* **12**, 525-533 (2000).

- 51 Canney, M. S., Khokhlova, V. A., Bessonova, O. V., Bailey, M. R. & Crum, L. A. Shock-induced heating and millisecond boiling in gels and tissue due to high intensity focused ultrasound. *Ultrasound in medicine & biology* **36**, 250-267 (2010).
- 52 Top, A., Hamarneh, G. & Abugharbieh, R. in *Medical Image Computing and Computer-Assisted Intervention—MICCAI 2011* 603-610 (Springer, 2011).
- 53 Top, A., Hamarneh, G. & Abugharbieh, R. in *Medical Computer Vision. Recognition Techniques and Applications in Medical Imaging* 204-213 (Springer, 2010).
- 54 Sapareto, S. A. & Dewey, W. C. Thermal dose determination in cancer therapy. *International Journal of Radiation Oncology Biology Physics* **10**, 787-800 (1984).
- 55 Dewhurst, M., Viglianti, B., Lora-Michiels, M., Hanson, M. & Hoopes, P. Basic principles of thermal dosimetry and thermal thresholds for tissue damage from hyperthermia. *International Journal of Hyperthermia* **19**, 267-294 (2003).
- 56 Khokhlova, T. D. *et al.* Controlled tissue emulsification produced by high intensity focused ultrasound shock waves and millisecond boiling. *The Journal of the Acoustical Society of America* **130**, 3498-3510 (2011).

Chapter 3

Mechanical Fractionation of Tissues using Microsecond-Long HIFU Pulses on a Clinical MR-HIFU System



This chapter is based on:

Eranki, Avinash, et al. "Mechanical fractionation of tissues using microsecond-long HIFU pulses on a clinical MR-HIFU system." *International Journal of Hyperthermia* 34.8 (2018): 1213-1224.

Eranki, Avinash, et al. "Quantification of Cavitation Histotripsy Lesion Volumes on a Clinical MR-HIFU System" *Focused Ultrasound Symposium* (2016).

Chapter 3

3.1 Abstract

Purpose: High intensity focused ultrasound (HIFU) can non-invasively treat tumors with minimal or no damage to intervening tissues. While continuous-wave HIFU thermally ablates target tissue, the effect of hundreds of microsecond-long pulsed sonications cause mechanically fractionated lesions, which is examined in this work. Guided by the results we obtained in BH of TMP's, detailed in chapter 2, we wanted to further study and characterize sonication parameter-dependent thermal and mechanical bioeffects in multiple tissue types, to provide the foundation for future preclinical studies and facilitate clinical translation.

Methods and Materials: Acoustic power, number of cycles/pulse, sonication time, and pulse repetition frequency (PRF) were varied on a clinical magnetic resonance imaging (MRI) - guided HIFU (MR-HIFU) system. Ex vivo porcine liver, kidney, and cardiac muscle tissue samples were sonicated (3×3 grid pattern, 1 mm spacing). Temperature, thermal dose, and T2 relaxation times were quantified using MRI. Lesions were histologically analyzed using H&E and vimentin stains for lesion structure and viability.

Results: Thermomechanical HIFU bioeffects produced distinct types of fractionated tissue lesions: solid/thermal, paste-like, and vacuolated. Sonications at 20 or 60Hz PRF generated substantial tissue damage beyond the focal region, with reduced viability on vimentin staining, whereas H&E staining indicated intact tissue. Same sonication parameters produced dissimilar lesions in different tissue types, while significant differences in temperature, thermal dose, and T2 were observed between the parameter sets.

Conclusion: Clinical MR-HIFU system was utilized to generate distinct types of lesions and to produce targeted thermomechanical bioeffects in ex vivo tissues. The results guide HIFU research on thermomechanical tissue bioeffects, inform future studies, and advice sonication parameter selection for direct tumor ablation or immunomodulation using a clinical MR-HIFU system.

3.2 Introduction

Focal or local cancer therapies using mechanical-HIFU may play roles in locally dominant disease, pain control, and for antigen presentation or enhanced T-cell maturation in combination with immunotherapy. Local treatment may be delivered with invasive open or laparoscopic surgery, or non-invasive HIFU bio-modulation. Local tumor therapies include surgery ¹ or minimally invasive therapies ² such as radiofrequency (RF) ^{3,4}, cryoablation ⁵, laser ablation ^{6,7}, microwave ablation ^{8,9}, irreversible electroporation ^{10,11}, and therapeutic ultrasound ¹²⁻¹⁴. All local therapies carry iatrogenic risks, but less invasive or non-invasive procedures may carry less risk to nearby critical structures than more invasive options, and may have less pain with quicker recovery ¹⁵⁻¹⁸.

In contrast to minimally invasive image-guided therapies, high intensity focused ultrasound (HIFU) is a non-invasive thermal therapy that precisely focuses acoustic waves on a target tissue (often cancer) within the body, heating the target to over 60°C and leading to local tissue destruction. HIFU thermal ablation has been used to treat various tumors in multiple anatomic locations including liver, kidney, breast, prostate, uterus, brain, and bone ^{12,14,19-23}. Similar to minimally invasive thermal therapy, HIFU ablation can result in thermal damage to tissues surrounding the treated region due to heat diffusion or off-target heating. This may limit HIFU clinical applicability or efficacy in certain anatomical locations and applications ^{13,24}.

Newer HIFU techniques termed cavitation cloud histotripsy (CH) ^{25,26} and boiling histotripsy (BH) ²⁷⁻²⁹ may overcome certain limitations of HIFU thermal ablation via the mechanical fractionation mechanism, which may have a more distinct and precise margin, with a sharp spatial transition from normal to dead tissue. Unlike HIFU thermal ablation that typically employs continuous wave or high duty cycle ultrasound exposures, these histotripsy approaches typically apply pulsing regimes at higher acoustic powers and lower duty cycles. In particular, BH uses millisecond-long HIFU bursts, producing shock wave fronts to repeatedly induce boiling at the focus in a short period of time ^{27,29}. On the contrary, CH uses microsecond-long low duty cycle

Chapter 3

(<5%) ultrasound pulses to initiate and maintain a dense cavitation bubble cloud ^{25,26}. Both methods result in mechanical tissue fractionation at the targeted location, likely with variable bioeffects heavily dependent upon the acoustic parameters prescribed.

For both BH and CH, b-mode ultrasound has been used in sonication planning and guidance ^{28,30}, while temperature changes around the focal region were measured using thermocouples ^{30,31}. However, thermocouples and optical temperature probes are invasive and may not be placed within the focal zone, especially at high acoustic pressures, since they could cause cavitation at the thermocouple tip, resulting in unreliable measurements or probe damage. On the other hand, magnetic resonance imaging (MRI) can be used to accurately and non-invasively plan treatment using T1-weighted and T2-weighted sequences while quantifying relative temperatures in real time, both within and around the focal region, most commonly using proton resonance frequency shift (PRFS) -based thermometry ^{29,32-34}.

Prior work has explored pulse lengths that are several milliseconds long or in the order of few tens of microseconds ^{26,27,29}. However, there is a paucity of knowledge on temperature and tissue bioeffects produced by hundreds of microsecond-long HIFU pulses at varying acoustic power, total sonication time, or PRF. Additionally, most current research involving these mechanical regimes of HIFU utilize custom built transducers and systems that may not be well characterized, leading to challenges in standardization and translation of this HIFU approach to the clinic ^{30,35}. Systematic exploration of HIFU-mediated thermomechanical bioeffects on a clinical HIFU platform could provide the requisite foundation for future preclinical histotripsy studies. Furthermore, clearer understanding of the sonication parameter-dependent bioeffects at high acoustic pressures using a clinical MR-HIFU system is a requisite to clinical translation of this technology, which may have advantages over existing thermal and mechanical clinical modalities of ablation.

Using a clinical MR-HIFU system to perform sonications with different parameter sets in three types of *ex vivo* porcine tissue, the objectives of this study were to: (i) characterize resultant

lesion types, structure, and viability, (ii) quantify area of temperature and thermal dose at the focal region, and (iii) investigate MRI T2 relaxation time -dependent change post-sonication.

3.3 Methods & Materials

3.3.1 Experiment Setup

A clinical MR-HIFU system (Sonalleve V1, Philips, Vantaa, Finland) was used for all experiments. The system is capable of precisely delivering acoustic power with both spatial and temporal control, and consists of a generator cabinet, a patient tabletop with an ultrasound transducer, and a therapy planning console with control software. The ultrasound array transducer attaches to a positioning system with 5 degrees of freedom, and is submerged in a sealed degassed water tank within the patient tabletop. The spherical shell transducer array consists of 256 elements arranged in a pseudo random fashion, with a focal length of 120 mm and an F-number of 0.938. The transducer was operated at a frequency of 1.2 MHz and the acoustic power as well as pulse parameters were controlled using the planning console. The HIFU beam propagates through an acoustic window, producing a focal point of $1.56 \times 1.53 \times 9.37$ mm in size (-6 dB of pressure)³⁶. The HIFU system is integrated with a clinical MR imaging system (Achieva 1.5T, Philips, Best, Netherlands) to perform MRI-based sonication planning and real-time temperature mapping. A passive cavitation detector (PCD) integrated at the middle of the HIFU transducer array was used to monitor for cavitation bubble activity. The center frequency of this PCD is 650 kHz, which is approximately half of the transmit frequency of 1.2 MHz, with an acquisition rate of 1 sample/500 ms.

The overall setup used for our experiments is depicted in Figure 1. A cylindrical water bath, filled with deionized and degassed water at typical internal body temperature (37.5°C) and sealed with a Mylar membrane on one end, was placed over the acoustic window. A custom holder to position and fix the tissues within the water bath was designed and 3D printed. The holder consisted of a plastic box with openings at the bottom and top surfaces to permit sonication

and exiting beam path (Fig 1). A closed-loop heating system with circulating water was custom built to maintain the tissue temperature at 37.5°C throughout the experiment. A fresh tissue sample was inserted in the holder for every sonication protocol. An acoustic absorber pad was secured 2 cm from the top of the tissue holder to prevent reflections within the water bath.

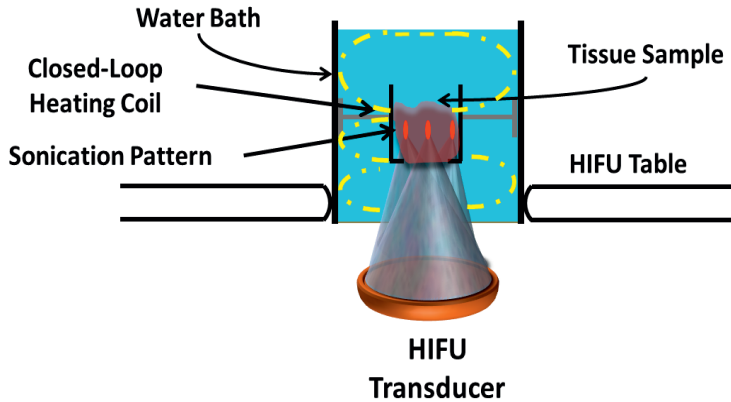


Figure 1. Experimental setup to produce lesions in ex vivo tissues on a clinical MR-HIFU system. The setup consisted of a water bath, filled with degassed water and a closed loop heating coil that circulated heated water to maintain the water bath temperature at 37.5 C. A custom designed tissue holder was positioned at a fixed distance from the transducer. The water bath was placed on the patient tabletop's acoustic window. Each tissue sample (45 mm in thick ness) was sonicated using a 3 3 grid pattern with 1 mm spacing between foci in either direction.

3.3.2 Ex vivo Tissue Preparation

Healthy adult pigs (n = 3) were euthanized on an unrelated protocol approved by the Animal Care and Use Committee. Liver, kidney, and cardiac muscle tissues were selected since they represent a broad range of biochemical tissue composition^{25,35,37}. All tissue samples were harvested within one hour of animal euthanasia, allowing for greater tissue viability preservation and decomposition control compared to abattoir-obtained tissues. These tissues were immediately cut into multiple, 45 mm thick samples to fit the tissue holder. The prepared tissue

samples were transported in a container filled with fresh phosphate buffered saline (PBS, 1x) on ice. This approach may retain cellular function and viability for approximately 72 hours³⁸. All tissue samples were degassed for two hours in a vacuum desiccant chamber at room temperature while submerged in PBS. Once degassed, the tissues were replaced in the PBS-filled container. Subsequently, the container was placed on ice, and transferred to the MRI suite.

3.3.3 MRI-based Sonication Planning and Monitoring

Relevant details on applied MRI pulse sequences are presented in Table 1. Briefly, a turbo field echo (TFE) survey for localizing the tissue sample was performed. Subsequently, a 2D fast field echo (FFE) scan was performed to check for the presence of air bubbles in the ultrasound beam path. A T2-weighted (T2W) 3D turbo spin echo (TSE) imaging sequence was used for sonication planning. MR images for thermometry were acquired in real time using a multishot RF-spoiled 2D FFE echo-planar-imaging (FFE-EPI) pulse sequence. Temperature and thermal dose maps were calculated online using the PRFS method, and displayed on the therapy planning console. Another set of T2W images with identical acquisition parameters was performed after sonication to visualize the lesion. In addition, quantitative T2 maps were acquired post-sonication using a multi-slice, multi-echo sequence with 5 echo times.

3.3.4 HIFU Sonication Parameters

Sonication locations were selected on the therapy planning console based on the T2W planning MR images. Locations 25 mm deep within the tissue were targeted in a 3 × 3 grid pattern with spatial separation of 1 mm between discrete foci (Figure 1). The 1 mm spacing was applied to obtain contiguous fractionated lesions, since 2 mm spacing as typically employed in thermal ablations³², may result in a gap (i.e., pressures lower than threshold pressure) between foci. To observe effects similar to experiments conducted *in vivo*, reference temperature for MR-thermometry was set to 37.5°C, and temperature changes were calculated relative to this baseline temperature. Both the sonication grid pattern and parameter sets (Table 2) were selected to mimic

Chapter 3

clinically relevant treatment times and volumes, while ensuring safe and consistent operation of the clinical MR-HIFU system. These sonication parameters were selected to coarsely cover ranges that were previously not explored using a clinical MR-HIFU system. Specifically, acoustic power below 500 W did not produce an observable lesion, while powers greater than 800 W risk damage to the transducer. In addition, we selected total sonication times that span wide range of current preclinical and clinical sonications. PRF was chosen to be higher than 8 Hz to compensate for shorter pulse lengths (lesion did not form for PRF below 8 Hz), while, PRF greater than 60 Hz is not feasible on this clinical MR-HIFU system due to hardware limitations. In addition, we calculated total sonication time based on the number of times the 3 × 3 grid pattern was repeated. For all parameters sets except C and D, the grid pattern was repeated 900 times. For sets C and D, respectively, the grid pattern was sonicated 300 and 1800 times. The entire set of sonication parameters were repeated thrice in liver tissue, while they were performed once in kidney and cardiac muscle tissues.

Table 1. List of MRI pulse sequences and their respective parameters applied during histotripsy experiments. Parameters were held constant for all tissue types and repetitions. TR, TE, FA, and FOV stand for repetition time, echo time, flip angle, and field of view, respectively.

MRI Sequence	Type	TR (ms)	TE (ms)	FA (°)	Voxel Size (mm)	Slices	FOV (mm)
Survey – target localization	2D TFE	3.5	1.73	25	1.47 x 2 x 10	4 axial; 4 sagittal; 4 coronal	200 x 200
Air bubble detection	2D FFE	150	15	10	1.25 x 1.25 x 2.5	10 coronal	280 x 280 x 25
T2w sonication planning	3D TSE	685	35	90	1.2 x 1.3 x 1.5	50 coronal	250 x 250 x 75
Real-time MR thermometry	2D FFE-EPI	36	19	20	2.5 x 2.5 x 7	3 coronal; 1 sagittal	400 x 310
Post-sonication T2 maps	2D TSE	1200	20 ~ 105	90	1.2 x 1.2 x 6	3 coronal	80 x 80 x 20

Table 2. Sonication parameters used in the experiments for all tissue types. Acoustic power, pulse repetition frequency, number of cycles/pulse, and total sonication time were varied. Sonication parameters varied are highlighted (†), while others were kept constant. The peak positive and negative pressure values are extracted from Kreider et al. ³⁶

Parameter Set	Acoustic Power (W)	Peak Positive Pressure (MPa)	Peak Negative Pressure (MPa)	PRF (Hz)	Number of Cycles/Pulse	Duty Cycle (%)	Total Sonication Time (s)	Energy (J)
A	800†	106.30±1.63	18.38±0.34	10	800	0.66	815.4	4349
B	700	100.97±1.51	18.40±0.55	10	1200†	1	818.1	5727
C	700	100.97±1.51	18.40±0.55	10	800	0.66	271.8†	1268
D	700	100.97±1.51	18.40±0.55	10	800	0.66	1630.8†	7610
E	700	100.97±1.51	18.40±0.55	20†	800	1.33	410.4	3830
F	700	100.97±1.51	18.40±0.55	60†	800	4	140.4	3931

3.3.5 Histology

Following sonication, tissue samples were trimmed to contain resultant lesions and fixed in 10% neutral buffered formalin for histological processing, which included paraffin embedding and histologic sectioning (5 μ m). Subsequently, these tissues were stained with hematoxylin and eosin (H&E) to investigate the structural integrity of tissues, and vimentin (Vimentin Bond RTU Primary, Leica Biosystems, Illinois, USA). Vimentin is an immunohistochemistry marker expressed in most cells of mesenchymal origin, including hepatic stem cell, kidney glomeruli, fibroblasts, endothelial cells, and smooth muscle, amongst others. Lack or absence of vimentin staining often indicates significant damage to tissue antigen and viability ^{39,40}. Briefly, the vimentin staining process involved deparaffinized tissue blocks that were rehydrated and rinsed using deionized water. This was followed by rinsing with peroxide for five minutes. Vimentin antibody was then applied, and tissue was incubated for 10 minutes. Furthermore, hematoxylin was applied as a counterstain. Finally, tissue was rinsed in peroxide and washed using deionized water.

Chapter 3

Stained tissues were imaged at 4x, 10x, and 40x magnifications (Hamamatsu NanoZoomer-XR, Shizuoka, Japan).

3.3.6 Temperature & Thermal Dose Data Analysis

The MRI-based temperature maps were analyzed using MATLAB (version R2014a, MathWorks, Natick, MA, USA). All temperature and thermal dose calculations were made within a 71 × 55 mm region-of-interest (ROI), centered on the focal region. The area of temperature greater than 45°C at the end of sonication within the coronal and sagittal planes was calculated for all samples. Anything less than 45°C for these exposure times, was considered milder hyperthermia, generally resulting in no or reversible thermal damage and vascular shutdown compared to higher temperatures (> 45°C)⁴¹⁻⁴³. Cumulative equivalent minutes at 43°C (CEM43) was used as a metric for thermal dose assessment and was calculated using the following equation:

$$TD(t) = \int_0^t R^{43-T(t)} dt$$

where t is the treatment time and R = 0.25 if T(t) < 43°C and 0.5 otherwise^{44,45}. Area of thermal dose greater than 240 CEM43 was computed for every sonication in all *ex vivo* samples.

3.3.7 Statistical Analysis

All quantitative results are reported as mean ± standard deviation (SD). Comparisons amongst parameter groups in liver tissues were performed using one-way ANOVA constrained to Bonferroni correction using GraphPad Prism (Version 5.01, GraphPad Software Inc., La Jolla, CA). For all tests, two-tailed p-values were obtained, and differences were considered significant if p<0.05.

3.4 Results

3.4.1 Effect of Sonication Parameters on Lesion Appearance and Structure

Ex vivo porcine liver was sonicated with each parameter set listed in Table 2. Lesions in all tissue samples were square in shape, resembling the planned sonication. Most sonication parameter sets produced lesions with sharp boundaries between normal and sonicated tissue. Three distinct lesion types were obtained with sonication parameter sets F, A, and D, from Table 2. Based on gross pathology, the three lesion types are:

Solid Thermal Lesions

The solid thermal lesion seen in Figure 2a2 was created using parameter set F. Even though the total duration of the sonication was relatively short, visual examination of the tissue revealed a white ring around the focal region, suggesting thermal damage. This is supported by the temperature map in Figure 2a1, showing temperatures greater than 60°C (instantaneous tissue death) in the entire sonication region. Lack of perfusion further increased thermal effects next to the sonicated region. Gross pathology image of the lesion showed mechanically fractionated center along with peripheral (apparently thermal) heating effects (Figure 2a2). H&E stain revealed hepatic lobules completely disrupted in the middle of the sonicated region, with the edge of the region presenting heterogeneity of completely and partially disrupted hepatic lobules (Figures 2a3-5).

Paste-Like Lesions

Temperature increase in the sonicated region for parameter set A did not extend beyond 50°C and was contained within the sonicated region (Figure 2b1). Figure 2b2 shows a paste-like lesion with the contents of the lesion in a semisolid state, with nominal structural integrity. Figures 2b3-5 show the focal region with partly intact paste-like tissue, along with surrounding intact tissue. The sonicated region contains mostly lysed hepatocytes with few intact hepatocytes. The number of intact cell clusters increase towards the border of this region.

Chapter 3

Vacuolated Lesions

A vacuolated lesion was obtained using sonication parameter set D, as seen in Figure 2c2. Although temperature at the sonicated region was not greater than 55°C, the area of temperature >45°C was greater than those observed with all other sonication parameters sets (Figure 2c1). The center of the focal region was completely liquefied post sonication. H&E staining revealed intact surrounding tissue, with a central region devoid of tissue structure. Figure 2c3 shows intact bile ducts less than 800 µm from the focal region. Closer examination of the border of the focal region in Figures 2c4 and 2c5 shows completely intact tissue with no cell fragments.

Mechanical Fractionation of Tissues using Microsecond-Long HIFU Pulses

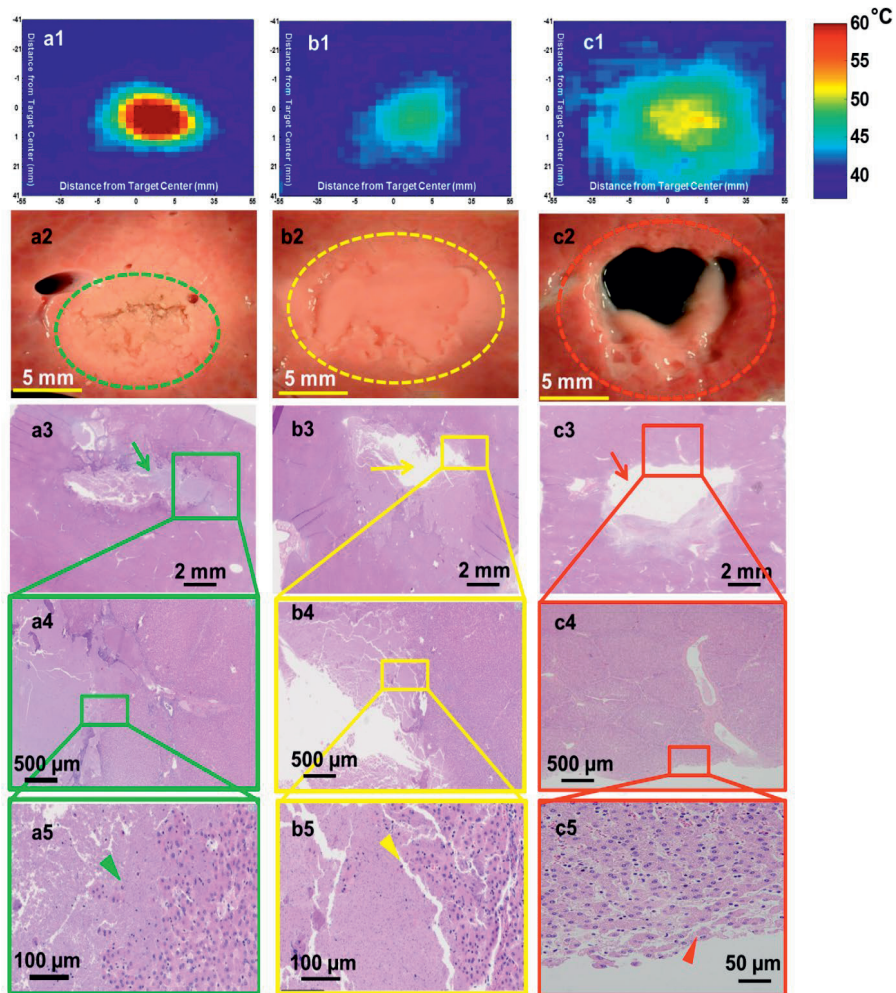


Figure 2. Lesions produced in ex vivo porcine liver tissue using sonication parameter sets F, A and D with their corresponding H&E stains are illustrated in a, b & c panels, respectively. These lesions display significantly different morphologies. a1. Thermal map showing temperatures greater than 60 C in the focal region. a2. Shows a solid thermal lesion (green dotted circle) with mechanical disruption of tissue at the centre of the focal region, surrounded by whitening of tissue. a3. Shows H&E stain with green arrow pointing to the necrosed region of liver. a5. Arrowhead pointing to individual injured cells at the edge of the treatment region. b1. Thermal map displaying temperatures no greater than 50 C at the focal region, with minimal or

Chapter 3

no temperature change surrounding this region. b2. Lesion consists of a paste-like tissue in the focal region (yellow dotted lesion) surrounded by a sharp boundary of intact tissue. b3. Shows area of missing tissue in the H&E stain due to loss of the paste during stain process. b4. Region of both intact and necroses tissue. b5. Yellow arrowhead points to hepatic cells partially or completely ruptured. c1. This lesion consisted of the greatest area of temperature, but did not have temperatures increase greater than 55 C. c2. Displays a vacuolated lesion at the focal region (red dotted circle) with intact tissue around the lesion. c3. Red arrow shows region of vacuolated tissue with intact surrounding tissue. c4&5. Region of intact tissue and vacuolated tissue with red arrowhead pointing to the edge of the lesion that is intact post sonication.

3.4.2 Tissue Viability Post Sonication: Comparison of H&E and Vimentin Staining

Immunohistochemical staining for vimentin protein was performed post sonication in all tissue samples as a surrogate marker for tissue viability (i.e., thermal injury denatures proteins), and compared to H&E stain for tissue integrity and architecture. To illustrate the difference between H&E (Figure 3a & c) and vimentin (Figure 3b & d), staining, parameter sets C and F in liver tissue are presented. The tissue sonicated with parameter set F displays mechanical tissue fractionation at the focal region that is surrounded by whitening of tissue, an indicator of thermal damage (Figure 3a & b). Figure 3a1 shows H&E stain with partially intact tissue at focal region and intact surrounding tissue (Figure 3a2 & 3a3). Figure 3b shows vimentin stain within the same region of tissue following sonication with parameter set F. Contrary to the finding with H&E staining, there is a region of intact but presumably injured or non-viable hepatic lobules, inferred from the lack of vimentin staining in Figure 3b1. Figure 3b2 shows a region closer to the sonicated region that is injured (yellow arrowhead), with transition region leading to an uninjured hepatic lobule (yellow arrow). It is important to note that although the hepatic lobules appear intact, loss of vimentin staining may be a surrogate for lack of tissue viability, which may ultimately lead to necrosis.

The right panel in Figure 3 shows another liver tissue sample sonicated with parameter set C. The H&E staining seen in Figure 3c1 through 3c3 show no disrupted hepatic lobules or

Mechanical Fractionation of Tissues using Microsecond-Long HIFU Pulses

cells beyond the center of the focal region, while the center of the focal region consists mostly of coagulative necrosis of hepatocytes, with a few intact cells. Vimentin staining of this tissue in Figure 3d shows normal staining beyond the sonicated region, suggesting no functional damage to immediately adjacent tissue. A closer look at the hepatic lobule at the border of the sonicated region in Figure 3d3 shows partially fractionated hepatic parenchyma, but the rest of the lobule seems to stain normally, suggesting some viability at the cellular level.

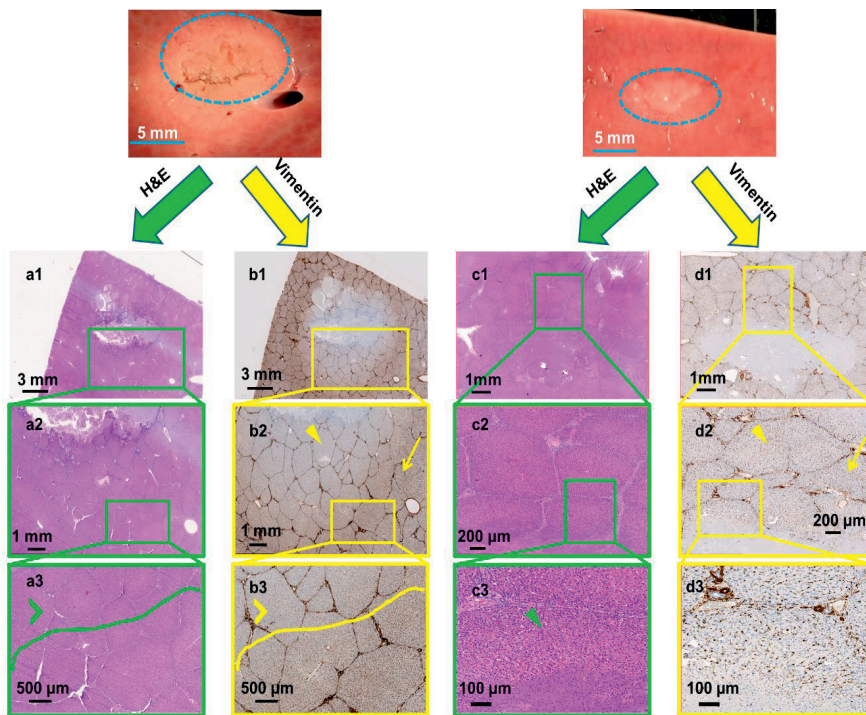


Figure 3. Gross pathology along with H&E and vimentin stains created using sonication parameter sets F (panels a & b) and C (panels c & d). Vimentin stains for mesenchymal cells and is a surrogate for tissue viability. Panel b shows substantial damage of tissue beyond the focal region (panel b2, yellow arrowhead) even though H&E indicates intact tissue (panel a3 green arrowhead). In contrast, panel c shows structurally intact tissue around the focal region and panel d depicts viable tissue in this intact region (green and yellow arrowheads in panels c3 & d2 respectively).

3.4.3 Dependence of Tissue Type on Lesion Production

Even though all tissue samples had similar thickness, most sonication parameter sets produced dissimilar lesion types in different tissues (Figure 4 is an example for sonication parameter set F). Liver tissue has partial mechanical fractionation along with surrounding thermal bioeffects. On the contrary, kidney tissue had a paste-like lesion with the contents of the lesion appearing fractionated and necrotic. Cardiac muscle tissue displayed a combination of mechanical fractionation and some thermal bioeffects along the boundary of the lesion. H&E staining of the liver tissue shows lysed tissue at the center of the sonication region with partially disrupted hepatic lobules along the border and several clusters of hepatic cells, some of them with significant cellular injury (Figures 4a1 and a2). Figure 4a3 shows several clusters of hepatic cells, with some of them partially ruptured (green arrowhead). The cortex of the kidney was structurally intact post sonication, with the center of the sonication region containing paste-like cellular contents, seen in Figure 4b1. Closer look at the contents at the center of the sonication region shows mostly lysed cells (yellow arrowhead). The lesion had sharp boundaries with vital proximal structures intact. Cardiac muscle had both mechanical and thermal damage as seen in Figure 4c. The boundary of the lesion retained its structure, while the center of the focal region contained liquefied tissue and cellular fragments, seen in Figures 4c1 and c2. Figure 4c3 shows partially intact cardiac muscle cells (blue arrowhead). Table 3 summarizes sonication parameter-dependent lesion types in *ex vivo* porcine liver, kidney, and cardiac muscle tissues. All three tissues vary in biochemical composition, density, and acoustic attenuation ⁴⁶, which may explain the variation in lesions obtained using the same sonication parameter set.

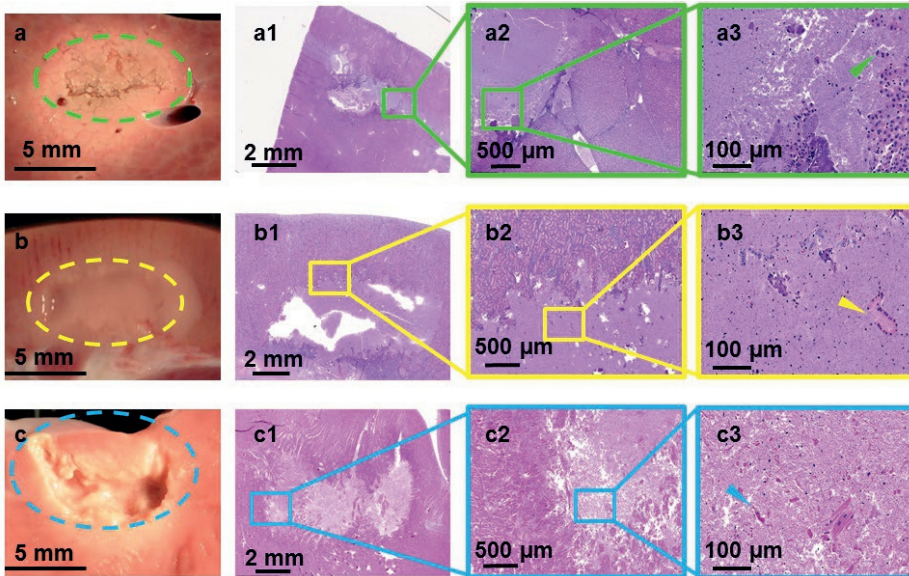


Figure 4. Gross pathology along with H&E stains of lesions produced using sonication parameter set F in porcine liver, kidney, and heart tissues in panels a, b and c, respectively. While the liver tissue expressed solid thermal damage, the kidney presented a paste-like lesion at the focal region. The cardiac muscle showed substantial mechanical fractionation, with some thermal effects along the lesion border.

3.4.4 Effect of Sonication Parameters on Temperature and Thermal Dose

Area of Temperature > 45°C

The area of temperature greater than 45°C along the coronal (Figure 5i) and sagittal (Figure 5ii) planes at the end of sonication was quantified from MR-thermometry data for all sonication parameter sets in liver tissue. Significant differences in this area were found across all sonication parameter sets in the coronal plane (overall ANOVA $p < 0.0001$). Post-hoc test reveals significant differences between parameter set D ($1958 \pm 173.4 \text{ mm}^2$) and all the other parameter sets ($p < 0.001$, Figure 5i). Additionally, significant differences were also found between parameter sets A ($841 \pm 43.9 \text{ mm}^2$) and C ($314.6 \pm 76.3 \text{ mm}^2$, $p < 0.01$), parameter sets B (962.5

Chapter 3

$\pm 141.6 \text{ mm}^2$) and C ($314.6 \pm 76.3 \text{ mm}^2$, $p < 0.001$), and parameter sets C ($314.6 \pm 76.3 \text{ mm}^2$) and E ($645.8 \pm 117.3 \text{ mm}^2$, $p < 0.001$). Along the sagittal plane, there was an overall significant difference in area of temperature ($p < 0.001$), with parameter set D ($3063 \pm 421.9 \text{ mm}^2$) being significantly different from all other parameter sets ($p < 0.001$). However, there was no significant difference in this metric between any other parameter sets (Figure 5ii).

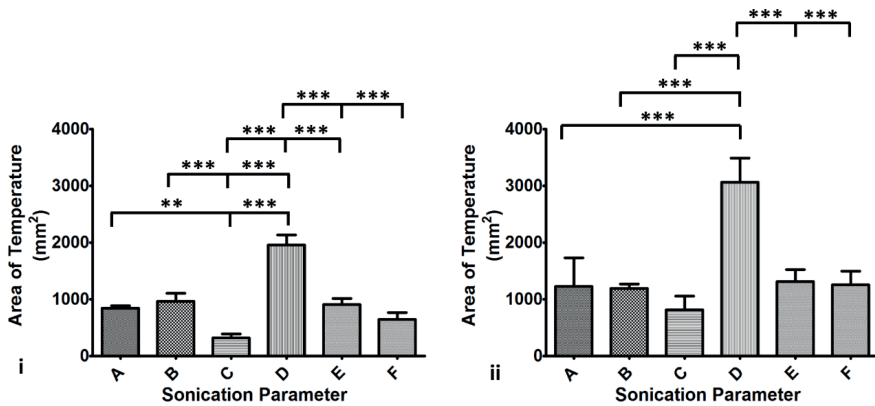


Figure 5. Column chart showing area of temperature greater than 45 C along the coronal (panel i) and sagittal (panel ii) planes. Statistically different area of temperature was found between D and all other parameter sets, consistent with measurements made along the sagittal plane. Area of temperature was higher along the sagittal plane compared to the coronal plane since the focus region is longer along the sagittal plane than in the coronal plane.

Area of Thermal Dose > 240 CEM43

The area of thermal dose > 240 CEM43, indicative of lethal tissue damage^{42,44}, along the coronal plane at the end of sonication was computed from MRI-based thermal dose data for all sonication parameter sets (Figure 6). There was an overall significant difference ($p < 0.0001$) in sampled area that experienced a thermal dose > 240CEM43 in this plane. Along the coronal plane, the area of thermal dose for parameter set D ($1106 \pm 137.5 \text{ mm}^2$) was significantly different from every other sonication parameter set. Furthermore, parameter set B (609.2 ± 313.9) was

significantly different from parameter set C ($125 \pm 59.6 \text{ mm}^2$, $p < 0.05$). Although the area of lethal thermal dose did not change significantly between parameter sets A, B, E, and F, lesions produced in liver tissue with these parameter sets were different in type and structure (Figure 6).

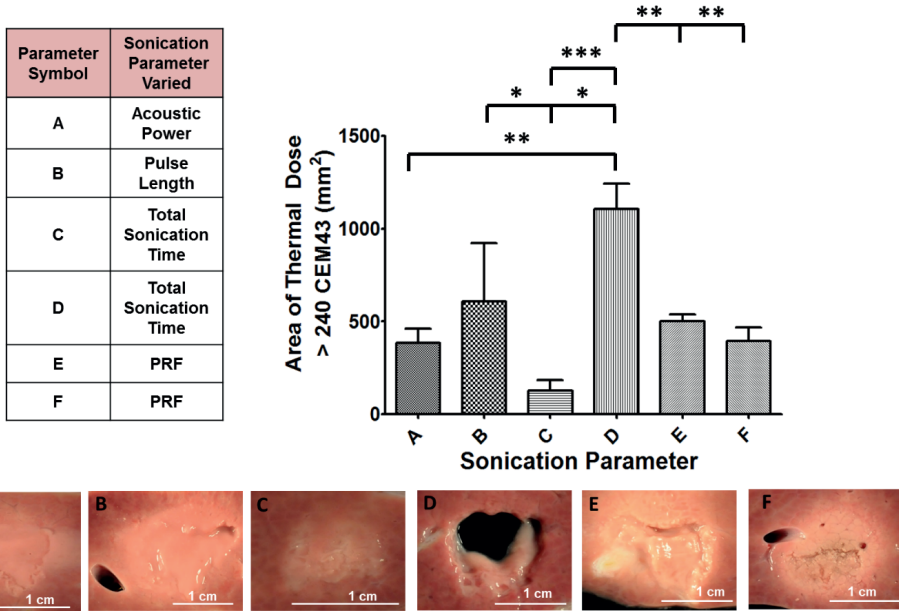


Figure 6. Summary of the varied sonication parameters along with area of lethal thermal dose and corresponding gross pathology images of liver tissue. Area of thermal dose is quantified along the coronal plane and displayed in bar graph format. Parameter set D was significantly different compared to all other parameter sets. There were additional differences between other sonication parameter sets. Although the area of lethal thermal dose was similar between parameter sets A, B, E and F, the lesions produced were different in structure, as seen in the gross pathology images.

3.4.5 Changes in T2 Relaxation Time and Lesion Appearance on MRI

Post-sonication, tissue samples were imaged using T2W MRI to assess the degree and type of damage. Lesions appeared as hyperintense regions in T2W images. However, the hyperintense region was less visible in the kidney samples and in samples with higher degree of

Chapter 3

thermal damage. Post-sonication T2W images of both heart and liver tissues sonicated with parameter sets A and D, respectively, are shown in Figure 7. MRI T2W images visualized the lesions clearly with distinct boundary (and in most samples with distinction between each sonication point), as observed in Figure 7. T2 relaxation times of sonicated and un-sonicated tissue in each sample were calculated (Table 4). Vacuolated and paste-like lesions (parameter sets D and B) produced higher T2 relaxation times compared to thermal lesions (parameter set F). T2 relaxation times inside and outside the lesion were not significantly different in liver tissue between repetitions ($p=0.5813$ and $p=0.6978$, respectively). In addition, T2 values were significantly different between within the lesion and outside the lesion for all parameter sets ($p=0.00278$). These preliminary results suggest that a clinical MRI can repeatedly differentiate mechanically fractionated tissues from untreated tissues. This result is valuable but requires further optimization and validation of MRI parameters *in vivo*, before MRI guidance may be relied upon for this task.

Table 4. T2 relaxation times inside and outside the sonication region in liver tissue for all sonication parameter sets.

Sonication Parameter Set	T2 Relaxation Time Inside Lesion (ms)	T2 Relaxation Time Outside Lesion (ms)
A	84.9±9.9	52.5±4.2
B	92.6±10.9	53.1±3.4
C	64.9±7.6	52.2±3.1
D	123.1±27.2	51.5±2.9
E	58±6.3	50.2±3.1
F	68.4±25.5	49.8±3.8

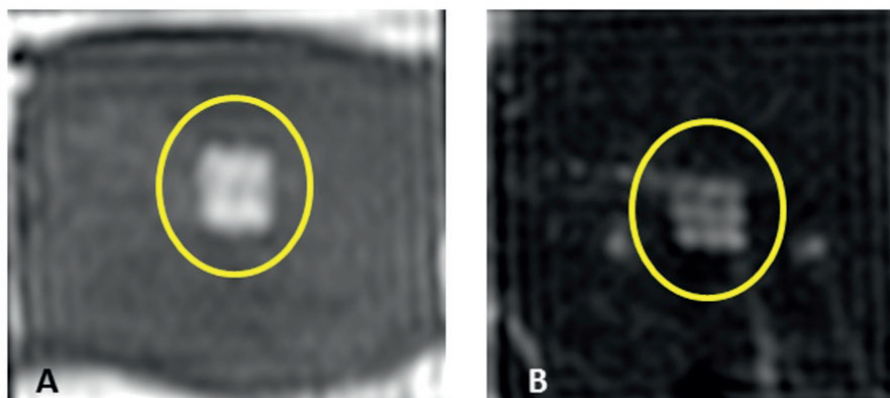


Figure 7. Examples of T2-weighted MR images of *ex vivo* porcine heart and liver obtained post-sonication using parameter sets A (panel A) and D (panel B). The images reveal a square-shaped hyperintense region (yellow circle) consistent with the square sonication grid pattern and with the square fractionated and partially liquefied lesion. Image in panel B also reveals nine spatially distinct points consistent with the sonication grid. (Colored version is available on the journal's webpage).

3.5 Discussion

Bioeffects resulting from hundreds microsecond-long pulsing regimes produced using a clinical MR-HIFU system were investigated in three different *ex vivo* porcine tissue types. Characterization of lesion type and structure relative to achieved temperature is vital in distinguishing and deconvoluting thermal bioeffects from intermingled mechanical bioeffects when utilizing microsecond long HIFU pulsing regimes. In order to understand the sonication parameter-dependent bioeffects and lesion characteristics, sonication parameters were modified such as acoustic power, PRF, number of cycles/pulse, and total sonication time. In addition, MRI quantified the area of temperature $> 45^{\circ}\text{C}$, area of thermal dose > 240 CEM43, and T2 relaxation time.

Herein, we provide observations that can inform the selection of sonication parameters to produce controllable titrate-able and predictable bioeffects in liver, kidney, and cardiac muscle on a clinical MRI HIFU system. While liver and kidney have been widely used as target tissues in

Chapter 3

HIFU research, cardiac muscle was included, since HIFU has potential cardiac specific clinical applications in, e.g., treatment of arrhythmias, septal defects and hypertrophic obstructive cardiomyopathy⁴⁷⁻⁵⁰. Sonication parameters that produce a vacuolated lesion may hold potential in precisely debulking tumors while minimizing injury to nearby critical structures (such as nerves) via a sharp, well demarcated transition zone. On the other hand, sonication parameter sets that produce a paste-like lesion may produce a depot of vital antigens close to vascularized tissue to boost and stimulate a cancer immune response, although this correlation is speculative at present (studies in progress, unreported herein).

The first part of this work focused on the effect of sonication parameter sets on the resulting lesion types. Some of the sonication parameter sets (e.g., parameter set F) produced predominantly thermal bioeffects along with some mechanical disruption of tissue. This indicates that the rate of heat deposition was greater than that of heat dissipation. The rate of heating for parameter set F was approximately 4.5 to 6.4 times greater compared to all other sets. Additionally, parameter set F had the highest PRF (60 Hz), causing more heat deposition in a short period of time at 700 W. On the other hand, some of these sonication parameters sets produced cell lysate with partially intact cells at the focal region, with little or no thermal damage. For example, parameter set C produced a paste-like fractionated lesion at the focal region with no evidence of thermal damage to surrounding tissue. These results elucidate the ability of certain sonication parameters to limit thermal tissue damage beyond the focal region. Varying pulse length, detailed in parameter set B resulted in paste-like lesion in liver with additional thermal effects in cardiac and kidney tissues. Increasing pulse length enhances resulting thermal effects in tissues due to increased energy deposition and duty cycle. Also, sonication parameters explored in this work shows no significant variation in peak negative pressure, but resulting lesion obtained in tissues were different, suggesting the role of PRF, total sonication time and pulse length in lesion production. Table 3 summarizes sonication parameter-dependent lesion types in *ex vivo* porcine tissues explored in this study. Same sonication parameter sets produced varying

bioeffects in different tissue types. This is due to tissue microstructure differences causing dissimilarities in ultrasound wave scattering, refraction and attenuation⁵¹. Specifically, it has been shown that shearing motions of molecules and viscous forces in the media, heat losses due to conduction, and chemical relaxation processes play a strong role in varied ultrasound bioeffects in different tissue types. While tissue bioeffects obtained in this study are similar to previously published work, we wanted to address the bioeffects of unexplored sonication parameters using a clinical MR-HIFU system^{25,35}.

We monitored cavitation bubble activity for sonications in all tissue samples. However, due to varying sonications parameters used and limitations with PCD settings (acquisition rate of one sample/500 ms), the cavitation activity may or may not coincide with the actual sonication ON time, and therefore the time of the activity, its duration, or its magnitude is not fully quantifiable with our setup. We are certain, however, that cavitation occurred while using all parameter sets A-F and hypothesize that the mechanical fractionation effects in tissues observed herein were due to cavitation bubble formation in combination with heat caused by incident nonlinear shock fronts. Additionally, cavitation nuclei were shown to appear at 1.2 MHz and at pulse lengths greater than 5 ms⁵². In this work, the intent was to quantify temperature and thermal dose, and to better understand the changes in tissue viability with the proposed sonication protocols. Our data suggests no substantial effect of cavitation activity on temperature measurements. Additional goals included assessment of the ability of a clinical MR-HIFU system to produce clinically relevant and repeatable lesions without any additional non-commercial hardware, making this work applicable across other research institutions. In addition, results reported in this work are repeatable using any calibrated HIFU transducer with an F number ≈ 1 . We demonstrate the potential for such an ultrasound transducer and system with a known power-pressure calibration to produce varying tissue bioeffects with temperature feedback that can be used as a guide for further preclinical and clinical work using similar HIFU transducers and sonication parameters.

Chapter 3

Thermal bioeffects were observed on gross pathology images as whitened tissue, while H&E stain showed no definite changes beyond the fractionated tissue boundary. This is in strong agreement with prior work, showing that ablative therapies may cause significant cell death while preserving cellular architecture, or thermal fixation⁵³. Additionally, H&E stain is known to be a poor indicator of thermal damage (especially in the acute setting) and shows variable findings from no change to thermal fixation, despite lethal thermal dose shown on cellular viability stains. Further H&E poorly correlates with cellular outcomes due to ablative therapies⁵⁴. This further warrants the usage of additional stains that provide vital information on cellular viability. For example, nicotinamide adenine dinucleotide-dehydrogenase (NADH-d) or tetrazolium salts have been shown to stain both viable and unviable tissue regions in ablative therapies^{35,55,56}. Depending on the type of lesions produced (semi-solid or liquid), this may result in freeze artifacts or ice crystals. In contrast, vimentin immunohistochemistry does not require freezing tissues post HIFU, thereby avoiding histopathology-related artifacts. Using vimentin stain, significant protein damage surrounding the focal area was seen, with a gradual transitioning to undamaged tissue, a finding attributable to increased heat absorption at higher PRF. Vimentin stain, in future may act as a surrogate marker for cellular and biomolecule viability following HIFU and histotripsy therapies. In the future, it is most informative when vimentin as well as additional histopathological methods are used to verify sonication parameter -dependent tissue viability beyond the focal region, at different time points post sonication.

Thermoablative techniques such as RFA have repeatedly shown diverse thermal lesion structure based on tissue and tumor type⁹. Our experiments reveal analogous results: the same HIFU sonication parameter set produced vastly dissimilar lesions in different tissues. One potential cause of pronounced thermal damage with sonication parameter set F is that porcine liver tissue has a thin band of interstitial fibrous tissue surrounding each hepatic lobule. This effect is also well pronounced in the heart tissue, possibly due to the dense anatomical structure of the cardiac muscle. These tissue structures may result in significant heat deposition, with little scope

for dissipation, leading to enhanced thermal bioeffects. Although all three tissue types exhibited different lesion types, the center of the focal region was partially lysed. The lysed lesion contents may locally spill cytoplasmic and membrane proteins to blood and lymphatic vessels that deliver antigen presenting cells or other immunocytes and cytokines. The variable effects of sonication parameters on different tissues may be in part related to tissue elasticity, attenuation, and density. Tissue mechanical fractionation effects may well be optimized to maximize an immune response in terms of antigen presentation without or with less thermal denaturation of the requisite proteins. This ability to titrate bioeffects based upon HIFU parameters could be a powerful tool for the oncologist or immunologist hoping to optimize, calibrate, or personalize therapy for a specific tumor type, tissue, or patient.

Sonication related temperature changes shed light on changes in bioeffects in various tissues. Specifically, we compared area of temperature $> 45^{\circ}\text{C}$ and area of thermal dose > 240 CEM43 for all sonication parameters. Temperature $> 45^{\circ}\text{C}$ was specifically chosen since it is shown to result in long term thermal effects including tissue necrosis and vascular shutdown^{41,43}. Analysis of both temperature and overall thermal dose allows better understanding and prediction of bioeffects. For example, parameter sets A and C produced similar thermal doses but significantly different temperature profiles in liver. The subsequent lesions were vastly different, with parameter set A producing a paste-like lesion and C causing a thermal lesion. In general, quantification of both area of temperature and lethal thermal doses and its correlation with lesion types and bioeffects could potentially guide selection of parameters for future use.

T2W MRI of the tissue samples was adequate to plan sonications in all three tissue types. Moreover, on post-sonication T2W MRI the HIFU produced lesions demonstrated higher signal intensity as compared to unsonicated tissue. Tissue fractionation or changes in tissue structure have been shown to produce changes in T2 relaxation time^{57,58}. Similar observations were made in our experiments due to tissue structure changes to semi-solid or liquefied debris, causing an increase in T2 signal intensity. These preliminary studies also illustrate the ability of MRI to

Chapter 3

differentiate fractionated from unfractionated and thermal lesions. Additionally, T2 relaxation times reported in table 4 match closely with previously reported values^{59,60}. Although in this study the same MR imaging parameters were applied for all tissue types, future studies may optimize these parameters for different tissue types. Finally, additional studies are needed to define a meaningful relationship between T2 relaxation time and the degree of tissue fractionation, liquefaction, or thermal damage.

In this work, we used MRI to plan sonications and to quantify temperature as well as cumulative thermal dose in real time. Although there are limitations in absolute temperature measurements (in terms of scale and location), these limitations in spatial and temporal imaging resolution and sonication pattern were equally distributed for all ultrasound exposure parameters, thus hopefully providing a framework for relative comparison amongst groups. In addition, this approach is applicable when the update time is short compared to the time required for a significant change in temperature during treatment. Also, tissue viability has been reported *in vivo* to change over a period of time post sonication^{53,54}. Therefore, it may be valuable to study the effects of varying tissue viability post sonication using the vimentin stain.

3.6 Conclusion

Differing prescriptions for acoustic parameters in this experimental work characterizes the resulting lesion types, structure, and viability, tissue temperature and thermal dose, and MRI T2 relaxation times in three types of *ex vivo* porcine tissues using a clinical MR-HIFU system. These findings are suggestive of mechanisms that may be modulated for noninvasive oncology therapies. Hundreds of microsecond-long HIFU pulses can produce varying lesion types in different tissues, and a clinical MRI system can differentiate the resulting mechanically fractionated from unfractionated regions. This work may inform the selection of sonication parameters to produce controllable thermomechanical bioeffects in liver, kidney, and cardiac muscle, and facilitate clinical exploration of this HIFU technique. Successful clinical translation of

Mechanical Fractionation of Tissues using Microsecond-Long HIFU Pulses

this technique will depend on assessing the sonication parameter –dependent thermomechanical bioeffects and immune responses in a suitable preclinical *in vivo* model.

3.7 References

- 1 van Doorn, R. C. *et al.* Resectable retroperitoneal soft tissue sarcomas. The effect of extent of resection and postoperative radiation therapy on local tumor control. *Cancer* **73**, 637-642 (1994).
- 2 Gelet, A. *et al.* Transrectal high-intensity focused ultrasound: minimally invasive therapy of localized prostate cancer. *Journal of Endourology* **14**, 519-528 (2000).
- 3 Dupuy, D. E. *et al.* Percutaneous radiofrequency ablation of malignancies in the lung. *American Journal of Roentgenology* **174**, 57-59 (2000).
- 4 Gervais, D. A. *et al.* Radio-frequency Ablation of Renal Cell Carcinoma: Early Clinical Experience 1. *Radiology* **217**, 665-672 (2000).
- 5 Gill, I. S. *et al.* Renal cryoablation: outcome at 3 years. *The Journal of urology* **173**, 1903-1907 (2005).
- 6 Gangi, A. *et al.* Osteoid Osteoma: Percutaneous Laser Ablation and Follow-up in 114 Patients 1. *Radiology* **242**, 293-301 (2007).
- 7 Pacella, C. M. *et al.* Thyroid tissue: us-guided percutaneous interstitial laser ablation—a feasibility study 1. *Radiology* **217**, 673-677 (2000).
- 8 Wright, A. S., Lee Jr, F. T. & Mahvi, D. M. Hepatic microwave ablation with multiple antennae results in synergistically larger zones of coagulation necrosis. *Annals of Surgical Oncology* **10**, 275-283 (2003).
- 9 Brace, C. L. Radiofrequency and Microwave Ablation of the Liver, Lung, Kidney, and Bone: What Are the Differences? *Current Problems in Diagnostic Radiology* **38**, 135-143 (2009).
- 10 Davalos, R. V., Mir, L. & Rubinsky, B. Tissue ablation with irreversible electroporation. *Annals of biomedical engineering* **33**, 223-231 (2005).
- 11 Thomson, K. R. *et al.* Investigation of the safety of irreversible electroporation in humans. *Journal of Vascular and Interventional Radiology* **22**, 611-621 (2011).
- 12 Illing, R. *et al.* The safety and feasibility of extracorporeal high-intensity focused ultrasound (HIFU) for the treatment of liver and kidney tumours in a Western population. *British journal of cancer* **93**, 890-895 (2005).
- 13 Poissonnier, L. *et al.* Control of prostate cancer by transrectal HIFU in 227 patients. *European urology* **51**, 381-387 (2007).
- 14 Huisman, M. *et al.* Feasibility of volumetric MRI-guided high intensity focused ultrasound (MR-HIFU) for painful bone metastases. *J Ther Ultrasound* **2**, b51 (2014).
- 15 Johnson, D. B. *et al.* Defining the complications of cryoablation and radio frequency ablation of small renal tumors: a multi-institutional review. *The Journal of urology* **172**, 874-877 (2004).
- 16 Livraghi, T. *et al.* Treatment of Focal Liver Tumors with Percutaneous Radio-frequency Ablation: Complications Encountered in a Multicenter Study 1. *Radiology* **226**, 441-451 (2003).
- 17 Rhim, H. *et al.* Radiofrequency Thermal Ablation of Abdominal Tumors: Lessons Learned from Complications 1. *Radiographics* **24**, 41-52 (2004).
- 18 Lawrence, V. A. *et al.* Incidence and hospital stay for cardiac and pulmonary complications after abdominal surgery. *Journal of general internal medicine* **10**, 671-678 (1995).
- 19 Chapman, A. & Ter Haar, G. Thermal ablation of uterine fibroids using MR-guided focused ultrasound—a truly non-invasive treatment modality. *European radiology* **17**, 2505-2511 (2007).
- 20 Kim, Y. S. *et al.* Volumetric MR-HIFU ablation of uterine fibroids: role of treatment cell size in the improvement of energy efficiency. *European journal of radiology* **81**, 3652-3659, doi:10.1016/j.ejrad.2011.09.005 (2012).
- 21 Chen, W. & Zhou, K. High-intensity focused ultrasound ablation: a new strategy to manage primary bone tumors. *Current Opinion in Orthopaedics* **16**, 494-500 (2005).
- 22 Yarmolenko, P. S. *et al.* Technical aspects of osteoid osteoma ablation in children using MR-guided high intensity focussed ultrasound. *International Journal of Hyperthermia*, 1-10 (2017).
- 23 Sharma, K. V. *et al.* Comparison of noninvasive high-intensity focused ultrasound with radiofrequency ablation of osteoid osteoma. *The Journal of pediatrics* **190**, 222-228. e221 (2017).
- 24 Chaussy, C. & Thüroff, S. Results and side effects of high-intensity focused ultrasound in localized prostate cancer. *Journal of Endourology* **15**, 437-440 (2001).
- 25 Vlaisavljevich, E. *et al.* Histotripsy-induced cavitation cloud initiation thresholds in tissues of different mechanical properties. *Ultrasonics, Ferroelectrics, and Frequency Control, IEEE Transactions on* **61**, 341-352 (2014).

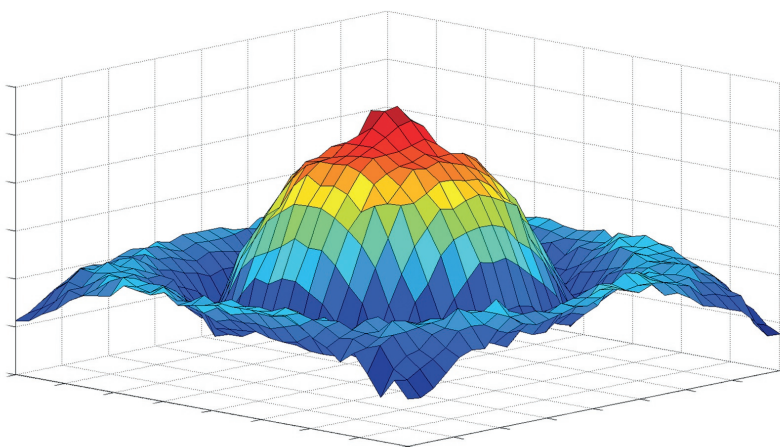
- 26 Xu, Z., Hall, T. L., Fowlkes, J. B. & Cain, C. A. Effects of acoustic parameters on bubble cloud dynamics in ultrasound tissue erosion (histotripsy). *The Journal of the Acoustical Society of America* **122**, 229-236 (2007).
- 27 Canney, M. S., Khokhlova, V. A., Bessonova, O. V., Bailey, M. R. & Crum, L. A. Shock-induced heating and millisecond boiling in gels and tissue due to high intensity focused ultrasound. *Ultrasound in medicine & biology* **36**, 250-267 (2010).
- 28 Khokhlova, T. D. *et al.* Controlled tissue emulsification produced by high intensity focused ultrasound shock waves and millisecond boiling. *The Journal of the Acoustical Society of America* **130**, 3498-3510 (2011).
- 29 Eranki, A. *et al.* Boiling histotripsy lesion characterization on a clinical magnetic resonance imaging-guided high intensity focused ultrasound system. *PLoS one* **12**, e0173867 (2017).
- 30 Vlasisavljevic, E. *et al.* Image-guided non-invasive ultrasound liver ablation using histotripsy: feasibility study in an in vivo porcine model. *Ultrasound Med Biol* **39**, 1398-1409, doi:10.1016/j.ultrasmedbio.2013.02.005 (2013).
- 31 Kieran, K. *et al.* Refining histotripsy: defining the parameter space for the creation of nonthermal lesions with high intensity, pulsed focused ultrasound of the in vitro kidney. *The Journal of urology* **178**, 672-676 (2007).
- 32 Köhler, M. O. *et al.* Volumetric HIFU ablation under 3D guidance of rapid MRI thermometry. *Medical physics* **36**, 3521-3535 (2009).
- 33 Quesson, B. *et al.* A method for MRI guidance of intercostal high intensity focused ultrasound ablation in the liver. *Medical physics* **37**, 2533-2540 (2010).
- 34 Rieke, V. & Butts Pauly, K. MR thermometry. *Journal of Magnetic Resonance Imaging* **27**, 376-390 (2008).
- 35 Wang, Y.-N., Khokhlova, T., Bailey, M., Hwang, J. H. & Khokhlova, V. Histological and biochemical analysis of mechanical and thermal bioeffects in boiling histotripsy lesions induced by high intensity focused ultrasound. *Ultrasound in medicine & biology* **39**, 424-438 (2013).
- 36 Kreider, W. *et al.* Characterization of a multi-element clinical HIFU system using acoustic holography and nonlinear modeling. *Ultrasonics, Ferroelectrics, and Frequency Control, IEEE Transactions on* **60**, 1683-1698 (2013).
- 37 Häcker, A. *et al.* Multiple high-intensity focused ultrasound probes for kidney-tissue ablation. *Journal of Endourology* **19**, 1036-1040 (2005).
- 38 Lam, F., Mavor, A., Potts, D. & Giles, G. Improved 72-hour renal preservation with phosphate-buffered sucrose. *Transplantation* **47**, 767-770 (1989).
- 39 Battifora, H. Assessment of antigen damage in immunohistochemistry: the vimentin internal control. *American journal of clinical pathology* **96**, 669-671 (1991).
- 40 Hayat, M. A. *Handbook of Immunohistochemistry and in Situ Hybridization of Human Carcinomas: Molecular Pathology, Colorectal Carcinoma, and Prostate Carcinoma*. Vol. 2 (Academic Press, 2005).
- 41 Partanen, A. *et al.* Mild hyperthermia with magnetic resonance-guided high-intensity focused ultrasound for applications in drug delivery. *International journal of hyperthermia* **28**, 320-336 (2012).
- 42 Yarmolenko, P. S. *et al.* Thresholds for thermal damage to normal tissues: an update. *International Journal of Hyperthermia* **27**, 320-343 (2011).
- 43 Gasselhuber, A. *et al.* Targeted drug delivery by high intensity focused ultrasound mediated hyperthermia combined with temperature-sensitive liposomes: Computational modelling and preliminary in vivo validation. *International Journal of Hyperthermia* **28**, 337-348 (2012).
- 44 Sapareto, S. A. & Dewey, W. C. Thermal dose determination in cancer therapy. *International Journal of Radiation Oncology Biology Physics* **10**, 787-800 (1984).
- 45 Dewhirst, M., Viglianti, B., Lora-Michiels, M., Hanson, M. & Hoopes, P. Basic principles of thermal dosimetry and thermal thresholds for tissue damage from hyperthermia. *International Journal of Hyperthermia* **19**, 267-294 (2003).
- 46 Duck, F. A. *Physical properties of tissues: a comprehensive reference book*. (Academic press, 2013).
- 47 Swaminathan, A. *et al.* Feasibility of noninvasive 3 T MRI-guided myocardial ablation with high intensity focused ultrasound. *Journal of Cardiovascular Magnetic Resonance* **11**, O86 (2009).

Chapter 3

- 48 Wu, Q. *et al.* Noninvasive cardiac arrhythmia therapy using High-Intensity Focused Ultrasound (HIFU) ablation. *International journal of cardiology* **166**, e28-e30 (2013).
- 49 Yamashita, H. *et al.* Computer-aided delivery of high-intensity focused ultrasound (HIFU) for creation of an atrial septal defect in vivo. *Medical Imaging and Augmented Reality*, 300-310 (2008).
- 50 Engel, D. J. *et al.* Myocardial lesion formation using high-intensity focused ultrasound. *Journal of the American Society of Echocardiography* **19**, 932-937 (2006).
- 51 Luo, L., Molnar, J., Ding, H., Lv, X. & Spengler, G. Ultrasound absorption and entropy production in biological tissue: a novel approach to anticancer therapy. *Diagnostic Pathology* **1**, 35 (2006).
- 52 Khokhlova, T. D. *et al.* Dependence of Boiling Histotripsy Treatment Efficiency on HIFU Frequency and Focal Pressure Levels. *Ultrasound in Medicine and Biology* **43**, 1975-1985 (2017).
- 53 Margulis, V. *et al.* Acute histologic effects of temperature-based radiofrequency ablation on renal tumor pathologic interpretation. *Urology* **64**, 660-663 (2004).
- 54 Stern, J. M., Anderson, J. K., Lotan, Y., Park, S. & Caddeu, J. A. Nicotinamide adenine dinucleotide staining immediately following radio frequency ablation of renal tumors—is a positive stain synonymous with ablative failure? *The Journal of urology* **176**, 1969-1972 (2006).
- 55 Date, R. S. *et al.* Development and validation of an experimental model for the assessment of radiofrequency ablation of pancreatic parenchyma. *Pancreas* **30**, 266-271 (2005).
- 56 Scudamore, C. H. *et al.* Radiofrequency ablation followed by resection of malignant liver tumors. *The american journal of surgery* **177**, 411-417 (1999).
- 57 Allen, S. P., Hernandez-Garcia, L., Cain, C. A. & Hall, T. L. MR-based detection of individual histotripsy bubble clouds formed in tissues and phantoms. *Magnetic resonance in medicine* **76**, 1486-1493 (2016).
- 58 Partanen, A. *et al.* in *International Symposium for Therapeutic Ultrasound*.
- 59 Hadjisavvas, V., Ioannides, K., Komodromos, M., Mylonas, N. & Damianou, C. Evaluation of the contrast between tissues and thermal lesions in rabbit in vivo produced by high intensity focused ultrasound using fast spin echo MRI sequences. *Journal of Biomedical Science and Engineering* **4**, 51 (2011).
- 60 De Bazelaire, C. M., Duhamel, G. D., Rofsky, N. M. & Alsop, D. C. MR imaging relaxation times of abdominal and pelvic tissues measured in vivo at 3.0 T: preliminary results. *Radiology* **230**, 652-659 (2004).

Chapter 4

Tissue-mimicking thermochromic phantom for characterization of HIFU devices and applications



This chapter is based on:

Eranki A, Mikhail A.S, Negussie A.H, Katti P, Wood B.J, Partanen A. "Tissue-mimicking thermochromic phantom for characterization of HIFU devices and applications." *International Journal of Hyperthermia*. 2019 Jan 1;36(1):518-29.

Chapter 4

4.1 Abstract

Purpose: Tissue-mimicking phantoms (TMPs) are synthetic materials designed to replicate properties of biological tissues. There is a need to quantify temperature changes following ultrasound or magnetic resonance imaging-guided high intensity focused ultrasound (MR-HIFU). This work describes development, characterization, and evaluation of tissue-mimicking thermochromic phantom (TMTCP) for direct visualization and quantification of HIFU heating. The objectives were to 1) develop an MR-imageable, HIFU-compatible TMTCP that reports absolute temperatures, 2) characterize TMTCP physical properties, and 3) examine TMTCP color change after HIFU.

Methods and Materials: A TMTCP was prepared containing thermochromic ink, silicon dioxide, and bovine serum albumin and its properties were quantified. A clinical MRI-guided and a preclinical US-guided HIFU system were used to perform sonications in TMTCP. MRI thermometry was performed during HIFU, followed by T2-weighted MRI post-HIFU. Locations of color and signal intensity change were compared to the sonication plan and to MRI temperature maps.

Results: TMTCP properties were comparable to those in human soft tissues. Upon heating, the TMTCP exhibited an incremental but permanent color change for temperatures between 45 and 70°C. For HIFU sonications the TMTCP revealed spatially sharp regions of color change at the target locations, correlating with MRI thermometry and hypointense regions on T2-weighted MRI. TMTCP-based assessment of various HIFU applications was also demonstrated.

Conclusion: We developed a novel MR-imageable and HIFU-compatible TMTCP to characterize HIFU heating without MRI or thermocouples. The HIFU-optimized TMTCP reports absolute temperatures and ablation zone geometry with high spatial resolution. Consequently, the TMTCP can be used to evaluate HIFU heating and may provide an *in vitro* tool for peak temperature assessment, and reduce preclinical *in vivo* requirements for clinical translation.

4.2 Introduction

Tissue-mimicking phantoms (TMPs) are synthetic materials designed to mimic the properties of biological tissues, and are commonly used to evaluate, calibrate, characterize, and assess medical devices, including thermal therapy applicators. TMPs are also used in preclinical research as an alternative to *ex vivo* tissues and organs, as TMPs possess several advantages. These include superior availability and shelf life, high structural uniformity, and customizability. In addition, TMPs provide a test environment for quality assurance (QA), operator training, and optimization of therapy protocols without necessitating animal or human patients.

High intensity focused ultrasound (HIFU) is a therapeutic modality useful for a wide variety of clinical applications, and is capable of non-invasive, volumetric tissue heating to induce targeted and localized thermal ablation, mild hyperthermia, and/or mechanical fractionation¹⁻⁴. HIFU is generally performed under magnetic resonance imaging (MR-HIFU) or ultrasound imaging (US-HIFU) guidance⁵⁻⁹. A suitable TMP for HIFU applications should be MR and US compatible and imageable, and possess similar physical, acoustic, and thermal properties as human tissues. These properties include mass density, speed of sound, acoustic attenuation, thermal conductivity, and thermal diffusivity. An ideal TMP to characterize and optimize HIFU devices, parameters, and sonication protocols, and to perform QA, should also provide a direct indication of temperature elevation or absolute temperature as well as recapitulate volumetric, spatial heating patterns.

Several HIFU TMP formulations based on agar, gelatin, or polyacrylamide have been reported that often include additives to adjust TMP thermal and acoustic properties to be comparable to human soft tissues¹⁰⁻¹⁵. For example, the TMP acoustic attenuation and speed of sound may be adjusted via the addition of silicon dioxide particles, condensed milk, bovine serum albumin, corn syrup, glass beads, intralipid, graphite, or propanol¹⁶⁻¹⁹. Nevertheless, phantoms made with these materials typically do not provide a direct means for quantifying absolute temperatures or changes in temperature during or following HIFU heating.

Chapter 4

Accurate and quantitative evaluation of HIFU-generated temperature elevation and heating patterns generally require the insertion of thermocouples or fiber-optic temperature probes, or the use of MRI-based temperature mapping methods^{8,20-22}. However, probe placement at or adjacent to the HIFU focus interferes with the acoustic field, and can disrupt HIFU energy delivery and cause damage to the probe tip, resulting in inaccurate measurement of temperature^{23,24}, necessitating the need for thermal models to estimate HIFU focal zone temperatures. On the other hand, MRI thermometry is not always available, feasible, or cost effective, and US-HIFU devices or preclinical HIFU devices may not be MRI compatible, prohibiting the use of MRI for immediate and direct temperature assessment.

One approach to visualize thermal lesions in a TMP is by incorporation of bovine serum albumin (BSA) due to its coagulation and characteristic opacification upon heating (also observed via changes in MRI signal intensity and/or T2 relaxation time)^{17,25,26}. While the coagulation threshold temperature can be adjusted by altering the pH of the phantom¹⁷, BSA-based TMPs generally do not report on absolute temperatures.

Thermochromic materials possess the ability to change color based on temperature. The change in color can be permanent or reversible, and with or without intermediate stages (colors). Several different materials may be used to achieve color changes over a range of temperatures including liquid crystals, leuco dyes, or inks²⁷⁻²⁹. For example, a heat sensitive phantom utilizing thermochromic liquid crystals has been recently developed for HIFU QA³⁰. This phantom consists of a layer of thermochromic material on top of an absorbing disc, but is not tissue-mimicking and does not inform on volumetric spatial heating patterns. In addition, a tissue-mimicking thermochromic phantom (TMTCP) material that reports on HIFU heating patterns has been described³¹. This TMTCP incorporates a thermochromic material to produce a reversible change upon heating. However, the reversible nature of the color change requires rapid analysis in order to inform on temperatures before color reversal. Furthermore, the color change threshold (50°C)

Tissue-mimicking thermochromic phantom for characterization of HIFU devices and applications of this phantom is low for thermal ablation and the color change process is affected by a hysteresis effect.

Our team previously reported a TMTCP gel formulation that permanently changes color upon heating. We characterized its ability to provide quantitative and absolute measurements over a range of temperatures, and evaluated its applicability in radiofrequency ablation^{27,28}. In this study, we tailored the TMTCP gel formulation for HIFU use and evaluated its applicability in characterization of HIFU devices, sonication parameters, and heating protocols. Specifically, the objectives of this study were to: 1) Develop an MR-imageable and HIFU-compatible TMTCP material; 2) characterize its physical, thermal, and acoustic properties as well as its pre- and post-HIFU T2 relaxation time; and 3) examine TMTCP performance by analyzing HIFU-mediated heat deposition and spatial distribution through MRI and visual assessment of color change using two different HIFU systems.

4.3 Methods & Materials

4.3.1 TMTCP preparation

The acrylamide-based TMTCP material was prepared as previously described with the addition of silicon dioxide and BSA to impart ultrasound attenuation and MRI signal effects (coagulation of BSA results in T2 relaxation time change)²⁷. Briefly, degassed, de-ionized water was mixed under a fume hood with an aqueous solution of 40% (w/v) acrylamide/bis-acrylamide (VWR International, Secaucus, NJ). Thermochromic ink (MB Magenta NH 60°C concentrate, 5% v/v; LCR Hallcrest, LLC, Glenview) that changes color from white to magenta was added to this mixture. Bovine serum albumin (BSA, 3% w/v; Sigma Aldrich, Milwaukee, WI), and silicon dioxide (1.1% w/v; Sigma Aldrich, Milwaukee, WI) were also added. Finally, ammonium persulfate (APS, Sigma Aldrich, Milwaukee, WI) and N, N, N', N'-tetramethylethylenediamine (TEMED, Sigma Aldrich, Milwaukee, WI) were added to initiate polymerization and to act as a catalyst,

Chapter 4

respectively. All ingredients were kept and mixed at room temperature, and the solution was stirred until ingredients were completely dissolved (~ 15-20 minutes). This solution was then poured into 200 mL cylindrical molds, 706 mL petri dishes, or 4 mL glass vials, sealed, cooled overnight, and kept at 4°C until use. Preparation of a TMTCP batch generally took 30 - 40 minutes. The standard TMTCP formulation for HIFU use is summarized in Table 1.

4.3.2 Measurement of TMTCP properties

In preparation for ultrasonic attenuation and speed of sound measurements, TMTCP phantoms were formed inside custom-constructed, 200 mL cylindrical plastic molds with taut, acoustically transparent Mylar sheets secured at each end. Speed of sound and attenuation measurements were performed using an ultrasonic time-delay spectrometry (TDS) system as previously described by Gammell et al.³². Briefly, a 13-mm diameter, 10-MHz planar source transducer (Valpey Fisher Corp., Hopkinton, MA) transmitted a down-swept sine wave signal from 10 to 0 MHz in 0.1 s. A 6-mm diameter, 5-MHz planar receiving transducer (Valpey Fisher Corp.), located 30 cm from the transmitter, distinguished arrivals with different propagation delays by their frequency offset relative to the transmitted signal using a narrowband swept filter.

The attenuation (insertion loss) was measured in three TMTCP samples, as described by Madsen et al.³³. The spectra (in dB) transmitted through the custom molds filled with deionized water and TMTCP material were subtracted to eliminate reflection losses at the anterior and posterior Mylar interfaces, the latter located 1 cm from the receiver. Speed of sound measurements were obtained in the same three TMTCP samples by using the temperature dependent speed of sound in water as the substitution reference³⁴. Measurements were taken at four spatially separate locations in the phantom (5 mm apart) at ambient temperature (26.3°C), and each signal was averaged 64 times.

Thermal conductivity and thermal diffusivity of TMTCP were measured from three samples using a thermal property analyzer (KD-2 Pro, Decagon Devices, Pullman, WA). In addition, mass

Tissue-mimicking thermochromic phantom for characterization of HIFU devices and applications density of the TMTCP material was determined using the Archimedes' principle. Briefly, phantom samples ($N = 5$; 2 cm diameter) cut from the 200 mL cylindrical phantoms were submerged in water and the density was measured in triplicate using a balance equipped with a density measurement kit (Mettler Toledo, VWR International, Batavia, IL). Finally, acoustic impedance was determined by multiplying the density and the speed of sound of TMTCP material³⁵. For all property measurement results, the average \pm one standard deviation is provided.

4.3.3 Characterization of TMTCP color change

Color vs. temperature calibration of the TMTCP material was performed as previously described²⁸. Briefly, capped glass vials containing 4 mL of TMTCP gel were submerged in a water bath in triplicate and incubated for 10 minutes at temperatures ranging from 35 to 70°C, as measured by calibrated optical temperature probes (diameter = 0.56 mm, Luxtron 3100, LumaSense Technologies, Santa Clara, CA). The vials were subsequently removed from the water bath and allowed to cool to room temperature (25°C) before color analysis.

Vials containing TMTCP gel were then photographed at a standard color temperature of 5500 K under controlled lighting conditions using a portable photography light box (SANOTO 16 \times 12 in. Softbox MK40, Whittier, CA) and a Canon Digital EOS T5 SLR camera. The photographs were color-corrected using the white background of the photography box as a reference prior to extraction of red, green, and blue (RGB) color channel values using a custom MATLAB script (R2013a, MathWorks, Natick, MA). The RGB components were plotted as a function of temperature to produce a calibration curve.

4.3.4 Clinical and preclinical HIFU systems

A clinical MR-HIFU system (Sonalleve V2, Profound Medical Inc., Mississauga, ON, Canada) was used for volumetric HIFU exposures (Fig. 1A). The Sonalleve V2 system delivers spatiotemporally controlled ultrasound energy, and consists of a therapy control workstation, RF generators and control electronics, and a treatment table that houses the positioning system and

Chapter 4

a 256-element phased-array ultrasound transducer (14 cm focal length). The transducer is immersed in an oil tank, sealed with a thin, plastic, acoustically transparent membrane to allow HIFU beam propagation to the target (Fig. 2).

A preclinical benchtop US-HIFU system (Therapy Imaging Probe System [TIPS], Philips Research, Cambridge, MA, USA) was also used for HIFU exposures (Fig. 1B). The TIPS system includes an 8-element annular ultrasound transducer (8 cm focal length) as well as a motion control system capable of precise spatial targeting.

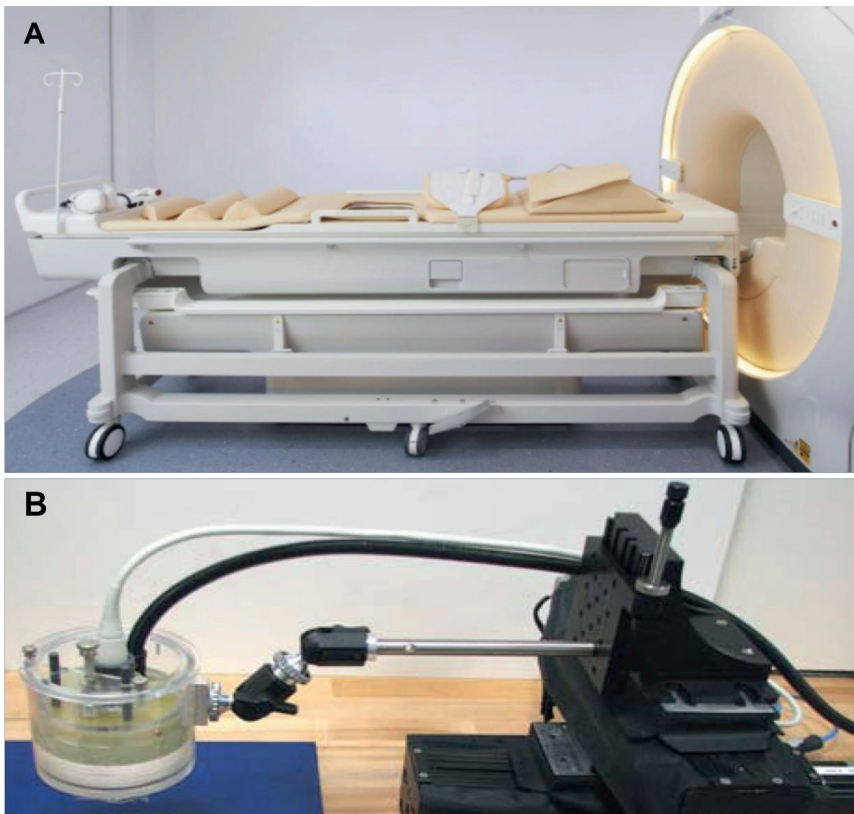


Figure 1. HIFU systems utilized in TMTCP experiments. A) The Sonalleve V2 clinical tabletop MR-HIFU system. B) The TIPS preclinical benchtop US-HIFU system.

4.3.5 Experimental setup and HIFU sonication parameters

TMTC phantoms (diameter 15 cm, height 4 cm) were prepared for HIFU sonications. These TMTCs were positioned on the clinical MR-HIFU treatment table between two pieces of acrylamide gel at room temperature (Fig. 2). Acrylamide has relatively low ultrasound attenuation (0.08 to 0.14 dB/cm at 1 MHz) and has been proposed as a coupling media for focused ultrasound therapy³⁶. Degassed water and an acrylamide layer was used for acoustic coupling between the plastic membrane and the TMTC phantom, as well as between the TMTC phantom and an acoustic absorber (Fig. 2). Nine circular regions of 12 mm in diameter were targeted, using sonication frequency of 1.2 MHz, acoustic power of 160 W, and electronic steering of the HIFU focus along concentric circle trajectories⁸. A cool-down time of 5 min was applied after each sonication, and the transducer positioning system was utilized to move between the targets. A temperature feedback algorithm with a target mean temperature of 65°C was applied, resulting in consistent sonication duration of approximately 40 s for all sonications.

Additionally, we performed pulsed boiling histotripsy (BH) sonications using acoustic power of 450 W, 10 ms long pulses, and 30 pulses per trajectory point. BH is a HIFU technique that is capable of precise mechanical fractionation of target tissue with minimal surrounding heating^{2,3,37}. Furthermore, as representative examples, HIFU sonications were performed in TMTC embedded with either a rubber blood vessel -mimic with water flow, or plastic rib mimic (VeroWhitePlus, Stratasys, Ltd., MN, USA; acoustic attenuation = 3.0 dB/cm @ 1 MHz, speed of sound = 2539 m/s)³⁸. The blood vessel -mimic was created using Penrose tubing, while the rib-mimic was created by using a CT-scan -based 3D printed section of human ribcage. The mimics were placed within the TMTC phantom mold during preparation, after which the TMTC was allowed to gel, as described earlier³⁹.

For experiments on the TIPS preclinical HIFU system, TMTCs were sandwiched between two pieces of acrylamide gel, fixed onto an acoustic absorber, and positioned underneath the TIPS transducer. This allowed for acoustic coupling by a thin layer of degassed

Chapter 4

water. Sonications were then performed using ultrasound frequency of 1.0 MHz, electric power of 30 W, and sonication durations of 60, 120, and 180 s. For each duration setting, four separate locations (2 cm apart; square pattern) were targeted, and the motion control system was utilized to move between targets.

Post-HIFU, we made multiple cuts with a surgical monofilament suture, prudently, to expose the phantom layer by layer. Once the sonicated region was exposed, we also made a transverse cut (90°), exposing the volumetric shape of the sonicated region.

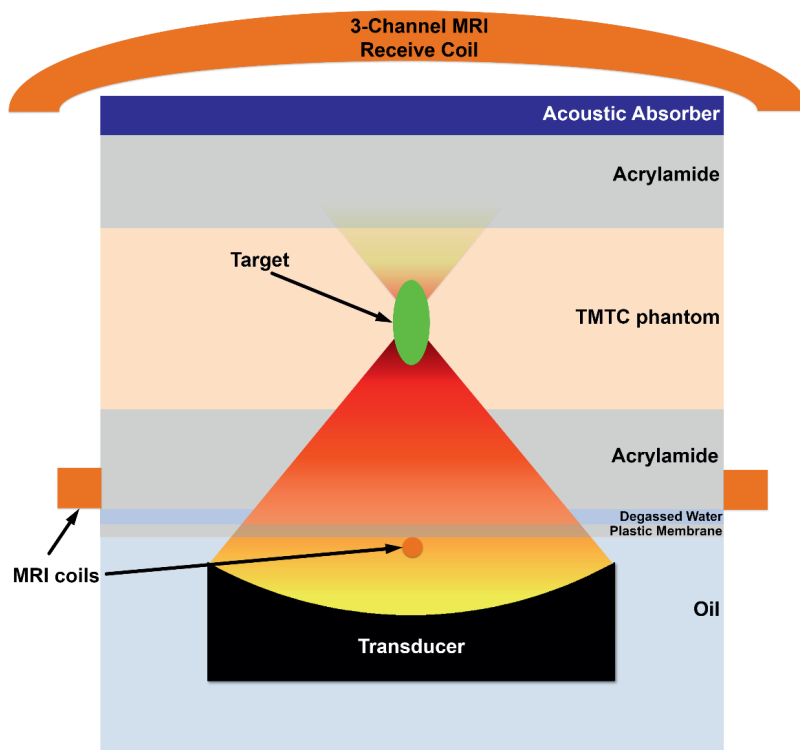


Figure 2. Schematic representation (not depicted to scale) of HIFU targeting in TMTCP using the Sonalleve V2 clinical MR-HIFU system. A similar configuration, but without the MRI coils, was used with the TIPS preclinical US-HIFU system.

Tissue-mimicking thermochromic phantom for characterization of HIFU devices and applications

4.3.6 MRI-based quantification of temperatures and T2 relaxation times

For HIFU exposures using the Sonalleve V2 clinical MR-HIFU system, a clinical 1.5T MRI scanner (Achieva, Philips, Best, Netherlands) was used for exposure planning, real-time thermometry utilizing the proton resonance frequency shift (PRFS) method ⁴⁰, and to visualize sonicated volumes using T2-weighted imaging and quantitative T2 mapping. A clinical 5-element RF receive coil was used in the experiments. The coil consists of two elements integrated into and around the acoustic window in the treatment table (below the TMTCP), and of another three elements positioned above the TMTCP (Fig. 2).

Standard T1- and T2-weighted MRI were acquired for planning the target locations in TMTCP and to visualize sonicated volumes, respectively, while multi-plane thermometry was performed during HIFU sonications using a dynamic, RF-spoiled, fast field echo-echo planar imaging (FFE- EPI) sequence. Two imaging slices were acquired; one coronal and one sagittal slice automatically positioned perpendicular and parallel to the beam axis, with the slices crossing at the center of the target region. The thermometry sequence parameters were: TR 54 ms, TE 19 ms, matrix size 144 × 144, field-of-view (FOV) 200 × 200 mm², slice thickness 7 mm, and flip angle 19.5°, resulting in voxel size of 1.4 mm × 1.4 mm × 7.0 mm, with an acquisition time of 2.5 s per dynamic frame.

Before and after TMTCP water bath heating at 65°C for 2 hours (to trigger complete and uniform color change and BSA coagulation), T2 maps of four cylindrical 200 mL phantoms were acquired to quantify pre- and post-heating MRI T2 relaxation times using a two-channel clinical RF receive coil (SENSE Flex M, Philips, Best, the Netherlands) at two different field strengths (1.5T and 3.0T, Achieva, Philips, Best, the Netherlands). T2 maps of coronal stacks consisting of 6 slices per phantom were acquired using a multi-echo 2D turbo spin echo pulse sequence with the following parameters: 16 echo times ranging from 50 to 450 ms, FOV 100 × 100 mm², in-plane acquisition resolution 2.2 × 4.0 mm², slice thickness 5 mm with a slice gap of 3.0 mm, TR 3400 ms, two signal averages, and a flip angle of 90°.

4.4 Results

4.4.1 Properties of TMTCP

Unheated TMTCP mass density, speed of sound, acoustic attenuation, acoustic impedance, thermal conductivity and diffusivity, and T2 relaxation times were measured (Table 2). Pre-heating TMTCP properties were found to be similar to those in human soft tissues such as liver, kidney, brain, and muscle^{41,42}. Post-heating T2 relaxation times were measured to be 97 ± 5 ms at 1.5T and 86 ± 5 ms at 3.0T.

In addition, TMTCP color change was assessed over a range of temperatures. The greatest color change occurred above 64°C (Fig. 3). Color changes were not detected for temperatures below 45°C, while there was a gradual change between 45 and 64°C. Additionally, Figure 4 shows color vs. temperature calibration curves derived by quantifying the red, green, and blue color channel values from TMTCP photographs. The curves are overlaid on a computer-generated color swatch, which aids visual assessment of temperature change in the TMTCP. There was minimal change in color intensity at temperatures between 30 and 45°C and between 65 and 75°C, with the green color channel displaying the greatest dynamic range between 30 and 75°C.

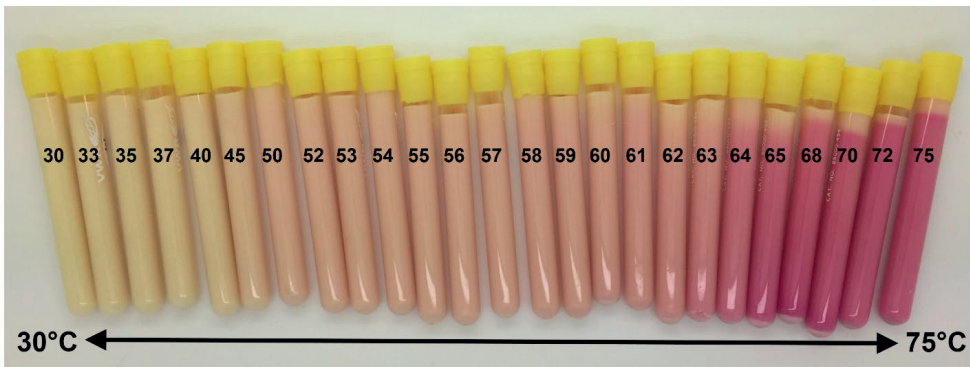


Figure 3. Color of TMTCP samples after water bath heating to temperatures between 30 and 75°C.

Color changes are visible after incubating at temperatures above 45°C.

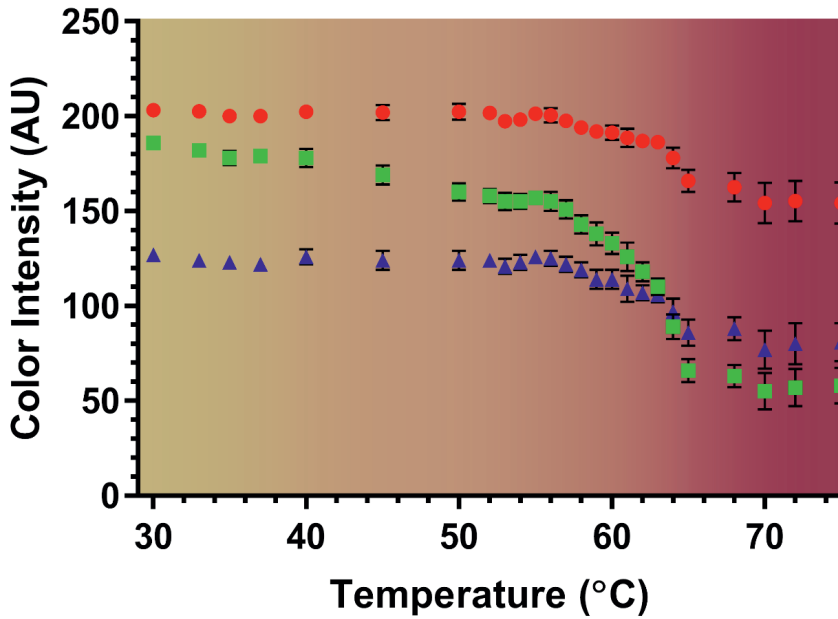


Figure 4. Color vs. temperature calibration curves derived by quantifying RGB-color intensity values of the TMTCP samples as a function of temperature between 30 and 75°C, overlaid on a computer-generated color swatch. The color swatch aids visual assessment of temperature change in the TMTCP. The circles, squares, and triangles represent red, green, and blue color channels, respectively. The error bars indicate one standard deviation of intra-phantom or analysis-based variability, not inter-phantom variability.

4.4.2 Formulation dependence of TMTCP color change

TMTCP color post-heating was examined for formulations with or without silica, BSA, or sodium chloride that provide ultrasound attenuation, MR-imageability, and electrical conductivity, respectively. Figure 5 demonstrates the effect of different phantom formulation ingredients on TMTCP color change properties. Our standard formulation (Table 1) demonstrated substantial

Chapter 4

color change at temperatures above 64°C (Fig. 5A). The formulation without sodium chloride demonstrated greater color change at temperatures above 63°C, with similar color as the standard formulation at temperatures between 55 and 70°C (Fig. 5B). Phantom formulation without silica also revealed greatest color change at 63°C (Fig. 5C). The formulation without BSA demonstrated its greatest change in color at 62°C, as well as the highest color intensity of all TMTCP formulations (Fig. 5D).



Figure 5. TMTCP color change as a function of temperature (1°C increments) and phantom formulation: A) standard formulation, B) standard formulation without sodium chloride, C) standard formulation without silica, and D) standard formulation without BSA.

Tissue-mimicking thermochromic phantom for characterization of HIFU devices and applications

4.4.3 Correspondence of TMTCP color change with MRI

Co-localization of phantom color change, temperature elevation, and T2 signal intensity changes was evaluated. Using the clinical Sonalleve V2 MR-HIFU system, we planned a pattern with nine discrete target regions – each 12 mm in diameter (Fig. 6A). Utilizing MRI-based temperature feedback control, HIFU sonications resulted in mean temperatures above 65°C at the targeted regions (Fig. 6B). Post-HIFU, nine hypointense regions approximately 12 mm in diameter were visible on T2-weighted MRI, corresponding to locations of TMTCP color changes (Fig. 6C & D) with high spatial precision relative to the sonication plan. Ablative temperatures were reflected in the TMTCP color, with nine regions displaying a uniform change to magenta (Fig. 6D). Ovoid regions of color change approximately 30 mm in length were visible in the phantom along the ultrasound-axis (Fig. 6E).

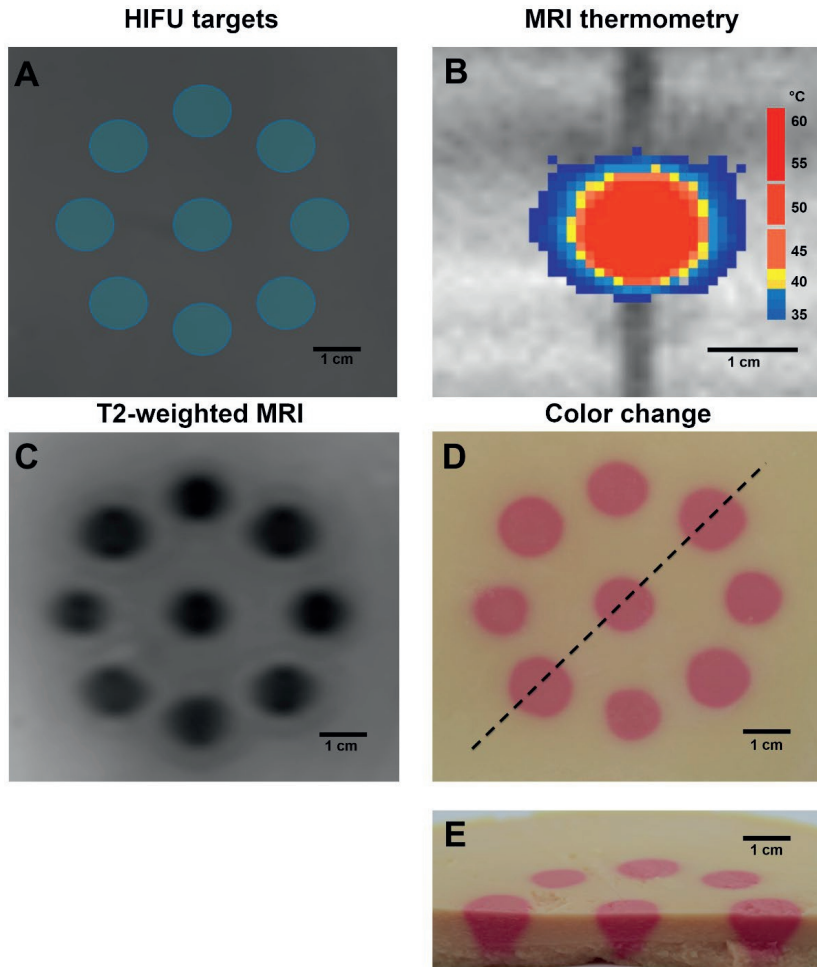


Figure 6. **A)** HIFU target planning within a TMTCP performed on T1-weighted MRI. **B)** Real-time MRI thermometry during HIFU sonication. **C)** Hypointense regions (due to BSA coagulation) on T2-weighted MRI. **D)** Photograph of TMTCP cross-section perpendicular to the HIFU beam path, showing permanent color changes with high spatial precision relative to the plan. The dashed line represents the cut to expose volumetric nature of color change. **E)** Photograph of a bisected TMTCP showing color changes perpendicular to and along the HIFU beam path.

4.4.4 TMTCP assessment on a preclinical US-HIFU system

TMTCP extensibility to other devices was assessed by performing HIFU sonications on a preclinical ultrasound-guided HIFU system. Four spatial locations in each TMTCP were targeted, resulting in consistent color change at the target locations (Fig. 7). Sonications of 60 s produced small regions of color change at low color intensity, while 180 s sonications displayed the largest spatial dimensions and greatest intensity of color. Ovoid regions of lower T2 relaxation times, which enlarged with increasing sonication duration, were observed in 3.0T MRI T2 maps (Fig. 7).

Finally, T2 relaxation time change and color change profiles were computationally derived based on T2 maps and TMTCP photographs. Representative maps for 120 s sonications are shown in Figure 8A and 8B for T2 and color, respectively. Temperature contours derived from the color map and temperature vs. color calibration (Fig. 4) are also shown in Figure 8B. Maximum T2 change from baseline was approximately 55 ms at the center of each target region, gradually decreasing at locations further away from the targets (Fig. 8C). Correspondingly, the green color intensity change was approximately 100 units at the center of each target, gradually reducing to zero further away from the targets (Fig. 8D). The T2 transition from the target center to the periphery was more gradual compared to the color intensity transition.

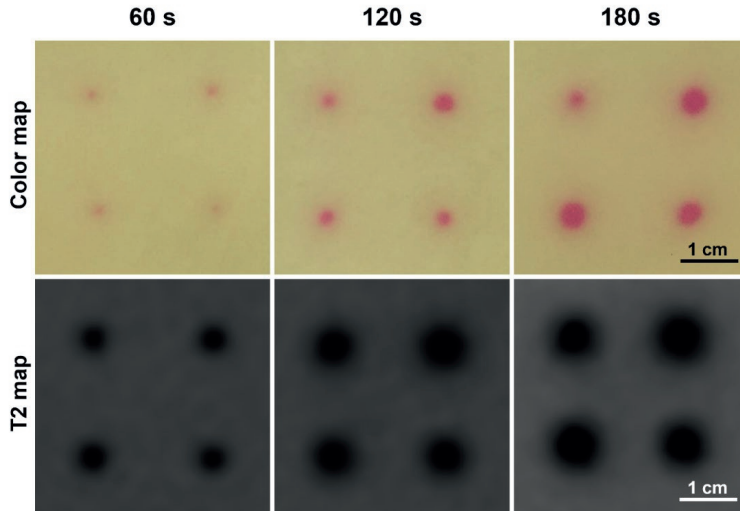


Figure 7. Representative TMTCP cross-section photographs and MRI T2 maps perpendicular to HIFU beam for 60 s, 120 s, and 180 s sonications on the TIPS US-HIFU system.

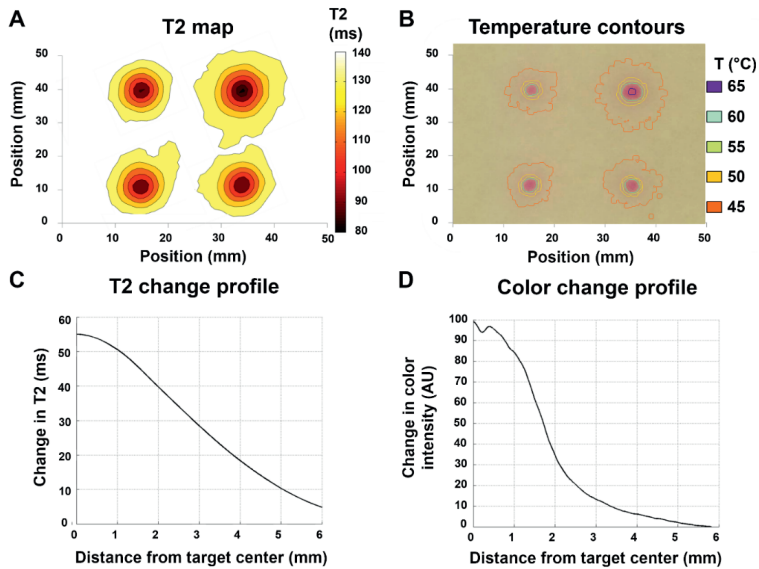


Figure 8 A&B) Computationally derived T2 and temperature contours based on MRI T2 maps and TMTCP color maps, respectively, following 120 s sonications on the TIPS preclinical HIFU system. **C&D)**

Tissue-mimicking thermochromic phantom for characterization of HIFU devices and applications

Representative examples of T2 and color change radial line profiles centered on the target. Profiles correspond to the upper left-hand-corner sonication location in A&B.

4.4.5 TMTCP HIFU applications

As an example of HIFU heating characterization, we performed sonications in TMTCP with the intent of producing both sparse and contiguous heating patterns (Fig. 9A & B) on the TIPS preclinical US-HIFU system. In both cases, we found locations with spatially precise color change and a sharp transition zone with high spatial accuracy relative to the plan, demonstrating the TMTCP utility in optimizing HIFU parameters and assessing targeting accuracy.

As an additional example, we evaluated the TMTCP applicability in assessing BH sonications using the Sonalleve V2 clinical HIFU system. We sonicated an 8-point circular pattern using HIFU parameters that resulted in high acoustic pressures *in situ*, and found localized mechanical fractionation and color changes limited to the sonication foci, with minimal extra-focal color change, consistent with BH sonications (Fig. 9C). This suggests that TMTCP may be applied in BH parameter optimization, and in evaluation of BH mechanical fractionation and heating.

TMTCP was also utilized to visualize HIFU side lobes and near-field heating (Fig. 9D). While the main color change region corresponded to focal energy deposition, color changes around the focal region and along the beam-axis were also observed, suggesting the role of side lobes in off-target heating, possibly due to non-random transducer element placement.

Finally, we showcased simplified HIFU ablation examples in close proximity to a large, high-flow vessel and of a liver segment situated under the rib cage by performing HIFU sonications in presence of TMTCP-embedded rubber vessel-mimic or plastic rib-mimic (Fig. 9E). No color change was apparent immediately adjacent to the vessel-mimic, indicating a heat sink effect. On the other hand, substantial color changes were observed next to the rib-mimic, demonstrating that its acoustic properties, which deviate from those of TMTCP, result in extensive off-target heating (Fig. 9F).

Overall, these results and observations highlight TMTCP applicability in characterization of different HIFU devices, applications, and sonication parameters.

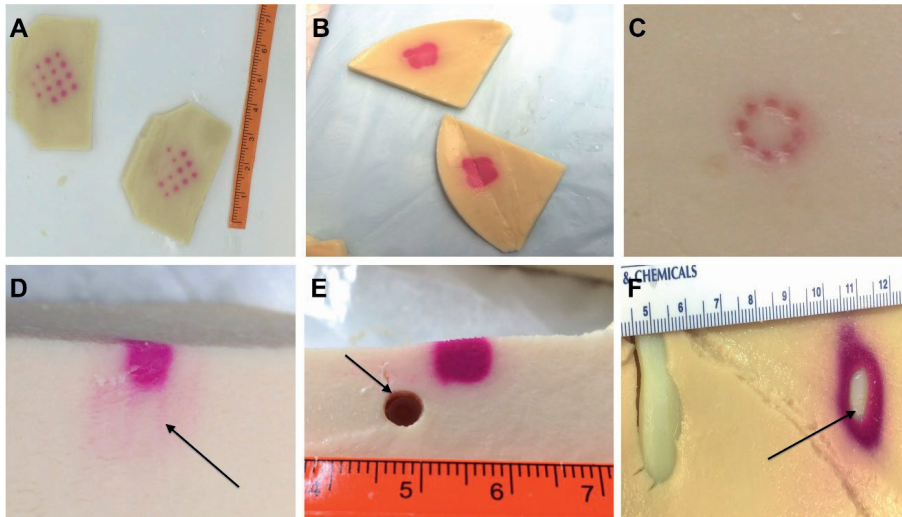


Figure 9. Example applications for TMTCP in HIFU use: **A&B)** Assessment of targeting accuracy, sonication grid patterns, sparsity or contiguity of the heated region, and achieved temperatures; **C)** Assessment of volumetric HIFU histotripsy and the resulting heating; **D)** Assessment of side lobes (arrow) and near-field heating; **E)** Assessment of heating patterns in close proximity to a vessel mimic (arrow), i.e., a heat sink; and **F)** Assessment of heating and heat diffusion in the presence of TMTCP-embedded rib-mimics (arrow).

4.5 Discussion

The success of thermoablative therapies depends on precise spatial targeting and controlled temperature elevation within target tissues. In particular, HIFU thermal ablation has required MRI thermometry for sonication parameter optimization, assessment of targeting accuracy, and assurance of appropriate temperature elevation for coagulative necrosis^{8,43-45}. Temperature probes proximal to the HIFU focal zone have been used for ultrasound-guided HIFU applications. However, given the 3D nature of the focal acoustic pressure field and frequent utilization of volumetric heating concepts such as electronic steering of the focal point, the

Tissue-mimicking thermochromic phantom for characterization of HIFU devices and applications accuracy of volumetric temperature estimates depends on the number of probes and their location²⁴.

We have previously developed a TMTCP comparable to liver tissue for characterization of radiofrequency thermal ablation²⁸. Herein, a HIFU-compatible TMTCP was developed, its color assessed as a function of temperature, and its performance characterized on two different HIFU systems. Post-HIFU TMTCP color changes were correlated with MRI thermometry and T2 maps, demonstrating the applicability of TMTCP in MR-HIFU use.

Currently, most available TMPs cannot be used to accurately assess the spatial location and volume of the heated region post-HIFU. We witnessed an abrupt color change when TMTCP temperatures surpassed 64°C. This observation is particularly valuable in optimizing HIFU sonication parameters for tissue thermal ablation (55-65°C)⁴⁶. In addition, the TMTCP provides a permanent and stable change in color, allowing immediate or delayed assessment of HIFU-generated heated volumes (Figs. 6E & 9D). RGB color intensities were quantified from photographs of heated TMTCP samples (Fig. 4). Based on this color vs. temperature calibration, photos of TMTCP can be used for automated or semi-automated computational temperature estimates (Fig. 8B) to, e.g., validate MRI or US-based thermometry techniques.

The MRI compatibility of TMTCP is particularly valuable since a considerable number of HIFU treatments are performed under MRI guidance^{44,46}. TMTCP formulation with BSA provides permanent T2 relaxation time changes upon HIFU heating, allowing post-HIFU MRI-based verification of ablative temperatures. TMTCP pre-heating T2 relaxation times were comparable to human kidney and brain tissues. Post-heating, 57% and 43% T2 decrease was observed at 1.5T and 3.0T, respectively, suggesting a wide dynamic range in T2 maps and T2-weighted MRI of the TMTCP. Accordingly, we observed BSA denaturation and corresponding T2 changes at all targeted locations that correlated spatially with regions of color change. This suggests that both MRI T2 maps and TMTCP color maps can be used to validate targeting accuracy and assess heating patterns, independent of the utilized MR-HIFU or US-HIFU device. Figure 8 depicts T2

Chapter 4

and color change as a function of distance from the focus, and suggests that BSA coagulation begins at a lower temperature, and occurs more gradually than color change. However, the BSA coagulation threshold and degree of coagulation (T2 shortening) as a function of temperature or thermal dose may need to be characterized in more detail to allow for more accurate volumetric comparison and correlation of T2 maps and color maps.

HIFU sonications were also performed on a preclinical, MRI-incompatible, US-guided HIFU system without real-time thermometry capabilities to verify TMTCP applicability to other devices. We observed no appreciable TMTCP echogenicity changes on b-mode ultrasound post-heating when compared to pre-heating. For experiments in which echogenicity changes are desirable, it may be of interest to further adjust and optimize the TMTCP formulation to provide a post-heating echogenicity change. The TMTCP, however, provides quantitative information on temperatures, volumetric heating patterns, and targeting accuracy via color change. This allows for cost-effective device calibration and parameter optimization for various clinical HIFU applications without the need for real-time MRI-based thermometry. Example applications may include HIFU augmentation of immunotherapy, where generation of sparse heating patterns may yield better outcomes⁴⁷. If specific temperature immune-effects are better characterized, perhaps the TMTCP may be used to optimize HIFU-assisted immunotherapies. Similarly, HIFU ablation in close proximity to critical anatomical structures may carry risk, as off-target heating may not be predictable and should be avoided²¹. As showcased in this work, patient-specific, 3D-printed anatomic structure mimics embedded within a TMTCP might facilitate simulation or planning for specific high risk HIFU applications.

TMTCP temperature vs. color assessment for modified phantom formulations was performed to provide additional flexibility for users that do not have access to an MRI scanner or do not plan to use TMTCP for radiofrequency ablation-related work. For example, by preparing TMTCP without BSA or NaCl that provide MR-imageability and electrical conductivity, respectively, the phantom manufacturing can be simplified and made more economical.

Tissue-mimicking thermochromic phantom for characterization of HIFU devices and applications

Limitations of TMTCP should be considered. First, while the TMTCP provides a gradual color change at temperatures between 45 and 63°C, substantial color changes only occur at temperatures above 64°C. Although beneficial in HIFU ablation assessment, the TMTCP formulation may need to be adjusted for better evaluation of mild hyperthermia and sub-ablative temperatures. Alternatively, the use of other thermochromic inks with different color and color-change properties could be considered. Second, as the TMTCP color change is permanent, TMTCPs are essentially for singular use. However, thin exchangeable and disposable TMTCP slabs can be sandwiched between reusable, anthropomorphic materials in order to reduce costs or preparation time, as demonstrated in this study. Such phantoms with ablate-able and disposable modules fitting into anthropomorphic phantoms may have roles for training and simulation, especially for MRI-guided HIFU, or US-guided RF or microwave ablation. Similarly, small TMTCP can be embedded in a larger, reusable, non-thermochromic phantom. Third, as previously described, the TMTCP only reports absolute temperatures and not the cumulative thermal dose (i.e., time-temperature relationship) that is considered a better descriptor of tissue coagulative necrosis²⁸. To fully assess HIFU parameters and protocols applied in the clinic, the TMTCP ambient temperature should be maintained at 37°C during experiments. Finally, although the TMTCP acoustic attenuation was measured in this study, it may additionally be valuable to measure the relative contribution of absorption and scattering to the degree of power deposition (i.e., temperature elevation). This assessment could inform further optimization of the phantom formulation and its tissue-mimicking properties. Similarly, the phantom formulation may benefit from optimization and characterization specifically for non-thermal HIFU therapy approaches (e.g., histotripsy) by adjusting the formulation to closely match tissue properties such as elasticity and pressure threshold for cavitation.

4.6 Conclusion

A novel MR-imageable and HIFU compatible TMTCP that permanently changes color upon heating was developed. The TMTCP facilitates characterization of HIFU devices, sonication parameters, and heating protocols without the need for real-time MRI or thermocouple-based thermometry. The HIFU-optimized TMTCP can provide quantitative information on absolute temperatures, ablation volume geometry, temperature uniformity, and spatial targeting accuracy, based on TMTCP color and/or T2 change. Consequently, the TMTCP can be used to evaluate HIFU device- and sonication parameter-specific heating characteristics in a controlled, predictable, and spatially uniform environment through simple visual or computational methods. Although yet to be demonstrated, such methodologies may have important training and treatment planning implications as well.

4.7 References

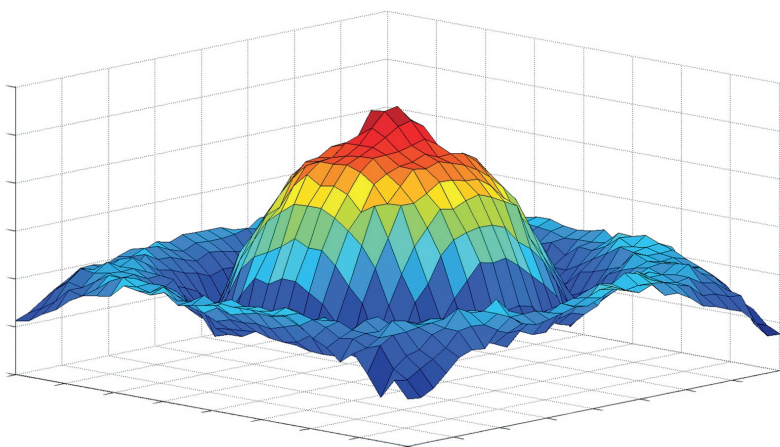
- 1 Partanen, A. *et al.* Mild hyperthermia with magnetic resonance-guided high-intensity focused ultrasound for applications in drug delivery. *International journal of hyperthermia* **28**, 320-336 (2012).
- 2 Eranki, A. *et al.* Boiling histotripsy lesion characterization on a clinical magnetic resonance imaging-guided high intensity focused ultrasound system. *PLoS one* **12**, e0173867 (2017).
- 3 Eranki, A. *et al.* Mechanical fractionation of tissues using microsecond-long HIFU pulses on a clinical MR-HIFU system. *International Journal of Hyperthermia*, 1-12 (2018).
- 4 Illing, R. *et al.* The safety and feasibility of extracorporeal high-intensity focused ultrasound (HIFU) for the treatment of liver and kidney tumours in a Western population. *British journal of cancer* **93**, 890-895 (2005).
- 5 F. Wu, L. Z., and W. R. Chen. Host antitumour immune responses to HIFU ablation. *International Journal of Hyperthermia* **23**, 165-171 (2007).
- 6 Huisman, M. *et al.* Feasibility of volumetric MRI-guided high intensity focused ultrasound (MR-HIFU) for painful bone metastases. *J Ther Ultrasound* **2**, b51 (2014).
- 7 Kim, Y.-s. *et al.* Volumetric MR-HIFU ablation of uterine fibroids: role of treatment cell size in the improvement of energy efficiency. *European journal of radiology* **81**, 3652-3659 (2012).
- 8 Köhler, M. O. *et al.* Volumetric HIFU ablation under 3D guidance of rapid MRI thermometry. *Medical physics* **36**, 3521-3535 (2009).
- 9 Mikhail, A. S., Partanen, A., Yarmolenko, P., Venkatesan, A. M. & Wood, B. J. Magnetic resonance-guided drug delivery. *Magnetic Resonance Imaging Clinics* **23**, 643-655 (2015).
- 10 Kim, J., Kim, M. & Park, Y. Development of an agar phantom adaptable for visualization of thermal distribution caused by focused ultrasound. 1372-1375 (2011).
- 11 Lai, C.-Y., Kruse, D., Seo, J. W., Kheirloom, A. & Ferrara, K. W. A phantom for visualization of three-dimensional drug release by ultrasound-induced mild hyperthermia. *Medical Physics* **40**, 083301 (2013).
- 12 Pichardo, S., Kivinen, J., Melodelima, D. & Curiel, L. Suitability of a tumour-mimicking material for the evaluation of high-intensity focused ultrasound ablation under magnetic resonance guidance. *Phys Med Biol* **58**, 2163-2183 (2013).
- 13 Dunmire, B., Kuczewicz, J. C., Mitchell, S. B., Crum, L. A. & Sekins, K. M. Characterizing an Agar/Gelatin phantom for image guided dosing and feedback control of high-intensity focused ultrasound. *Ultrasound in Medicine and Biology* **39**, 300-311 (2013).
- 14 Farrer, A. I. *et al.* Characterization and evaluation of tissue-mimicking gelatin phantoms for use with MRgFUS. *Journal of Therapeutic Ultrasound* **3** (2015).
- 15 Choi, M. J., Guntur, S. R., Lee, K. I., Paeng, D. G. & Coleman, A. A tissue mimicking polyacrylamide hydrogel phantom for visualizing thermal lesions generated by high intensity focused ultrasound. *Ultrasound in medicine & biology* **39**, 439-448 (2013).
- 16 Madsen, E. L., Frank, G. R. & Dong, F. Liquid or solid ultrasonically tissue-mimicking materials with very low scatter. *Ultrasound Med Biol* **24**, 535-542 (1998).
- 17 McDonald, M., Lochhead, S., Chopra, R. & Bronskill, M. J. Multi-modality tissue-mimicking phantom for thermal therapy. *Phys Med Biol* **49**, 2767-2778 (2004).
- 18 Partanen, A., Mougnot, C. & Vaara, T. Feasibility of Agar-Silica Phantoms in Quality Assurance of MRgHIFU. *AIP Conference Proceedings* **1113**, 296-300 (2009).
- 19 Dabbagh, A., Abdullah, B. J., Ramasindarum, C. & Abu Kasim, N. H. Tissue-mimicking gel phantoms for thermal therapy studies. *Ultrason Imaging* **36**, 291-316 (2014).
- 20 Dasgupta, S., Banerjee, R. K., Hariharan, P. & Myers, M. R. Beam localization in HIFU temperature measurements using thermocouples, with application to cooling by large blood vessels. *Ultrasonics* **51**, 171-180 (2011).
- 21 Civale, J., Clarke, R., Rivens, I. & Ter Haar, G. The use of a segmented transducer for rib sparing in HIFU treatments. *Ultrasound in medicine & biology* **32**, 1753-1761 (2006).
- 22 Rieke, V. & Butts Pauly, K. MR thermometry. *Journal of Magnetic Resonance Imaging* **27**, 376-390 (2008).
- 23 Horder, M. M., Barnett, S. B., Vella, G. J., Edwards, M. J. & Wood, A. K. In vivo heating of the guinea-pig fetal brain by pulsed ultrasound and estimates of thermal index. *Ultrasound in medicine & biology* **24**, 1467-1474 (1998).

Chapter 4

- 24 Hynynen, K. The threshold for thermally significant cavitation in dog's thigh muscle in vivo. *Ultrasound in Medicine and Biology* **17**, 157-169 (1991).
- 25 Bouchard, L. S. & Bronskill, M. J. Magnetic resonance imaging of thermal coagulation effects in a phantom for calibrating thermal therapy devices. *Medical Physics* **27**, 1141-1145 (2000).
- 26 Brodin, N. P. *et al.* A simple method for determining the coagulation threshold temperature of transparent tissue-mimicking thermal therapy gel phantoms: Validated by magnetic resonance imaging thermometry. *Medical Physics* **43**, 1167-1174 (2016).
- 27 Negussie, A. H. *et al.* Thermochromic tissue-mimicking phantom for optimization of thermal tumor ablation. *Int J Hyperthermia* **32**, 239-243 (2016).
- 28 Mikhail, A. S. *et al.* Evaluation of a tissue-mimicking thermochromic phantom for radiofrequency ablation. *Medical Physics* **43**, 4304-4311 (2016).
- 29 Smith, C., Sabatino, D. & Praisner, T. Temperature sensing with thermochromic liquid crystals. *Experiments in fluids* **30**, 190-201 (2001).
- 30 Qureshi, F. *et al.* Thermochromic phantom for therapeutic ultrasound daily quality assurance. *Journal of Therapeutic Ultrasound* **3**, P72 (2015).
- 31 Dabbagh, A., Abdullah, B. J. J., Abu Kasim, N. H. & Ramasindarum, C. Reusable heat-sensitive phantom for precise estimation of thermal profile in hyperthermia application. *International journal of hyperthermia* **30**, 66-74 (2014).
- 32 Gammell, P. M., Maruvada, S. & Harris, G. R. An ultrasonic time-delay spectrometry system employing digital processing. *Ieee Transactions on Ultrasonics Ferroelectrics and Frequency Control* **54**, 1036-1044 (2007).
- 33 Madsen, E. L. *et al.* Interlaboratory comparison of ultrasonic backscatter, attenuation, and speed measurements. *Journal of Ultrasound in Medicine* **18**, 615-631 (1999).
- 34 Marczak, W. Water as a standard in the measurements of speed of sound in liquids. *Journal of the Acoustical Society of America* **102**, 2776-2779, doi:10.1121/1.420332 (1997).
- 35 Christensen, D. A. *Ultrasonic Bioinstrumentation*. (John Wiley and Sons, 1988).
- 36 Prokop, A. F. *et al.* Polyacrylamide gel as an acoustic coupling medium for focused ultrasound therapy. *Ultrasound in medicine & biology* **29**, 1351-1358 (2003).
- 37 Canney, M. S., Khokhlova, V. A., Bessonova, O. V., Bailey, M. R. & Crum, L. A. Shock-induced heating and millisecond boiling in gels and tissue due to high intensity focused ultrasound. *Ultrasound in medicine & biology* **36**, 250-267 (2010).
- 38 Alles, E. J., Nikitichev, D. & Desjardins, A. E. in *2015 IEEE International Ultrasonics Symposium (IUS)*. 1-4 (IEEE).
- 39 Farr, N. *et al.* in *5th International Symposium on Focused Ultrasound* (2016).
- 40 Quesson, B., de Zwart, J. A. & Moonen, C. T. Magnetic resonance temperature imaging for guidance of thermotherapy. *Journal of Magnetic Resonance Imaging* **12**, 525-533 (2000).
- 41 Stanisz, G. J. *et al.* T1, T2 relaxation and magnetization transfer in tissue at 3T. *Magnetic Resonance in Medicine: An Official Journal of the International Society for Magnetic Resonance in Medicine* **54**, 507-512 (2005).
- 42 Duck, F. A. *Physical Properties of Tissue: A Comprehensive Reference Book*. (Academic Press Limited, 1990).
- 43 Quesson, B. *et al.* A method for MRI guidance of intercostal high intensity focused ultrasound ablation in the liver. *Medical physics* **37**, 2533-2540 (2010).
- 44 Sharma, K. V. *et al.* Comparison of noninvasive high-intensity focused ultrasound with radiofrequency ablation of osteoid osteoma. *The Journal of pediatrics* **190**, 222-228. e221 (2017).
- 45 Yarmolenko, P. S. *et al.* Technical aspects of osteoid osteoma ablation in children using MR-guided high intensity focussed ultrasound. *International Journal of Hyperthermia* **34**, 49-58 (2018).
- 46 Hesley, G. K., Gorny, K. R., Henrichsen, T. L., Woodrum, D. A. & Brown, D. L. A clinical review of focused ultrasound ablation with magnetic resonance guidance: an option for treating uterine fibroids. *Ultrasound quarterly* **24**, 131-139 (2008).
- 47 Liu, F. *et al.* Boosting high-intensity focused ultrasound-induced anti-tumor immunity using a sparse-scan strategy that can more effectively promote dendritic cell maturation. *Journal of translational medicine* **8**, 7 (2010).

Chapter 5

Mechanical HIFU-triggered Immune Sensitization of Refractory Murine Neuroblastoma for Checkpoint Inhibitor Therapy



This chapter is based on:

Eranki, Avinash, et al. "Mechanical HIFU-triggered Immune Sensitization of Refractory Murine Neuroblastoma for Checkpoint Inhibitor Therapy" *Clinical Cancer Research* (2019, under review).

5.1 Abstract

Immunotherapy promises unprecedented benefits to cancer patients. However, the majority of cancer types, including high-risk neuroblastoma remain immunologically unresponsive. High intensity focused ultrasound (HIFU) is a non-invasive technique that can mechanically fractionate tumors, transforming immunologically “cold” tumors into responsive “hot” tumors. We treated <2% of tumor volume in previously unresponsive, large, refractory murine neuroblastoma tumors with mechanical HIFU, and assessed systemic immune response using flow-cytometry, ELISA, and gene sequencing. In addition, we combined this treatment with α CTLA-4 and α PD-L1 to study its effect on the immune response and long-term survival. Combining HIFU with α CTLA-4 and α PD-L1 significantly enhances anti-tumor response, improving survival from 0 to 62.5%. HIFU alone causes upregulation of splenic and lymph node NK cells and circulating IL-2, IFN- γ , and DAMPs, whereas immune regulators like CD4+Foxp3+, IL-10, and VEGF-A are significantly reduced. HIFU combined with checkpoint inhibitors induced significant increases in intratumoral CD4+, CD8 α +, and CD8 α +CD11c+ cells, CD11c+ in regional lymph nodes, and decrease in circulating IL-10 compared to untreated group. We also report significant abscopal effect following unilateral treatment of mice with large, established bilateral tumors using HIFU and checkpoint inhibitors compared to tumors treated with HIFU or checkpoint inhibitors alone (61.1% survival, $p < 0.0001$). This combination treatment significantly also induces CD4+CD44+hiCD62L+low and, CD8 α +CD44+hiCD62L+low population and are adoptively transferable imparting immunity, slowing subsequent de novo tumor engraftment. Mechanical fractionation of tumors using HIFU can effectively induce immune sensitization in a previously unresponsive murine neuroblastoma model, and promises a novel yet efficacious immuno-adjuvant modality to overcome therapeutic resistance.

5.2 Introduction

Despite the unprecedented potential of cancer immunotherapy, many patients with cancer do not respond to immunotherapy^{1,2}. Even among those that initially respond, many relapse after some period due to inadequate T-cell recognition resulting from loss of tumor antigen presentation by tumor cells^{3,4}. Both local and systemic strategies are required to mitigate therapeutic resistance to immunotherapy and transform immunologically “cold” tumors into responsive “hot” tumors.

Neuroblastoma is the third most common childhood cancer and arises from the developing sympathetic nerve ganglia in the abdomen, chest or, neck^{5,6}. Survival for pediatric patients with high-risk neuroblastoma has improved in recent years with the addition of multi-modal therapy including high dose chemotherapy, radiation, autologous stem-cell transplantation, and immunotherapy⁷. The costs of therapy associated with acute and late side-effects are high and over 50% of patients still do not survive despite intensive therapy⁷. Neuroblastoma cells evade the innate and adaptive immune system by downregulation of human leucocyte antigen (HLA) - class I & II^{8,9}, and are likely to be ignored by the host T-cell compartment^{8,10,11}. Various efforts to facilitate immunotherapy-based strategies including engineered T-cells specific to disialoganglioside (GD2), monoclonal antibodies directly targeting GD2, $\gamma\delta$ T-cells, and vaccine therapies have changed neuroblastoma treatment perspective¹²⁻¹⁵. Immune checkpoint inhibitor therapy is a recent advance in cancer therapy for several adult tumors, but similar responses have not been appreciated in pediatric solid tumor malignancies^{1,16,17}. The lack of therapy effectiveness in pediatric neuroblastoma is due to upregulation of TGF- β and IL-10, and downregulation of ligands that activate receptors expressed on NK and T-cells^{8,18}. The natural inhibition of hemopoietic stem-cell differentiation, generation of dendritic cells (DCs), T-cell proliferation, and the phenotype of the cellular and humoral immune response to neuroblastoma tumor cells is strikingly similar in human and murine (Neuro2a) hosts^{19,20}.

Chapter 5

Sensitizing and changing the tumor microenvironment is shown to improve the efficacy of checkpoint inhibitor therapy, resulting in systemic tumor regression ²¹. Minimally invasive treatments such as radiofrequency (RFA) and, cryo-ablation have been used to perform tumor ablation in the clinic that result in an inflammatory response ²²⁻²⁴. High intensity focused ultrasound (HIFU) is a completely noninvasive ablation therapy that is used in the clinic to thermally ablate solid tumors ^{25,26}. Thermal ablation using RFA and HIFU, however, could be unfavorable immunologically due to heat-associated tumor fixation, resulting in poor tumor permeability to immune cells and antigen release deficiency ^{27,28}. In addition to thermal ablation, HIFU can also be used to mechanically fractionate tumors, with minimal thermal effects, referred to as histotripsy ²⁹⁻³¹, which may improve anti-tumor immune sensitivity. Together with our collaborators, we have previously characterized this modality of HIFU, boiling histotripsy (BH, which will hereon be referred to as 'HIFU'), a technique capable of mechanically fractionating tumors with high spatial precision using a clinical HIFU system for ablation ³²⁻³⁴. HIFU-mediated mechanical tumor fractionation may cause immunogenic cell death, and create an *in situ* tumor debris depot within the treated zone, increasing inflammation and, potentially leading to immune sensitization ^{28,35}, which is unlikely to occur in HIFU ablation due to lack of tumor permeability ²⁷.

Herein, we report the role for HIFU in inducing significant immune response in a previously refractory, large subcutaneous murine neuroblastoma tumor model (Neuro2a)³⁶. We report that (1) partial mechanical fractionation of tumor using HIFU in combination with checkpoint inhibitors (α CTLA-4 + α PD-L1) significantly prolongs survival in a previously refractory unilateral and bilateral neuroblastoma tumor model; (2) HIFU induces a systemic immune activation of DCs, tumor infiltrating T-cells, proinflammatory cytokine changes, and damage-associated molecular patterns (DAMPs) changes, while downregulating regulatory T-cells, IL-10, TGF- β , and VEGF-A; and (3) HIFU-based tumor mechanical fractionation elicits systemic effector memory that is adoptively transferable.

5.3 Methods & Materials

5.3.1 Mouse Neuroblastoma Cell Culture & Checkpoint Inhibitor Antibodies

The murine neuroblastoma cell line Neuro2a is derived from an aggressive and metastatic sub-clone of the C1300 neuroblastoma cell line that was cultured from a spontaneous tumor in the spinal cord of A/J mice (ATCC, Manassas, VA). Neuro2a cells were maintained in Dulbecco's Modified Essential Medium (DMEM) supplemented with 1% penicillin-streptomycin (Invitrogen, Carlsbad, CA) and 10% fetal bovine serum (Gemini Bioproducts, Sacramento, CA). Cells were grown at 37°C under 5% CO₂. Anti-mouse checkpoint inhibitors αCTLA-4 (clone 9D9) and αPD-L1 (clone 10F.9G2) were obtained from commercially available source (BioXCell, West Lebanon, NH).

5.3.2 Study Design

This study was designed to evaluate the role and efficacy of HIFU-based tumor fractionation on treatment of murine neuroblastoma tumors. Experiments were performed on a protocol (IRB# 30499) approved by institutional animal care and use committee (IACUC) at Children's National Medical Center, Washington, DC. A total of 150 A/J mice with subcutaneous tumors were used in this study (105 unilateral, and 45 bilateral). Mice were assigned randomly to six treatment groups: HIFU + αCTLA-4 + αPD-L1 (N = 16), a combination of αCTLA-4 + αPD-L1 (N = 10), HIFU only (N = 10), combinations of HIFU with only either αCTLA-4 or αPD-L1 (HIFU + αCTLA-4, N = 10); (HIFU + αPD-L1, N = 10), and untreated (N = 10). Mice in these groups had large, established unilateral neuroblastoma tumors. In addition, we evaluated HIFU + αCTLA-4 + αPD-L1 (N = 18) in mice with established and large bilateral tumors. Mice in all groups were subcutaneously injected with 1×10^6 neuroblastoma (Neuro2a) cells in the flank, and were randomized once the tumors reached a volume of 1200-1750 mm³. This model was desired over an orthotopic model to reduce variability and to avoid introduction of technical targeting challenges introduced by alternate models. In this and other murine models, >40% mortality by day 100 was

Chapter 5

previously demonstrated for starting tumor volumes less than 300 mm³ ^{15,28,37,38}. Combination of α CTLA-4 + α PD-L1 (100 μ g/antibody/mouse/time-point) was administered intraperitoneally on ~ days 1, 4 and, 7 after HIFU (Figure 1A). Mice were euthanized if tumor volumes exceeded 4000 mm³. Mice surviving HIFU alone or combinational treatment were re-challenged with 2x initial tumor burden (2×10^6 cells) >300 days after the first tumor challenge, to test long-term immune memory effect. T-cells were isolated from spleens of surviving mice, and $\sim 8 \times 10^6$ cells were adoptively transferred into naïve mice with de novo established (~ 600 -900 mm³ tumor volume) neuroblastoma tumors. Animal caretakers, as well as investigators who analyzed data were blinded to the mice groups.

5.3.3 Ultrasound-guided HIFU Tumor Fractionation

The HIFU system consists of a transducer that is capable of producing equivalent acoustic pressures to a clinical HIFU transducer (Sonalleve[®] V2 MR-HIFU system, Profound Medical Inc., Mississauga, ON, Canada) ³². The focal size of our HIFU transducer was 1.5×1.5×7 mm at -6dB level; with a transmit frequency of 1.5 MHz, focal length of 56 mm, and transducer aperture diameter of 75 mm. A commercially available amplifier (1240L, E&I, Rochester, NY) was used to power the HIFU transducer. The HIFU transducer produced a peak positive pressure of 85 MPa, and peak negative pressure of 14 MPa (shock amplitude of 80 MPa), measured in water using a fiber optic probe hydrophone (Rp Acoustics, Leutenbach, Germany). A 13.33 ms-long pulse at 1 Hz pulse repetition frequency, as previously described, was used for *in vivo* HIFU sonications ³². The HIFU focus was sequentially moved across three adjacent, non-overlapping foci using a computer controlled 3-axis linear-stage (Velmex, Bloomfield, NY) covering ~ 2% tumor volume (acoustically equivalent). The pulsing protocol was applied for 15 seconds/focus (Figure 1B). Mice were anesthetized using a ketamine-xylazine cocktail (100 mg/kg ketamine and 10 mg/kg xylazine), attached to a custom-built holder, and positioned in the water tank to align the HIFU focus within the tumor. The linear stages were connected to stepper motors (Maxon motors, Fall

Mechanical HIFU-triggered Immune Sensitization of Refractory Murine Neuroblastoma

River, MA) and remotely controlled (Galil motion controller, Rocklin, CA). A diagnostic ultrasound transducer (S12-4, Philips CX50, Philips, Cambridge, MA) was placed co-axially with the HIFU transducer for real-time b-mode image guidance to target the tumor along the axial plane (Figure 1B). This setup enabled a robust and repeatable platform to treat murine tumors. Immediately after HIFU, mice were administered buprenorphine (0.3 mg/ml of buprenorphine diluted to 1:10 with PBS) subcutaneously. Additional doses of buprenorphine were administered at 12, 24, and 48-hours post HIFU treatment, to alleviate any pain caused by tumor fractionation.

5.3.4 Statistical Analysis

All statistical analyses were performed using GraphPad Prism software (GraphPad Software Inc., La Jolla, CA) version 7.0. Sample sizes were determined a priori using a two-sided log rank test with an overall sample size of 30 mice (15 in HIFU + α CTLA-4 + α PD-L1 and 15 in untreated) which achieved a power of 76% at 0.05 significance level to detect a difference of survival proportion. Tumor growth curves are presented as tumor volume over time. Kaplan-Meier plots were populated for all groups post-treatment to demonstrate mice survival. Significance was assessed by log-rank test (Mantel-Cox test). Earlier time points were assessed using Gehan-Breslow-Wilcoxon test and were together presented as percent survival (mean \pm standard error). One-way nonparametric ANOVA, followed by Bonferroni correction was used to compare all experimental groups in both ELISA and flow cytometry data. Confidence interval of 95% was used for all tests. Empirical Bayes approach was used to analyze probe-wise microarray gene data and compute t-statistics, F-statistic, and log-odds of differential expression.

5.3.5 Time to Boil

Time-to-boil for BH was estimated for the applied acoustic power in our experiments. Ultrasound waves at the focal zone induce heating. This rate of this heating can be calculated using weak shock theory (51), as follows:

$$H = \frac{\beta f_o A_s^3}{6\rho_o^2 c_o^4}$$

where H is the heating rate, f_o is the ultrasound frequency, A_s is in-situ shock amplitude, ρ_o is density of the medium, and c_o is the speed of sound in the tissue. If the heating rate is sufficiently high, the effect of heat conduction to surrounding regions can be low and neglected. Using the heating rate, the time-to-boil can be calculated as:

$$t_b = \frac{\Delta T c_v}{H}$$

where ΔT is the difference between 100°C and local temperature and c_v is the heat capacity/volume. We used the following constants based on prior report³⁹ to calculate both heating rate and time-to-boil in the tumor tissue: $\beta = 4.1$, $f_o = 1.5$ MHz, $\rho_o = 1050$ kg/m³, $c_o = 1580$ m/s, $c_v = 3540 \times 10^3$ J/m³/°C.

5.3.6 ELISA

Whole blood samples were drawn from terminal cardiac puncture post euthanasia. Blood serum was extracted from these samples for ELISA. We used a commercially available ELISA multiplex kit (U-plex, Meso Scale Diagnostics, Rockville, MD). This kit was used to quantify the following relevant cytokines: GM-CSF, IFN gamma, IL-10, IL-2, IL-4, IL-6, VEGF-A, and TGF-Beta1, and TGF-Beta2. TGF-Beta (latent plus active) was run independently using acidified serum. For acidification, 1M HCL was incubated with serum at RT for 10 min, before neutralization with ~6 µl of 1M NaOH/0.5 M HEPES per 50 µl volume. All assays were carried out according to manufacturer's instruction, briefly, plates were coated with primary biotinylated capture antibody plus linker solution, then washed, and 25 µl of calibrator standard (in dilutions for standard curve) or serum samples were added in duplicates into the diluent, and incubated for 1 hr. Following incubation, plates were washed 3 times with PBS/Tween-20 wash buffer, and MSD gold sulfo-tag detection antibodies were applied for 1 hr. Plates were then washed 3 times again, and then read on a MESO QuickPlex SQ12 detector (MesoScale Diagnostics, Rockville, MD). Standard curves

Mechanical HIFU-triggered Immune Sensitization of Refractory Murine Neuroblastoma

were plotted (4-parameter logistic curve) and analyzed with Mesoscale Discovery Workbench 4.0 software.

5.3.7 Flow Cytometry

Spleen, tumor draining lymph node, contralateral lymph node, and tumor tissues were harvested immediately after mice were sacrificed and manually dissociated to obtain a single cell suspension. Cells were washed and re-suspended in 1×PBS for staining with Live Dead Aqua (Invitrogen) for 25 min at 4°C. Cells were washed with 1×PBS/2% FCS, and re-suspended in 100 µL of Foxp3 fix/perm buffer (eBioscience) for 30 min at 4°C. Cells were washed twice in 1x perm wash solution, and re-suspended in 100 µL of 1×Perm Wash solution for antibody specific staining. Cells were stained with antibodies against eFluor 450 CD4+ (RM4-5), APC-eFluor 780 CD8+ (53-6.7), PE Foxp3+ (FJK-16s), CD45+, APC CD11c+ (N418), PerCP-Cyanine5.5 CD11b+ (M1/70), and PE-Cyanine7 CD49b (DX5+) for 30 min at 4°C obtained from eBioscience. Cells were washed twice with 1×perm wash, and re-suspended in 100 µL 1x perm wash for analysis on a 13-color Cytex DXP flow cytometer.

5.3.8 Immunohistochemistry

Tumor tissue sections were cut into five µm-thick sections that were then formalin-fixed paraffin-embedded (FFPE). Hematoxylin and eosin, CD4+ (ab183685, Abcam, Cambridge, UK), CD8α+ (ab203035, Abcam, Cambridge, UK), CD68+ (ab125212, Abcam, Cambridge, UK), DAPI and PD-L1 (E1L3N, #77563, Cell Signaling, Danvers, MA) antibodies were used to stain tumor sections. These sections were imaged under a bright field microscope (BX-61, Olympus, Waltham, Massachusetts, USA) at 2x, 4x, 10x, and 40x. Resulting image sections were processed and quantified in the HSV color scheme in MATLAB (MathWorks, Natick, MA, USA).

5.3.9 Gene Expression & qRT-PCR

We performed a preliminary microarray analysis and verified changes in specific genes by quantitative reverse transcriptase-polymerase chain reaction (qRT-PCR). We specifically tested seven genes, based on their role in mediating anti-tumor cellular and cytokine responses post-HIFU³⁵. These are S100 calcium binding protein A8 (S100a8) and A9 (S100a9), heat shock protein family, member 7 (Hspb7), heat shock protein family A member 1B (Hspa1b or Hsp70), high mobility group box 1 (Hmgb1), lipocalin 2 (Lcn2), and Cd72. Tumors were excised pre- and post-HIFU treatment, and immediately frozen at -80°C. To ensure equal distribution of all tumor regions, frozen tumors were pulverized to a powder under liquid nitrogen in a mortar and pestle. Powder was divided into frozen 1.5 ml tubes, and stored at -80°C. To isolate RNA, guanidinium isothiocyanate containing lysis RLT buffer was added directly to the samples, and after homogenization, processing and cleanup continued following manufacturer's instructions using the RNeasy Maxi prep protocol (Qiagen, Germantown, MD). RNA quality was assessed by spectrophotometer and bioanalyzer analysis.

mRNA (250 ng) was analyzed on Affymetrix Mouse Clariom S arrays using standard reagents and following the Affymetrix protocol (ThermoFisher Scientific, Waltham, MA). Poly A controls were spiked into the reactions. Briefly, RNA was converted to cDNA, which was then in vitro transcribed into cRNA that was bead purified. Fifteen µg of purified cRNA was converted into ss-cDNA, which was then fragmented, cleaned, and hybridized (2.3 µg) for 16 hr (45°C) to the arrays. Hybridization solution was removed and arrays were washed and stained on an Affymetrix Fluidics 450 station and scanned with the Affymetrix GeneChip scanner. Data were analyzed with Transcriptome Analysis Console (4.0) software using the default setting and the RMA algorithm for normalization. Raw intensity values are background corrected, log₂ transformed and then quantile normalized.

Microarray data were validated with semi-quantitative Taqman qRT-PCR (ThermoFisher Scientific, Waltham, MA). Total RNA (250 ng) was converted into cDNA using a high capacity

Mechanical HIFU-triggered Immune Sensitization of Refractory Murine Neuroblastoma

cDNA reverse transcription kit (ThermoFisher Scientific, Waltham, MA). PCR was then performed using the following probes for expression of genes of interest: 1) Lcn2 (Mm01324470_m1), 2) Cd72 (Mm00514264_g1), 3) Hmgb1 (Mm00849805_g1), 4) S100a8 (Mm00496696_g1), 5) S100a9 (Mm00656925_m1), 6) Hspb7 (Mm04210487_m1), 7) Hsp70 (Mm01159846_s1), and 3 housekeeping genes: 1) GAPDH (Mm99999915_g1), 2) GUSB (Mm00446953_m1), 3) ACTB (Mm00607939_s1).

5.4 Results

5.4.1 HIFU in combination with α CTLA-4 + α PD-L1 cures refractory, unilateral neuroblastoma tumors, leading to significant long-term survival

To assess the role of HIFU mechanical fractionation in survival efficacy, we partially treated large, refractory Neuro2a tumors in mice. Treatment using HIFU alone or in combination with single checkpoint inhibitors alone was not effective and had no survival benefit (Fig. 1D, blue, black and, orange lines). Additionally, treatment with both α CTLA-4 + α PD-L1 (without HIFU) resulted in marginal survival (10%, Fig. 1D, red line). In contrast, HIFU combined with α CTLA-4 + α PD-L1 resulted in complete tumor regression at the primary site, with no distant metastases (Fig. 1C) and significantly increased long-term survival (>300 days, $p < 0.0001$) from 0% (untreated, HIFU only, HIFU + α CTLA-4 or HIFU + α PD-L1) to 62.5% (Fig. 1D, green line). Tumor volumes compared 28 days after treatment demonstrate that tumors treated with HIFU + α CTLA-4 + α PD-L1 were significantly smaller when compared to tumors treated with α CTLA-4 + α PD-L1 alone ($p = 0.0241$) (fig. S1). These results demonstrate that HIFU induces a strong synergistic effect when combined with α CTLA-4 + α PD-L1, and leads to long-term survival in a previously untreatable, refractory neuroblastoma tumor model.

Chapter 5

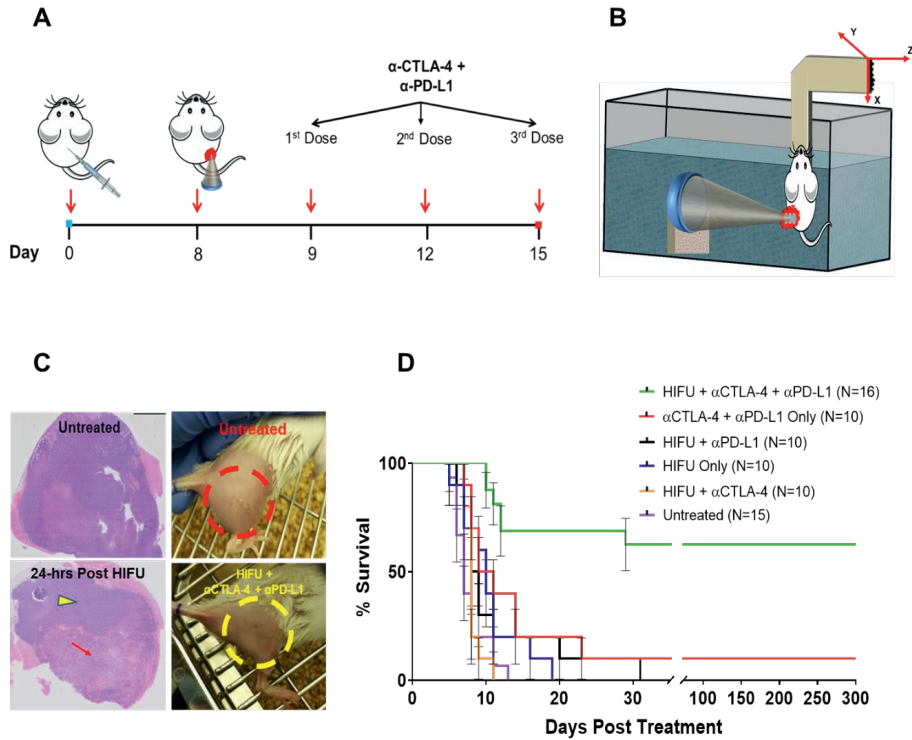


Figure 1. Adding HIFU to α CTLA-4 + α PD-L1 significantly increases survival in mice.

(A) Experimental timeline for treating mice with large, established unilateral neuroblastoma tumors using combination of HIFU and α CTLA-4 + α PD-L1. Mice were inoculated on day 0, tumors treated with HIFU on day 8, followed by a regimen of α CTLA-4 + α PD-L1. (B) Mice are held using an arm connected to a computer-controlled 3D positioning system, and the lower half of the mice's body is submerged into a water bath filled with circulating degassed water at $\sim 33^{\circ}\text{C}$. Three adjacent, non-overlapping HIFU foci ($1.5 \times 1.5 \times 7$ mm each) are positioned in the middle of the tumor. (C) H&E-stained histological sections obtained 24-hours after HIFU, demonstrating tumor fractionation and necrosis (red arrow), adjacent to intact tumor (yellow arrowhead). Representative photographs of mice with and without tumors. Red dashed-circle shows typical tumors, measuring ~ 1200 - 1750 mm^3 that were treated in this study, while yellow dashed-circle shows a completely tumor-free mouse after HIFU + α CTLA-4 + α PD-L1 treatment, with no evidence of iatrogenic effects from HIFU treatment. (D) Kaplan-Meier plots of six groups of mice with unilateral established tumors treated with either individual or combinational approaches. HIFU + α CTLA-4 + α PD-L1

Mechanical HIFU-triggered Immune Sensitization of Refractory Murine Neuroblastoma

was the only group to show significantly higher survival compared to all other groups, with more than 62% of mice surviving beyond 300 days post- treatment.

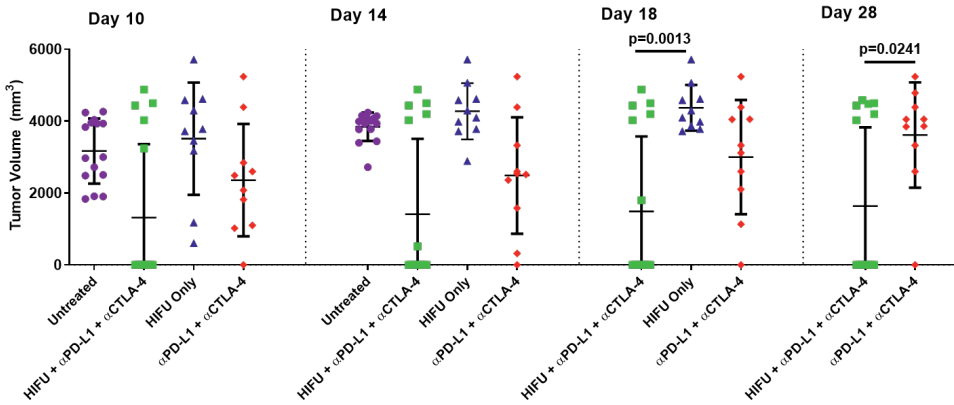


Figure S1. Time-lapse of tumor growth in untreated mice and mice treated with HIFU+ αCTLA-4 + αPD-L1, HIFU alone, and αCTLA-4 + αPD-L1.

Tumor volumes at day 10, 14, 18, and 28 for untreated mice (N = 15) and mice treated with HIFU+ αCTLA-4 + αPD-L1 (N = 16), HIFU alone (N = 10), and αCTLA-4 + αPD-L1 (N = 10) are displayed. By day 28, only mice treated with HIFU+ αCTLA-4 + αPD-L1 show reduced tumor volumes, while mice from all other groups display high and terminal tumor volumes. ($p = 0.0013$ for HIFU+ αCTLA-4 + αPD-L1 vs HIFU alone on day 18, and $p = 0.0241$ for HIFU+ αCTLA-4 + αPD-L1 vs αCTLA-4 + αPD-L1 on day 28).

5.4.2 Local HIFU treatment alone induces systemic cellular, cytokine, and gene response

Since HIFU was applied locally to fractionate tumors, we first sought to measure any loco-regional and systemic immune responses at 24, 48, and, 72-hours after HIFU alone (Fig. 2A-D).

Temporal evolution of cellular response in tumor, lymph nodes, and spleen

Untreated tumors did not have any infiltration of CD4+ and/or CD8α+ cells, although some resident macrophages (CD68+) were detected (fig. S2). Significant infiltration of both CD4+ and CD8α+ cells was observed in the treated tumor at 24-hours after HIFU alone (fig. S2, $p = 0.0001$

Chapter 5

and 0.033, respectively). This was accompanied by a significant increase in CD68⁺ cells at 48-hours, compared to untreated tumors (fig. S2, $p = 0.0377$). Significant increase in NK cells (DX5⁺) was measured in both spleen and tumor draining lymph nodes at 24-hours post-HIFU ($p = 0.0006$ and $p = 0.0004$, respectively, Fig. 2A), with a non-significant increase observed in the contralateral lymph nodes (fig. S3). At this time-point, dendritic cell (DCs, CD11c⁺) population also moderately increased in spleen, tumor draining lymph nodes, and contralateral lymph nodes (Fig. 2A & fig. S3), while CD8 α ⁺ DCs (CD8 α +CD11c⁺) subset significantly increased at 24-hours post HIFU in both spleen and tumor draining lymph nodes ($p = 0.0001$ and 0.0002 , respectively). At 48-hours post treatment, HIFU also caused a significant reduction in CD4⁺ subset of regulatory T-cells (CD4+Foxp3⁺) in the tumor draining lymph nodes ($p = 0.0200$). Likewise, at 72-hours, CD4+Foxp3⁺ population was significantly lower in the spleen and tumor draining lymph nodes ($p = 3.5e-9$ and $p = 0.0001$, respectively, Fig. 2A). CD4+Foxp3⁺ population remained unchanged in the contralateral lymph nodes at all time-points after HIFU (fig. S3). Given that a higher cytotoxic to regulatory T-cell ratio (CD8 α ⁺/Foxp3⁺) has been previously shown to signify favorable outcomes in several cancer types^{40,41}, we measured this cell ratio post-HIFU. CD8 α ⁺/Foxp3⁺ cell ratios were significantly elevated in both spleen and tumor draining lymph nodes at 72-hours post-HIFU treatment ($p = 0.0021$ and 0.0091 , respectively). We observed no significant changes in CD11b^{high} in spleen and tumor draining lymph nodes. These results show an early and marked increase in local immune cell infiltration of the tumor after HIFU.

Mechanical HIFU-triggered Immune Sensitization of Refractory Murine Neuroblastoma

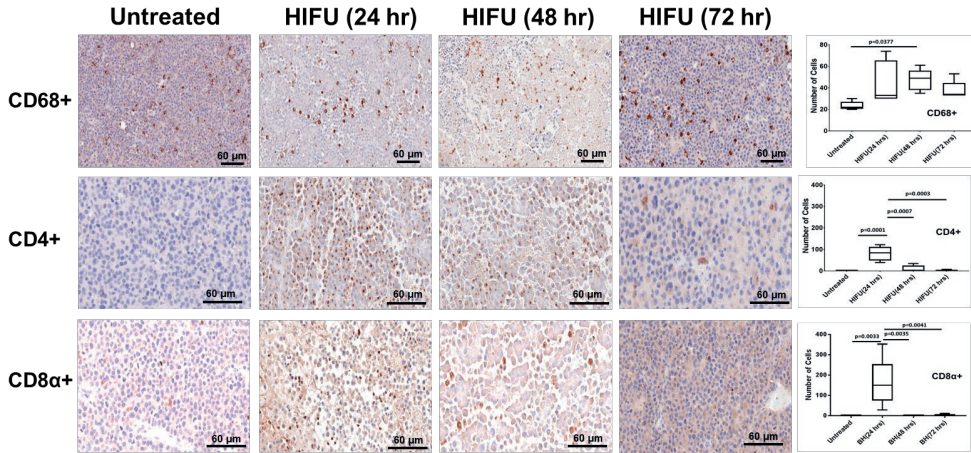


Figure S2. Immune cell infiltration within neuroblastoma tumors pre- and at 24, 48, & 72-hrs post-HIFU alone.

Untreated tumors presented no CD4+ or CD8α+ cell infiltration, albeit some macrophage cell infiltration. In contrast, 24-hrs post-HIFU stimulated a significant increase in CD68+, CD4+, and CD8α+ cell within the tumor, which slowly return to baseline by 72-hrs after HIFU. This suggests a strong acute immune response activated by HIFU treated of the tumors.

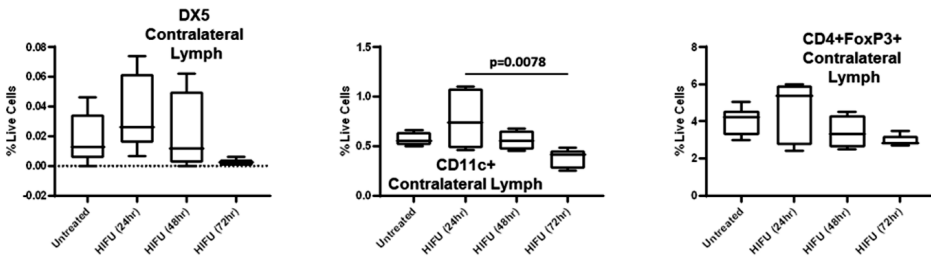


Figure S3. Circulating cellular profile in contralateral lymph nodes after treating mice with HIFU only.

DX5+, CD11c+, and CD4+Foxp3+ cell populations were measured in the contralateral lymph nodes in untreated mice and after 24, 48, and 72 after HIFU. All three cell types demonstrated insignificant increase after HIFU when compared to untreated population. There was however, a significant decrease in CD11c+ in the contralateral cell population from 24 to 72 hrs ($p = 0.0078$).

Intra-tumoral expression of PD-L1 post-HIFU

We further investigated the role of HIFU alone in altering the PD-L1 – PD-1 axis by measuring intratumoral PD-L1 expression. Untreated neuroblastoma tumors presented no PD-L1 expression (Fig. 2B). In contrast, there was a significant increase in PD-L1 expression on most tumor cells at 72-hours after HIFU treatment compared to untreated tumor (Fig. 2B, $p = 0.0001$). This acute increase in PD-L1 expression at 72-hours following HIFU suggests adaptive tumor immunity suppression, and loss of CD4 population (fig. S2). Thus anti-PD-L1 treatment is critical for countering this effect and enhancing anti-tumor immune responses ⁴².

Temporal progression of systemic inflammatory cytokines after HIFU

We then evaluated circulating inflammatory cytokine changes at 24, 48, and 72-hours post-HIFU alone (Fig. 2C). At 24-hours post-HIFU we observed significant increase in interleukin-2 (IL-2) ($p = 0.0148$) and granulocyte-macrophage colony-stimulating factor (GM-CSF) ($p = 0.0454$), plus a significant decrease in vascular endothelial growth factor-A (VEGF-A) ($p = 0.0072$). At 48-hours post-HIFU interleukin-6 (IL-6) ($p = 0.0298$) was significantly upregulated, whilst significantly lower concentrations in interleukin-10 (IL-10) ($p = 0.0227$) were measured. Further, at 72-hours post-HIFU, IL-10 continued to significantly decrease ($p = 0.0314$), and in contrast interferon- γ (IFN- γ) was significantly higher at 72-hours ($p = 1.7e-5$). We also measured no significant changes in TGF- β 1, TGF- β 2 (Fig. 2C), TNF- α , IL-12p70, or IL-4 after HIFU treatment (fig. S4).

significant decrease in CD11c+ in the contralateral cell population from 24 to 72 hrs ($p = 0.0078$).

Mechanical HIFU-triggered Immune Sensitization of Refractory Murine Neuroblastoma

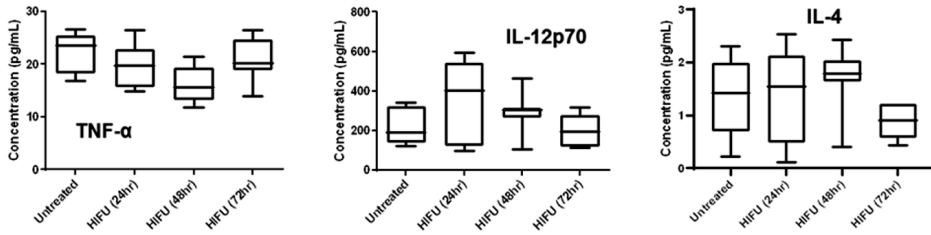


Figure S4. Effect of HIFU alone at 24, 48 and 72 hrs on circulating cytokines.

TNF- α , IL-12p70, and IL-4 were measured from cardiac blood in untreated mice and in mice once treated with HIFU at 24, 48, and 72 hrs. These systemic cytokine measurements did not indicate significant changes at any time point post-HIFU.

Gene expression within HIFU-treated tumors

We further characterized intra-tumor genetic patterns 24, 48, and 72-hours following HIFU treatment (Fig. 2D). S100 calcium binding protein A8 (S100a8), S100 calcium binding protein A9 (S100a9), heat shock protein family, member 7 (Hspb7), and lipocalin 2 (Lcn2), were overexpressed significantly at all three time-points, while heat shock protein family A member 1B (Hsp70) and Cd72 expression were significantly overexpressed at 24 and 48-hours post-HIFU, and high mobility group box 1 (Hmgb1) expression did not change post-HIFU.

In summary, our collective evidence from cellular phenotype changes, cytokine, and genetic signatures suggest that HIFU treatment of previously refractory neuroblastoma results in early immune cell presence in the tumor, lymph nodes and spleen, converting a non-immunogenic 'cold' tumor to an immunogenic 'hot' tumor.

Chapter 5

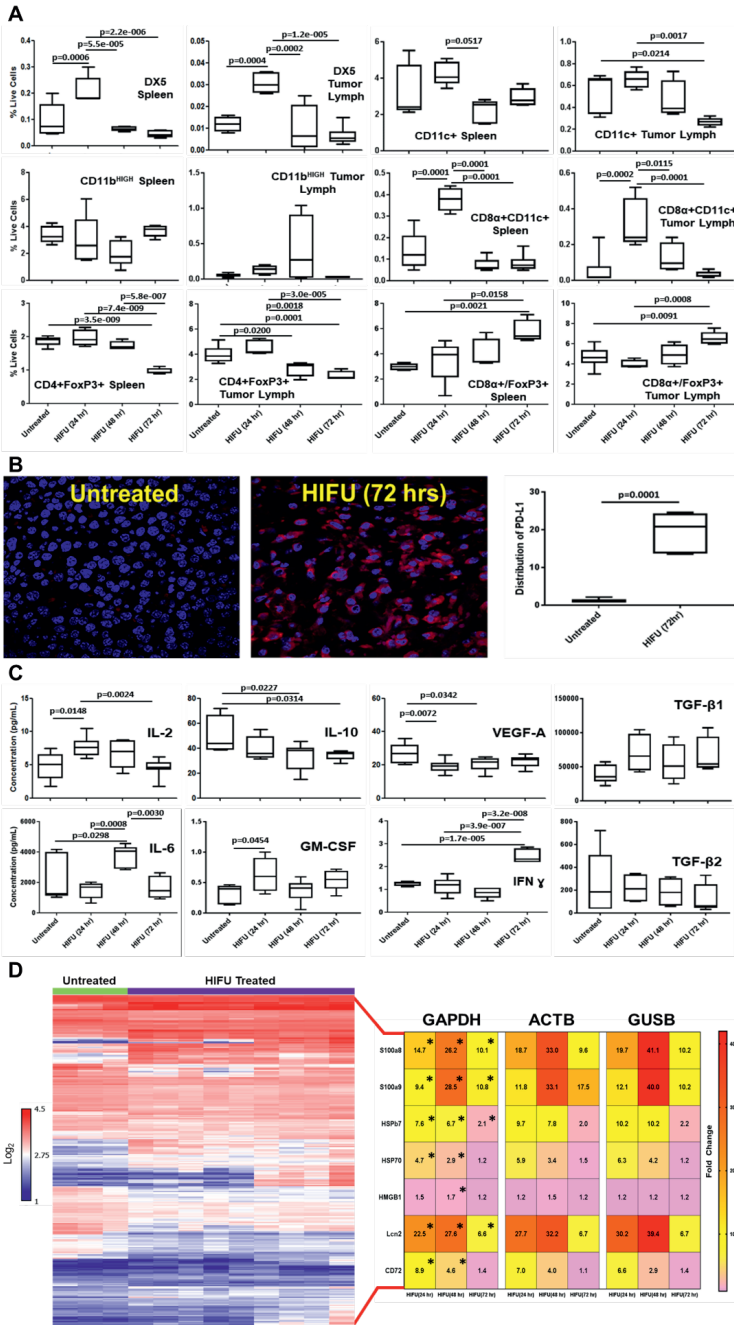


Figure 2. Systemic cellular, cytokine and genetic signature caused by HIFU mechanical fractionation alone of neuroblastoma tumor.

(A) Box plots presenting cellular changes as percent live cells in the spleen and tumor-draining lymph nodes of mice at 24, 48, and 72-hours following HIFU were compared against cellular changes in untreated mice. Percentage of CD4+Foxp3+, CD11c+, DX5+ (NK cells), CD11b^{high}, ratio of CD8+/CD4+Foxp3+, and CD8 α +CD11c+ were evaluated using flow cytometry. (B) Representative fluorescent microscopy images of tumor tissues stained with DAPI (blue stain) + PD-L1 (red stain) obtained from untreated mice and from mice at 72-hours post-HIFU. (C) Box plots presenting circulating cytokines in mice at 24, 48, and 72-hours post-HIFU and untreated mice in pg/mL (IL-2, VEGF-A, IL-10, TGF- β 1, GM-CSF, IL-6, IFN- γ , and TGF- β 2) measured using ELISA from terminal cardiac blood draw. (D) Microarray data from untreated, 24, 48, and 72-hours post-HIFU, represented as log₂ change. This was followed-up by qRT-PCR analysis of seven key genes repeated for three different housekeeping genes (GAPDH, ACTB, and GUSB). N \geq 8 tumors per time-point for each housekeeping gene were used. Asterisks in GAPDH columns represent significance from untreated tumors ($p < 0.05$), and was significantly high in gene expression for ACTB and GUSB housekeeping genes as well. Significance values for all data analysis were calculated using ANOVA with Bonferroni correction ($p < 0.05$).

5.4.3 Systemic immune effects are sustained after HIFU in combination with α CTLA-4 + α PD-L1 and results in systemic ‘abscopal’ effect and, prolonged survival

Similar to studying immune effects of HIFU only above, we analyzed circulating cytokine and systemic cellular changes in these mice at 24, 48, and 72-hours after the last dose of α CTLA-4 + α PD-L1. We observed significant intratumoral infiltration of helper T-cells (CD4+), cytotoxic T-cells (CD8 α +), as well as CD8 α + dendritic cells (CD8 α +CD11c+) at 48-hours after the last dose of checkpoint inhibitors (Fig. 3A). In addition, significant CD8 α +CD11c+ infiltration into the draining lymph nodes and spleen was measured after the last dose of checkpoint inhibitors (Fig. 3A). CD11c+ infiltration into draining and contralateral lymph nodes, as well as systemic cytokine changes were observed after the last dose of checkpoint inhibitors (Fig. 3A).

Chapter 5

IFN- γ was significantly elevated at 24-hours after the last dose of α CTLA-4 + α PD-L1 regime ($p = 0.0043$). These IFN- γ levels in circulating blood are similar in mice at 72-hours post-HIFU only, suggesting a sustained IFN- γ elevation at day 8 after treating tumors with HIFU. In contrast, mice receiving just α CTLA-4 + α PD-L1 and not supplemented by HIFU did not see any changes in IFN- γ concentration systemically (fig. S6). In addition, IL-10 significantly reduced by at least 10-fold at 24, 48, and 72-hours after the last dose of α CTLA-4 + α PD-L1 compared to untreated mice ($p = 8.9e-10$, $3.5e-11$, and $2.7e-10$, respectively). IL-6 was significantly lower at 72-hours after the last dose ($p = 0.0221$), while GM-CSF was significantly elevated at 72-hours after the last dose ($p = 0.0119$). This downward trend in systemic IL-10 concentration is similarly observed in HIFU only treatment of mice with unilateral tumors, suggesting a sustained effect at 10 days after HIFU. Population of dendritic cells (CD11c+) in tumor draining lymph nodes significantly increased at 48-hours compared to untreated mice ($p = 3.3e-6$), noticeably increasing in contralateral lymph nodes at 48-hours post final dose of α CTLA-4 + α PD-L1, suggesting systemic antigen presenting capability. Also, the frequency of both CD4+ and CD8 α + cells were found to be elevated in tumor at 48-hours after the last dosage of α CTLA-4 + α PD-L1 compared to untreated mice ($p = 0.0363$), and 24-hours after the last dose of checkpoint inhibitors ($p = 0.0070$). CD8 α +CD11c+ cells were significantly elevated intratumorally, in the spleen and in draining lymph node at 48-hours after the last dose of α CTLA-4 + α PD-L1 ($p = 0.0054$, 0.0001 , and 0.0010 , respectively). CD11b^{low} in the spleen was significantly elevated at 24-hours after the last dose of α CTLA-4 + α PD-L1 ($p = 0.0165$). In addition, CD11b^{high} population in the spleen was also significantly elevated at 24-hours post final α CTLA-4 + α PD-L1 dose compared to untreated mice ($p = 0.0318$). In contrast, mice treated with HIFU only did not show any changes in CD11b^{low}. The CD4+Foxp3+ cell population remained unchanged in both tumor draining and contralateral lymph nodes after the last dose of α CTLA-4 + α PD-L1, although they significantly reduced in mice treated with HIFU alone.

Mechanical HIFU-triggered Immune Sensitization of Refractory Murine Neuroblastoma

Given the local and systemic immunologic changes with HIFU alone and in combination with α CTLA-4 + α PD-L1, we hypothesize that local unilateral tumor fractionation using HIFU in combination with α CTLA-4 + α PD-L1 induces an abscopal effect in mice with established bilateral tumors ($>500 \text{ mm}^3$ on each side, $>1000 \text{ mm}^3$ total tumor burden) (Fig. 3B). We locally treated one side only with HIFU, and followed up with a regimen of systemic α CTLA-4 + α PD-L1 (similar to Fig. 1A). Interestingly, combining α CTLA-4 + α PD-L1 with one-sided HIFU tumor fractionation resulted in complete bilateral tumor regression (Fig. 3B). By day 20, 75% of mice had no tumors, bilaterally (fig. S5). There was a significant improvement in survival ($p = 0.0001$) compared to mice with unilateral tumors treated with checkpoint inhibitors or HIFU only (Fig. 3C). Overall, 61.1% of mice survived longer than 300 days in this group, with no evidence of local or systemic tumor recurrence. These results provide vital evidence of local treatment of tumor with HIFU in combination with α CTLA-4 + α PD-L1 cause a sustained systemic immune-adjuvant effect.

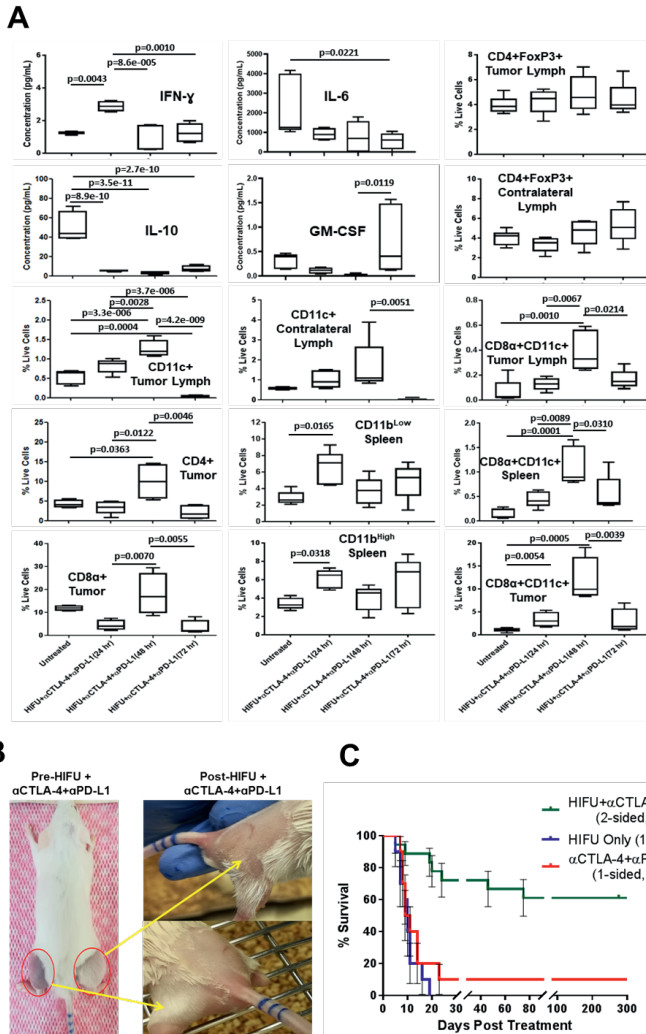


Figure 3. HIFU + α CTLA-4 + α PD-L1 treatment of large, established bilateral tumors leads to abscopal effect.

(A) Box plots showing cytokine concentration (pg/mL) and cellular changes (percent live cells), quantified at 24, 48, and 72-hrs after HIFU and the last dose of α CTLA-4 + α PD-L1 and, compared with untreated mice. Significance values for all data analysis were calculated using ANOVA ($p < 0.05$). (B) Representative photographs of mouse with established and large bilateral neuroblastoma tumors (red circles). After unilateral treatment with HIFU + α CTLA-4 + α PD-L1, both tumors completely regressed, signifying strong

Mechanical HIFU-triggered Immune Sensitization of Refractory Murine Neuroblastoma

abscopal effect. (C) Kaplan-Meier plot showing survival of mice with bilateral neuroblastoma tumors treated with HIFU + α CTLA-4 + α PD-L1 (N = 18). 61.1% of mice with bilateral tumors treated with HIFU + α CTLA-4 + α PD-L1 displayed significantly higher survival compared to mice with treated with HIFU only or α CTLA-4 + α PD-L1 only, beyond day 300.

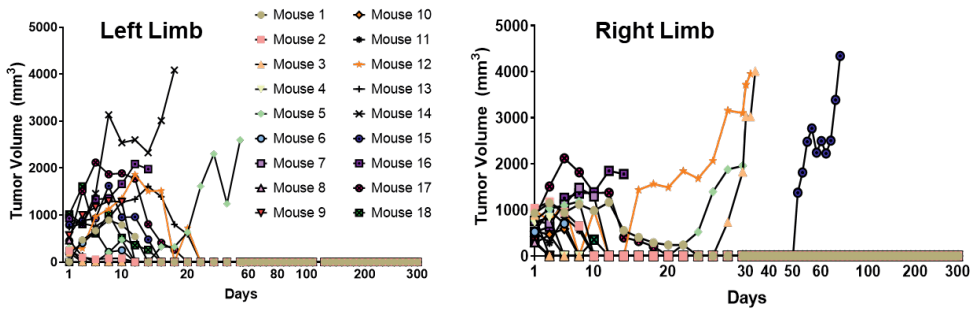


Figure S5. Tumor growth curves of left and right limbs of mice with bilateral tumors.

Tumor volumes of left and right limbs of mice (N = 18) treated with HIFU on one limb only, followed by a regimen of α CTLA-4 + α PD-L1. More than 62% of mice were tumor free by day 30.

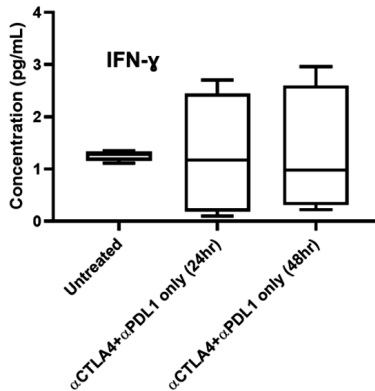


Figure S6. Effect of α CTLA-4 + α PD-L1 only at 24 and 48 hrs after last checkpoint inhibitor dose on IFN- γ .

Concentration of IFN- γ at 24 and 48-hrs after the last dose of checkpoint inhibitor combination dose did not significantly vary when compared to cardiac blood of untreated mice.

5.4.4 HIFU mediated tumor fractionation combined with checkpoint inhibitor using α CTLA-4 + α PD-L1 induces effector memory cells

In view of the fact that HIFU treated tumors continued to regress well beyond the treatment period and the abscopal effect, we re-challenged all surviving mice with twice the number of tumor cells (2×10^6 cells) compared to the initial inoculation (1×10^6 cells). Intriguingly, all mice survived this re-challenge for at least 75 days, tumor free without any evidence of tumor formation (Fig. 4A), except for two mice that demonstrated transient tumor formation, which eventually regressed by day 21 (fig. S7A). To determine the cellular mediator of this systemic effector memory response, we measured $CD4+CD44^{hi}CD62L^{low}$ and $CD8\alpha+CD44^{hi}CD62L^{low}$ cells in the spleen. The percentage of $CD4+$ and $CD8\alpha+$ cells expressing effector memory markers in mice that were re-challenged were 3 and 17 folds greater than in naïve mice ($p = 0.0001$, Fig. 4B & C). To further support the hypothesis of induction of long-term memory response following HIFU and checkpoint inhibitor treatment, we adoptively transferred the isolated T-cells from mice surviving combination therapy into mice with *de novo* established tumors (volume: 600-900 mm^3). We found significant tumor growth retardation and prolonged survival in mice that received adoptive T-cells compared to mice that did not receive adoptive T-cells ($p = 0.0002$) (fig. S7B). Combining HIFU with α -CTLA-4 + α -PD-L1 in previously untreatable and refractory neuroblastoma tumor not only effectively induced tumor regression and systemic abscopal effect, but also induced a long-term immune memory response.

Mechanical HIFU-triggered Immune Sensitization of Refractory Murine Neuroblastoma

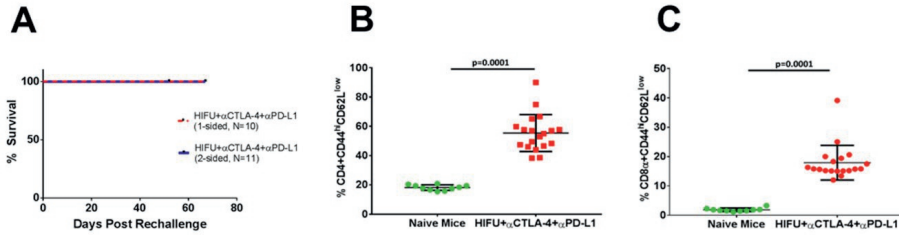


Figure 4. Mice surviving HIFU + αCTLA-4 + αPD-L1 treatment possess significantly high effector memory against neuroblastoma tumors.

(A) Kaplan-Meier plot shows 100% survival in mice re-challenged with 2x the initial tumor inoculation (2×10^6 vs 1×10^6). Mice from both unilateral and bilateral tumor groups were re-challenged and all mice survived. (B) Box plot showing significantly higher effector memory on CD4+ cells in mice treated with HIFU + αCTLA-4 + αPD-L1 compared to naïve mice (C) Box plot presenting significantly higher effector memory on CD8+ cells in mice treated with HIFU + αCTLA-4 + αPD-L1 compared to naïve mice. P-values were determined using unpaired Welch's t-test.

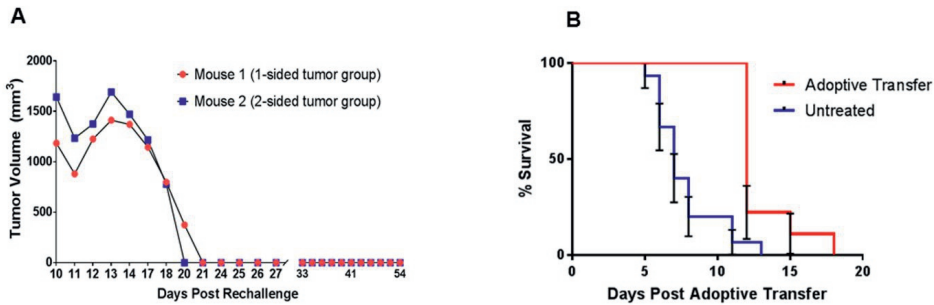


Figure S7. Immune memory effects in mice treated with HIFU+ αCTLA-4 + αPD-L1

(A) Tumor growth curves showing two mice (one mouse from the unilateral tumor group and one mouse from the bilateral tumor group) that presented a transient tumor volume increase up to ~1500 mm³ after tumor-cell rechallenge, which eventually regressed by day 21 post-rechallenge. This is an important result that suggests tumor-cell immunity in mice that were treated with HIFU+ αCTLA-4 + αPD-L1. (B) T-cells from surviving mice were adoptively transferred to naïve mice with de novo established tumors (volume:

Chapter 5

600-900 mm³). These mice survived longer than mice that did not receive an adoptive T-cell transfer ($p = 0.0001$), suggesting an adoptively transferrable immunity.

5.5 Discussion

In this study, we demonstrate that partial tumor fractionation using HIFU in combination with α CTLA-4 + α PD-L1 results in an abscopal effect and significantly prolongs survival in previously untreatable, large unilateral and bilateral murine neuroblastoma tumor models. Our results also provide a proof-of-concept for using HIFU to sensitize the systemic immune system, and serving as an adjuvant to checkpoint inhibitor therapy. We also reveal that this systemic anti-tumor effect is mediated by upregulation of dendritic cells, tumor infiltrating T-cells, proinflammatory cytokines, and DAMPs, as well as concurrent downregulation of pro-tumor regulators such as Foxp3, IL-10 and VEGF-A. Furthermore, this combination therapy elicits a systemic effector memory response that results in rejection of tumor re-challenge and can be adoptively transferred.

One of the most important findings in our study is that combining HIFU with α CTLA-4 + α PD-L1 significantly improves long-term survival of mice with large and established otherwise immunologically 'cold' neuroblastoma tumors. Tumors in mice were treated when the volume reached 1200-1750 mm³, which is significantly larger than prior reported work in similar or same tumor models^{27,28,38,43}. The HIFU foci were calculated to cover ~2% of total tumor volume, which may be clinically relevant in treating tumors in patients⁴⁴, where complete margin treatment may not be possible. Unlike HIFU-mediated thermal ablation, BH (modality of HIFU used in this study) is capable of mechanically fractionating tissues at high spatial precision and relatively low temperature elevation. In addition, BH's two-prong approach of debulking tumor tissue via mechanical fractionation while keeping major blood vessels intact^{30,45}, and simultaneously producing significant sterile inflammation⁴⁵, potentially improves efficiency of immune checkpoint inhibitors. The checkpoint inhibitors used in this study are clinically approved for multiple

Mechanical HIFU-triggered Immune Sensitization of Refractory Murine Neuroblastoma

indications and are currently in trials for treating neuroblastoma (NCT02304458)^{1,46}. Mechanically fractionating <10% of tumor volume with HIFU compared to thermally ablating more than 50% tumor volume, potentially reduces heat convective-associated iatrogenic effects, allows improved blood supply into the tumor and immune sensitization³⁷. These factors suggest mechanical fractionation using BH may lead to improved immune sensitization against tumor with little or no side effects compared to thermal ablation. This is potentially impactful in clinical translation of this drug-device combination therapy for patients suffering from high-risk or relapsed neuroblastoma, without other effective therapeutic options.

In the present study, we found three key mechanistic changes. First, HIFU-mediated mechanical fractionation of tumor tissue elevated concentrations of IFN- γ , while lowering concentrations of IL-10, and sustaining IL-4, TGF- β 1, and TGF- β 2. These cytokine changes help improve antigen presentation capability^{47,48} after HIFU-mediated mechanical fractionation of tumors. Tumor fractionation using HIFU also demonstrates remarkable DAMP changes. Key DAMPs such as S100a8/a9 and HSPs are upregulated post-HIFU, and are of key interest since they are known to bind to pattern recognition receptors (PRR) on the surface of innate immune cells, such as TLRs⁴⁹. These genes are also known to activate the S100a8/a9–NK cell axis via the receptor for advanced glycation end products (RAGE) pathway⁵⁰, facilitating dendritic cell maturation, and promoting immunogenic cell death (ICD)⁵¹. HIFU tumor fractionation increased HSP27 and HSP70 that may act as a chemoattractant to dendritic cells via the RAGE pathway (as observed in both preclinical and clinical studies)^{35,52}. We also mechanistically demonstrate the upregulation of CD72 gene, which is linked in inhibition of IFN- γ production by NK cells, although NK cell concentration significantly increased at 24-hrs. CD72 may have inhibited IFN- γ production by NK cells (without interfering with NK cell's cytotoxic abilities), leading to suppression of IFN- γ until 72-hours post-HIFU⁵³. We therefore conclude that 24-48 hours post-HIFU, a significant increase in macrophages, CD8 α + DCs, IFN- γ , T-cells, NK cells, and dendritic cells

Chapter 5

have converted a 'cold', non-immunogenic tumor to a 'hot', immunogenic tumor, but not adequate to improve overall survival.

Second, when HIFU tumor fractionation is combined with α CTLA-4 + α PD-L1, sustained systemic increase in CD11c+, CD8 α +CD11c+, CD4+, and CD8 α + populations, while inhibited IL-10 and CD4+Foxp3+ is observed, leading to abscopal effect and long-term survival in over 61.1% of mice. The presence of significantly high levels of CD11c+ in the draining lymph nodes after tumor fractionation, and downregulating CTLA-4 and PD-L1 suggests a more efficient T-cell priming and activation. Also, CD8 α +CD11c+ in the draining lymph nodes directly presents antigens to CD8 α + cells, leading to efficient priming and activation of CD8 α + cells. Combining HIFU tumor-fractionation with α PD-L1, improves T-cell based tumor targeting efficiency. This synergy between HIFU and checkpoint inhibitor therapy causing systemic cellular, cytokine, and DAMP release may have facilitated this effect, leading to significantly improved overall survival.

Third, HIFU in combination with α CTLA-4 + α PD-L1 improves long-term memory responses, and rejected tumor cell re-challenge with a strong adaptive immune response. Nineteen out of twenty-one mice rejected tumor re-challenge, while two presented transient tumor growth (1500-1800 mm³) before completely regressing by day 21 (fig. S7A). Overall, 100% mice initially treated with the HIFU + α CTLA-4 + α PD-L1 combination eventually survived the re-challenge sans further therapy. Since long-term memory markers CD4+CD44^{hi}CD62L^{low} and CD8 α +CD44^{hi}CD62L^{low} were found to be significantly elevated in re-challenged mice compared to untreated mice, suggesting HIFU's ability to improve T-cell memory. Adoptively transferring T-cells from surviving mice into naïve mice with established neuroblastoma tumor resulted in improved survival compared to mice that did not receive adoptive T-cells. This suggests a role of long-term memory T-cell response in slowing down established tumor growth. Alternatively, the increase in tumor infiltrating lymphocytes in the adoptive transfer group, may have induced upregulation of PD-L1 in the tumor, as well as the lack of α PD-L1, and may have prevented complete tumor regression and long-term survival.

Mechanical HIFU-triggered Immune Sensitization of Refractory Murine Neuroblastoma

Some important limitations remain unaddressed. Firstly, it would be valuable to assess the role of priming the immune system with α CTLA-4 prior to HIFU mechanical fractionation, followed by α PD-L1 in evaluating the role of T-cell priming and activation while reducing the potential effects of co-toxicity. Secondly, assessing the role of specific T-cell phenotypes after HIFU + checkpoint inhibitors, which may help support outcomes observed in this study. Finally, it may be interesting to assess the effect of treated tumor volumes in survival outcomes, and establish an 'exposure-response' relationship.

5.6 Conclusion

In conclusion, partial tumor fractionation of refractory neuroblastoma tumors in mice using HIFU enhances innate and adaptive cellular immunity, converting a 'cold' non-immunogenic tumor to a 'hot' immunogenic one. Combining this mode of HIFU with α CTLA-4 + α PD-L1 induces potent systemic immunity and cures mice with large, established unilateral and bilateral neuroblastoma tumors. In addition, HIFU treatment of these tumors leads to long-term immune memory. Our group has clinical experience in using HIFU for thermal tumor ablation in patients^{54,55} and we have previously demonstrated preclinical feasibility of performing tissue mechanical fractionation on the same clinical MR-HIFU system³². Thus, combining this technology with checkpoint inhibition is a step closer to clinical translation for patients with previously unresponsive primary neuroblastoma tumor with or without metastatic burden.

5.7 References

- 1 Merchant, M. S. *et al.* Phase I clinical trial of ipilimumab in pediatric patients with advanced solid tumors. *Clinical Cancer Research* **22**, 1364-1370 (2016).
- 2 Park, J. A. & Cheung, N.-K. V. Limitations and opportunities for immune checkpoint inhibitors in pediatric malignancies. *Cancer treatment reviews* **58**, 22-33 (2017).
- 3 Sharma, P., Hu-Lieskovan, S., Wargo, J. A. & Ribas, A. Primary, adaptive, and acquired resistance to cancer immunotherapy. *Cell* **168**, 707-723 (2017).
- 4 Ribas, A. *et al.* Pembrolizumab versus investigator-choice chemotherapy for ipilimumab-refractory melanoma (KEYNOTE-002): a randomised, controlled, phase 2 trial. *The lancet oncology* **16**, 908-918 (2015).
- 5 Irwin, M. S. & Park, J. R. Neuroblastoma. *Pediatric Clinics* **62**, 225-256 (2015).
- 6 Ries, L. A. G. *et al.* Cancer incidence and survival among children and adolescents. *United States SEER Program 1975-1995* (1999).
- 7 Pinto, N. R. *et al.* Advances in risk classification and treatment strategies for neuroblastoma. *Journal of clinical oncology* **33**, 3008 (2015).
- 8 Raffaghello, L. *et al.* Mechanisms of immune evasion of human neuroblastoma. *Cancer letters* **228**, 155-161 (2005).
- 9 Raffaghello, L. *et al.* Multiple defects of the antigen-processing machinery components in human neuroblastoma: immunotherapeutic implications. *Oncogene* **24**, 4634 (2005).
- 10 Contardi, E. *et al.* CTLA-4 is constitutively expressed on tumor cells and can trigger apoptosis upon ligand interaction. *International journal of cancer* **117**, 538-550 (2005).
- 11 Leach, D. R., Krummel, M. F. & Allison, J. P. Enhancement of antitumor immunity by CTLA-4 blockade. *Science* **271**, 1734-1736 (1996).
- 12 Prapa, M. *et al.* A novel anti-GD2/4-1BB chimeric antigen receptor triggers neuroblastoma cell killing. *Oncotarget* **6**, 24884 (2015).
- 13 Zeng, Y. *et al.* Anti-neuroblastoma effect of ch14. 18 antibody produced in CHO cells is mediated by NK-cells in mice. *Molecular immunology* **42**, 1311-1319 (2005).
- 14 Marquez-Medina, D., Salla-Fortuny, J. & Salud-Salvia, A. Role of gamma-delta T-cells in cancer. Another opening door to immunotherapy. *Clinical and Translational Oncology* **14**, 891-895 (2012).
- 15 Chakrabarti, L., Morgan, C. & Sandler, A. D. Combination of Id2 knockdown whole tumor cells and checkpoint blockade: a potent vaccine strategy in a mouse neuroblastoma model. *PLoS One* **10**, e0129237 (2015).
- 16 Pardoll, D. M. The blockade of immune checkpoints in cancer immunotherapy. *Nature Reviews Cancer* **12**, 252 (2012).
- 17 Zhu, X. *et al.* Severe cerebral edema following nivolumab treatment for pediatric glioblastoma: case report. *Journal of Neurosurgery: Pediatrics* **19**, 249-253 (2017).
- 18 Leen, A. M., Rooney, C. M. & Foster, A. E. Improving T cell therapy for cancer. *Annu. Rev. Immunol.* **25**, 243-265 (2007).
- 19 Sietsma, H. *et al.* Inhibition of hemopoiesis in vitro by neuroblastoma-derived gangliosides. *Cancer research* **58**, 4840-4844 (1998).
- 20 Shurin, G. V. *et al.* Neuroblastoma-derived gangliosides inhibit dendritic cell generation and function. *Cancer research* **61**, 363-369 (2001).
- 21 Zou, W. Immunosuppressive networks in the tumour environment and their therapeutic relevance. *Nature reviews cancer* **5**, 263 (2005).
- 22 Chin, J. L. *et al.* Results of salvage cryoablation of the prostate after radiation: identifying predictors of treatment failure and complications. *The Journal of urology* **165**, 1937-1942 (2001).
- 23 Dromi, S. A. *et al.* Radiofrequency ablation induces antigen-presenting cell infiltration and amplification of weak tumor-induced immunity 1. *Radiology* **251**, 58-66 (2009).
- 24 Livraghi, T. *et al.* Treatment of Focal Liver Tumors with Percutaneous Radio-frequency Ablation: Complications Encountered in a Multicenter Study 1. *Radiology* **226**, 441-451 (2003).
- 25 Poissonnier, L. *et al.* Control of prostate cancer by transrectal HIFU in 227 patients. *European urology* **51**, 381-387 (2007).
- 26 Chapman, A. & Ter Haar, G. Thermal ablation of uterine fibroids using MR-guided focused ultrasound-a truly non-invasive treatment modality. *European radiology* **17**, 2505-2511 (2007).

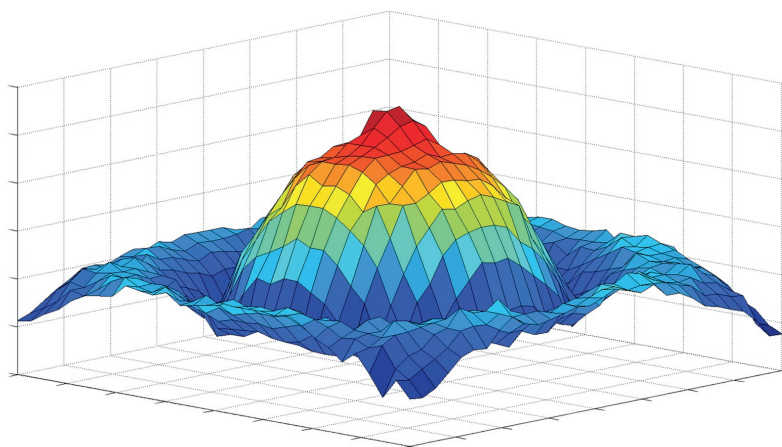
- 27 Silvestrini, M. T. *et al.* Priming is key to effective incorporation of image-guided thermal ablation into immunotherapy protocols. *JCI insight* **2** (2017).
- 28 Hu, Z. *et al.* Investigation of HIFU-induced anti-tumor immunity in a murine tumor model. *Journal of translational medicine* **5**, 34 (2007).
- 29 Eranki, A. *et al.* Mechanical fractionation of tissues using microsecond-long HIFU pulses on a clinical MR-HIFU system. *International Journal of Hyperthermia*, 1-12 (2018).
- 30 Khokhlova, V. A. *et al.* Histotripsy methods in mechanical disintegration of tissue: Towards clinical applications. *International Journal of Hyperthermia* **31**, 145-162 (2015).
- 31 Vlaisavljevich, E. *et al.* Histotripsy-induced cavitation cloud initiation thresholds in tissues of different mechanical properties. *Ultrasonics, Ferroelectrics, and Frequency Control, IEEE Transactions on* **61**, 341-352 (2014).
- 32 Eranki, A. *et al.* Boiling histotripsy lesion characterization on a clinical magnetic resonance imaging-guided high intensity focused ultrasound system. *PLoS one* **12**, e0173867 (2017).
- 33 Canney, M. S., Khokhlova, V. A., Bessonova, O. V., Bailey, M. R. & Crum, L. A. Shock-induced heating and millisecond boiling in gels and tissue due to high intensity focused ultrasound. *Ultrasound in medicine & biology* **36**, 250-267 (2010).
- 34 Eranki, A. *et al.* Tissue-mimicking thermochromic phantom for characterization of HIFU devices and applications. *International Journal of Hyperthermia* **36**, 518-529 (2019).
- 35 van den Bijgaart, R. J. *et al.* Thermal and mechanical high-intensity focused ultrasound: perspectives on tumor ablation, immune effects and combination strategies. *Cancer Immunology, Immunotherapy* **66**, 247-258 (2017).
- 36 Johnson, B. D., Yan, X., Schauer, D. W. & Orentas, R. J. Dual expression of CD80 and CD86 produces a tumor vaccine superior to single expression of either molecule. *Cellular immunology* **222**, 15-26 (2003).
- 37 Cano-Mejia, J. *et al.* Prussian blue nanoparticle-based photothermal therapy combined with checkpoint inhibition for photothermal immunotherapy of neuroblastoma. *Nanomedicine: Nanotechnology, Biology and Medicine* **13**, 771-781 (2017).
- 38 Srinivasan, P., Wu, X., Basu, M., Rossi, C. & Sandler, A. D. PD-L1 checkpoint inhibition and anti-CTLA-4 whole tumor cell vaccination counter adaptive immune resistance: A mouse neuroblastoma model that mimics human disease. *PLoS medicine* **15**, e1002497 (2018).
- 39 Khokhlova, T. D. *et al.* Dependence of boiling histotripsy treatment efficiency on HIFU frequency and focal pressure levels. *Ultrasound in medicine & biology* **43**, 1975-1985 (2017).
- 40 Shen, Z. *et al.* Higher intratumoral infiltrated Foxp3+ Treg numbers and Foxp3+/CD8+ ratio are associated with adverse prognosis in resectable gastric cancer. *Journal of cancer research and clinical oncology* **136**, 1585-1595 (2010).
- 41 Yao, X. *et al.* Levels of peripheral CD4+ FoxP3+ regulatory T cells are negatively associated with clinical response to adoptive immunotherapy of human cancer. *Blood*, blood-2011-2010-386482 (2012).
- 42 Mühlbauer, M. *et al.* PD-L1 is induced in hepatocytes by viral infection and by interferon- α and- γ and mediates T cell apoptosis. *Journal of hepatology* **45**, 520-528 (2006).
- 43 Lina Chakrabarti, C. M., Anthony D. Sandler. Combination of Id2 knockdown whole tumor cells and checkpoint blockade: a potent vaccine strategy in a mouse neuroblastoma model. *PLoS One* **10**, e0129237 (2015).
- 44 Bass, R. *et al.* Oncologic and functional outcome of partial gland ablation with HIFU for localized prostate cancer. *The Journal of urology* (2018).
- 45 Schade, G. R. *et al.* Boiling Histotripsy Ablation of Renal Cell Carcinoma in the Eker Rat Promotes a Systemic Inflammatory Response. *Ultrasound in medicine & biology* (2018).
- 46 Gong, J., Chehraz-Raffle, A., Reddi, S. & Salgia, R. Development of PD-1 and PD-L1 inhibitors as a form of cancer immunotherapy: a comprehensive review of registration trials and future considerations. *Journal for immunotherapy of cancer* **6**, 8 (2018).
- 47 D'andrea, A. *et al.* Interleukin 10 (IL-10) inhibits human lymphocyte interferon gamma-production by suppressing natural killer cell stimulatory factor/IL-12 synthesis in accessory cells. *Journal of Experimental Medicine* **178**, 1041-1048 (1993).
- 48 Strobl, H. & Knapp, W. TGF- β 1 regulation of dendritic cells. *Microbes and Infection* **1**, 1283-1290 (1999).

Chapter 5

- 49 Wheeler, D. S. *et al.* Extracellular Hsp72, an endogenous DAMP, is released by virally infected airway epithelial cells and activates neutrophils via Toll-like receptor (TLR)-4. *Respiratory research* **10**, 31 (2009).
- 50 Narumi, K. *et al.* Proinflammatory proteins S100A8/S100A9 activate NK cells via interaction with RAGE. *The Journal of Immunology*, 1402301 (2015).
- 51 Re, F. & Strominger, J. L. Toll-like receptor 2 (TLR2) and TLR4 differentially activate human dendritic cells. *Journal of Biological Chemistry* **276**, 37692-37699 (2001).
- 52 Hundt, W., O'Connell-Rodwell, C. E., Bednarski, M. D., Steinbach, S. & Guccione, S. In vitro effect of focused ultrasound or thermal stress on HSP70 expression and cell viability in three tumor cell lines. *Academic radiology* **14**, 859-870 (2007).
- 53 Alcón, V. L., Luther, C., Balce, D. & Takei, F. B-cell co-receptor CD72 is expressed on NK cells and inhibits IFN- γ production but not cytotoxicity. *European journal of immunology* **39**, 826-832 (2009).
- 54 Yarmolenko, P. S. *et al.* Technical aspects of osteoid osteoma ablation in children using MR-guided high intensity focussed ultrasound. *International Journal of Hyperthermia* **34**, 49-58 (2018).
- 55 Sharma, K. V. *et al.* Comparison of noninvasive high-intensity focused ultrasound with radiofrequency ablation of osteoid osteoma. *The Journal of pediatrics* **190**, 222-228. e221 (2017).

Chapter 6

Technical aspects of osteoid osteoma ablation in children using MR-guided high intensity focused ultrasound



This chapter is based on:

Pavel S.Yarmolenko, **Avinash Eranki**, Ari Partanen, Haydar Celik, AeRang Kim, Matthew Oetgen, Viktoriya Beskin et al. "Technical aspects of osteoid osteoma ablation in children using MR-guided high intensity focused ultrasound." *International Journal of Hyperthermia* 34, no. 1 (2018): 49-58.

6.1 Abstract

Background: Osteoid osteoma (OO) is a painful bone tumour occurring in children and young adults. Magnetic resonance imaging-guided high intensity focussed ultrasound (MR-HIFU) allows non-invasive treatment without ionising radiation exposure, in contrast to the current standard of care treatment with radiofrequency ablation (RFA). This report describes technical aspects of MR-HIFU ablation in the first 8 paediatric OO patients treated in a safety and feasibility clinical trial (total enrolment of up to 12 patients).

Materials and methods: OO lesions and adjacent periosteum were treated with MR-HIFU ablation in 5–20 sonications (sonication duration $\frac{1}{4}$ 16–48 s, frequency $\frac{1}{4}$ 1.2 MHz, acoustic power $\frac{1}{4}$ 20–160 W). Detailed treatment workflow, patient positioning and coupling strategies, as well as temperature and tissue perfusion changes were summarised and correlated.

Results: MR-HIFU ablation was feasible in all eight cases. Ultrasound standoff pads were shaped to conform to extremity contours providing acoustic coupling and aided patient positioning. The energy delivered was 10 ± 7 kJ per treatment, raising maximum temperature to 83 ± 3 °C. Post ablation contrast-enhanced MRI showed ablated volumes ranging 0.46–19.4 cm³ extending further into bone (7 ± 4 mm) than into soft tissue (4 ± 6 mm, $p \frac{1}{4}$ 0.01, Mann–Whitney). Treatment time ranged 30–86 min for sonication and 160 ± 40 min for anaesthesia. No serious treatment-related adverse events were observed. Complete pain relief with no medication occurred in 7/8 patients within 28 days following treatment.

Conclusions: MR-HIFU ablation of painful OO appears technically feasible in children and it may become a non-invasive and radiation-free alternative for painful OO. Therapy success, efficiency, and applicability may be improved through specialised equipment designed more specifically for extremity bone ablation.

6.2 Introduction

Osteoid Osteoma (OO) is a benign, but painful bone lesion that usually affects children and young adults between 10 and 20 years of age ¹. The most frequent symptom is localized bone pain that worsens at night and is alleviated by nonsteroidal anti-inflammatory drugs (NSAIDs) ². The pain results from prostaglandin release by the OO nidus – a highly vascularized central region often surrounded by a fibrovascular rim and reactive sclerosis ³. Complete and permanent pain resolution can be achieved through destruction of the OO nidus and adjacent periosteal nerves ¹.

Difficulty in intraoperative localization of the OO nidus makes open surgical resection challenging and involves significant bone resection and collateral damage ¹. To address the long hospital stays and recovery times associated with open surgical resection, CT guided-radiofrequency ablation (RFA) has become the standard of care treatment for OO refractory to medical management ^{4,5} over the course of the last two decades. While RFA has very high clinical success rates, it is an invasive procedure, which requires drilling from the skin through soft tissue and bone to burn the OO nidus with a probe. Image guidance with CT also exposes the patient and the physician to ionizing radiation.

Magnetic resonance imaging (MRI)-guided high intensity focused ultrasound (MR-HIFU) may address the inadequacies of open surgery and RFA by providing a completely non-invasive and spatially precise ablation of tissue without ionizing radiation. This therapeutic modality uses detailed anatomical MRI for treatment planning and multi-slice MRI thermometry for real time therapy monitoring and control. Various benign and malignant lesions have been treated with MR-HIFU, including uterine fibroids, prostate, brain and musculoskeletal tumors ⁶. Safety, feasibility, and effectiveness of MR-HIFU ablation of metastatic bone lesions and periosteal nerves to alleviate pain has also been shown ⁷. More recently, MR-HIFU was used by Napoli et al. to treat 29 patients (mean age = 25 ± 16) with painful OO, achieving >90% treatment success with no major treatment-associated adverse events ^{8,9}. Their initial study showed that MR-HIFU ablation of OO was feasible and safe using the InSightec ExAblate MR-HIFU system. Detailed information

Chapter 6

on procedure workflow, patient positioning, imaging and sonication parameters would help guide and develop this application of MR-HIFU.

The present work focuses on the technical aspects of eight MR-HIFU OO ablation treatments performed at our institution through an IRB-approved clinical trial designed to evaluate the safety and feasibility of this therapy in a pediatric cohort, in whom OO is most commonly seen. Our study complements previously published work by examining a younger patient population and using a different clinical MR-HIFU device. Specifically, we report on the procedure workflow, patient positioning and acoustic coupling strategies, MR imaging, and sonication parameters using the Philips Sonalleve V2 clinical system. We also discuss therapy duration, target temperature achieved, thermal dose, and non-perfused volume resulting from the treatment.

6.3 Methods & Materials

6.3.1 Patients

Eight patients with radiologically confirmed diagnosis of OO were treated on a prospective clinical trial of MR-HIFU ablation of OO in children and young adults, with a total planned enrolment of up to 12 patients (NCT02349971, [10]). All patients enrolled in this trial received treatment after providing a written informed consent, and all procedures were approved by the Children's National Health System institutional review board.

6.3.2 MR imaging

A clinical MRI scanner (Achieva 1.5 T, Philips, Best, Netherlands) was used in conjunction with other MR-HIFU system components for pre-treatment imaging, real-time guidance, and post-treatment assessment (Table 1), as briefly summarised below.

Following generic survey and reference scans, a high-resolution 3D dataset was examined to ensure that no air bubbles were present on the patient's skin in the likely HIFU beam path. For treatment planning, both T1- and T2-weighted 3D datasets were acquired to ensure sufficient

contrast and visibility of the small OO nidus, neurovascular bundles and other surrounding anatomy.

Real-time MRI thermometry was performed using the pro-ton resonance frequency shift (PRFS) method [11]. A near-field imaging slice was positioned in the plane that is approximately perpendicular to the HIFU beam, capturing either muscle adjacent to the fat or gel pad next to the skin if muscle thickness was insufficient (<7 mm).

Post-treatment MR imaging began 3 min after the last sonication ended to limit the effect of heat on tissue T1 and T2 values. The same T1- and T2-weighted scans were repeated after therapy and followed by manual infusion (1–2 ml/s) of MRI contrast agent (DotaremVR, 0.1 mmol/kg (0.2 ml/kg), Guerbet LLC, Bloomington, IN) and 5 ml saline flush. The T1-weighted scan was then repeated again.

6.3.3 MR-HIFU treatment

A clinical MR-HIFU system (Sonalleve V2, Philips, Vantaa, Finland) was used to thermally ablate the OO nidus and adjacent periosteal nerves, as summarised briefly below and in Figure 1. Six of the eight treated patients were positioned on the HIFU tabletop prior to induction of anaesthesia to acquire initial images used to pre-plan the treatment and to select a comfortable patient and target limb position with the aid of patient feedback and appropriate cushioning. Following onset of general anaesthesia, the patients were positioned on the MR-HIFU table. Planning image sets were acquired, followed by OO ablation and post-treatment contrast enhanced imaging. Further details on the equipment and details of the procedure are provided in “Supplemental Materials and Methods”.

6.3.4 Technical feasibility assessment

Technical feasibility was assessed using pre-treatment imaging and confirmed when appropriate patient positioning and ablation were completed on treatment day. Treatment was considered “feasible” if the patient was successfully positioned in a way that allowed for treatment without

Table 1. Overview of MRI sequences used for MR-HIFU treatment of OO. Field of view (FOV) for the real-time MR thermometry sequence was standardised at 400 # 400 mm, with three orthogonal slices intersecting at the current focus and one slice manually placed to monitor near field temperature. For all other scans, FOV and number of slices were minimised to conform to anatomy and minimise acquisition time.

MRI sequences and their purpose	Type	TR (ms)	TE (ms)	FA (°)	NSA	Voxel Size (mm)	Slices	Duration (min:s)
Survey – target localization	2D TFE	11.0	6.9	25	2	0.74 x 0.74 x 10	16	1:27
Reference – coil calibration	Reference							1:08
Air bubble detection – skin protection	3D FFE	15.0	12.0	10	2	1.1 x 1.1 x 2.0	Varied	< 4min
T2w – treatment planning and evaluation	3D TSE	1400	186	90	2	1.3 x 1.3 x 2.6	Varied	< 4 min
T1w scans – therapy planning and evaluation (pre- and post-treatment and post-contrast)	3D FFE	6.4	3.1	10	2	1.3 x 1.3 x 2.6	Varied	1:55 – 6:30
MR thermometry – treatment monitoring and control	2D FFE	54	30	19	1	2.5 x 2.5 x 7.0	4	0:3.7 dynamic

Technical aspects of Osteoid Osteoma treatment with HIFU

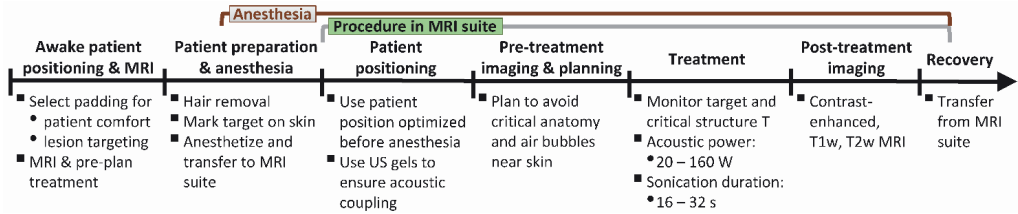


Figure 1. Overview of treatment workflow for osteoid osteoma ablation with MR-HIFU.

Table 2. Summary of patient and lesion characteristics. Reported periosteal thickness and nidus dimensions were calculated from CT images prior to treatment, with no significant differences compared to MRI ($p > 0.57$, t test).

	Mean \pm SD	(median, range)
Patients:		
Age (years)	15.8 \pm 5.9	(16.5, 7 – 24)
Sex (# male / # female)	6 / 2	
Weight (kg)	57 \pm 20	(65.2, 25.2 – 75.2)
Height (cm)	161 \pm 19	(167.5, 120 – 177)
BMI	21 \pm 4	(21.2, 14.4 – 27.3)
Lesions:		
Skin-to-bone distance at target lesion (mm)	32 \pm 16	(31.9, 16 – 60)
Periosteal thickness at target lesion (mm)	4 \pm 5	(2.5, 0 – 14)
OO nidus volume (mm ³)	1.0 \pm 0.6	(0.82, 0.4 – 2.5)
Lesion location	Femur: 3; Tibia: 3; Hallux: 1; Talus: 1	

6.4 Results

Patient and lesion characteristics

Patient demographics and disease location are described in Table 2. Six of the eight treated patients were below 18 years of age, and two were in their early twenties. All but one of the patients was 145–170 cm tall. There was a large range of lesion depths and periosteum thickness.

6.4.1 Technical feasibility

Patient positioning on the HIFU table and subsequent treatment were feasible in all 8 cases, with OO locations in the tibia ($n = 3$), femur ($n = 3$), talus ($n = 1$), and hallux ($n = 1$). Below, we describe patient support and ultrasound coupling strategies, and provide technical details that characterize feasibility of OO ablation with MR-HIFU.

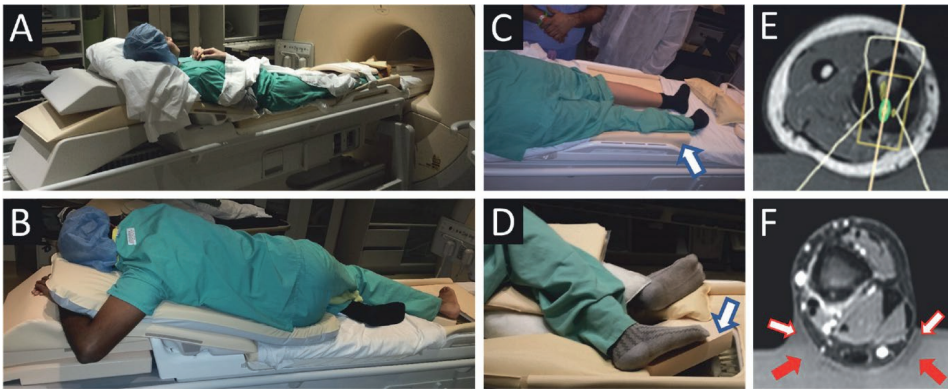


Figure 2. Patient positioning and ultrasound coupling for extremity OO treatments. Patient positioning was feasible in all eight patients. A&B: extension of the HIFU table was necessary to support the upper body during lower extremity treatment. C&D: pre-treatment positioning helped identify pressure spots, enabled pre-planning of sonications, and provided guidance for patient positioning. Yellow padding 4 cm in thickness (C&D, hollow blue arrows) was used in place of gel in pre-anesthesia patient positioning. E&F: modifying ultrasound coupling gel to ensure HIFU coupling free of air-water interfaces. Note that the outline of the HIFU beam passes directly into the limb while avoiding air through either (E) conformably carved gel pad, or (F) wedge-shaped gel pads (solid red arrows) placed on both sides of the limb, with 1:2 ultrasound imaging gel:water dilution creating continuous coupling (hollow red/white arrows).

6.4.2 Patient positioning

The patient height and weight ranged 120 – 177 cm and 25.2 – 75.2 kg respectively, requiring variable amounts of padding and support. To provide upper-body support for taller patients, we used additional hard foam positioning aids and soft foam padding, effectively extending the length

of the MR-HIFU table by as much as 50 cm (Figure 2A&B). Pre-treatment positioning of six of the eight patients while awake, prior to anesthesia was useful in identifying several patient-table contact points (especially around the edge of the HIFU tabletop acoustic window) that became uncomfortable or painful without extra padding. Patient feedback revealed that softer foam padding was necessary between the patient's body and the top pelvic MR imaging coil that was tightened against the patient's body with Velcro straps. Despite the preparatory positioning prior to anesthesia, three of the patients exhibited mild discomfort and pain at contact points of their body with the edge of the HIFU window (outside of the treatment area) with scarce padding. The discomfort resolved without treatment over the course of the first week following therapy.

6.4.3 Ultrasound coupling

Gel pads in combination with diluted diagnostic ultrasound gel successfully provided acoustic coupling and lethal thermal doses were not detected in the vicinity of the skin in treated patients. Two of the cases required a carved gel pad to better conform to the limb and to support it, providing enough gel-skin contact area to fit the HIFU beam and avoid reflection and off-target heating associated with air-water interfaces. The need for such modifications was most apparent in areas where the axial limb cross-section was small relative to the HIFU beam (Figure 1E&F).

6.4.4 Duration of the procedure and its components

Pre-treatment patient positioning and imaging was performed prior to anesthesia for six of the eight treated patients, lasting 20 – 40 min. Such pre-treatment positioning and imaging was deemed unnecessary for the remaining two patients whose lesions were similar in appearance and location to previously completed treatments. Once anesthetized and brought into the MRI suite, patient positioning duration hovered around its average of 28 ± 14 min for most patients, though for the first patient it was prolonged by the need to cut the stand-off pad to better fit the anatomy and the need to re-position the patient due to the presence of air bubbles (Figure 2B).

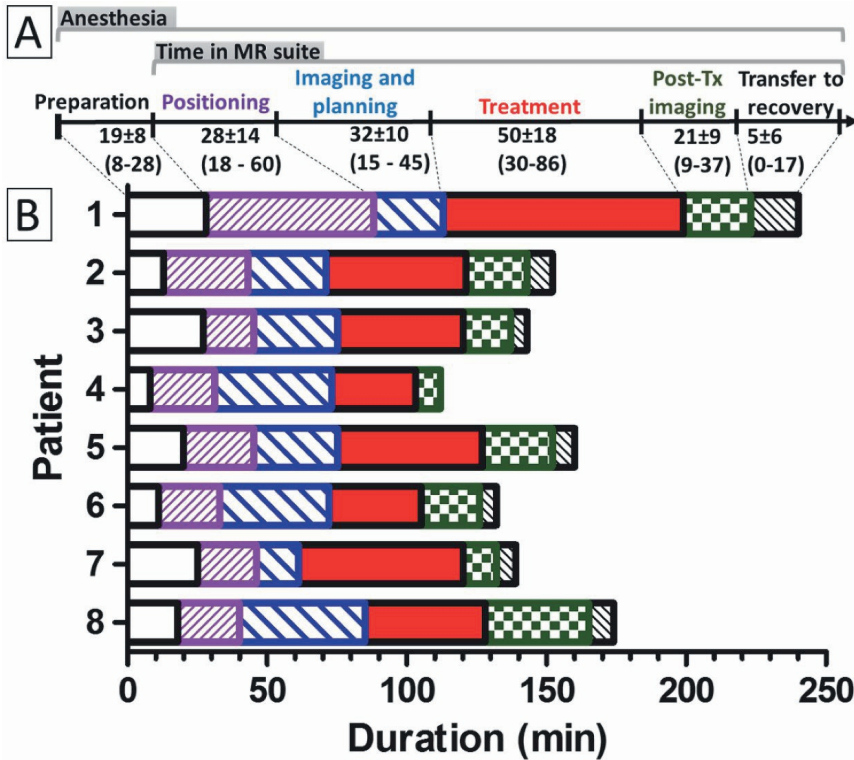
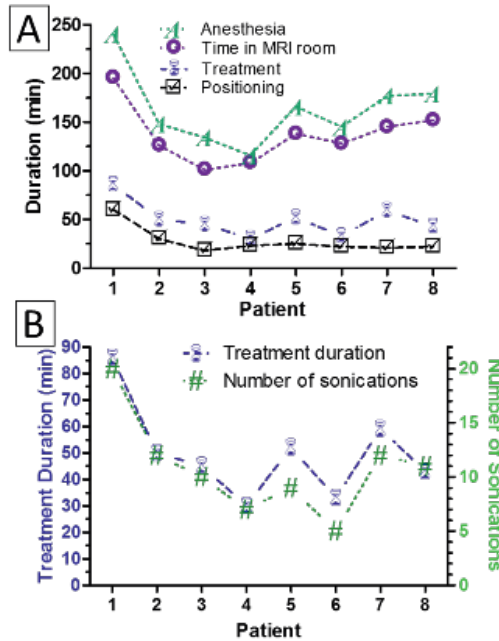


Figure 3. Duration of treatment and its individual components. A: Treatment workflow with average duration of each workflow component. B: Relative lengths of all treatment sub-components. 'Preparation' included pre-treatment induction of anesthesia and/or sedation, cleaning and hair removal from the skin at the treatment site as well as pre-treatment movement of the patient into the MRI suite. The duration of "Transfer to recovery" was set to 0 for patient 4, as this patient was not intubated.

For all patients, treatment planning began immediately after the first planning image set was acquired and sent to the HIFU Therapy Planning Console (<8 min into acquisition of pre-treatment MRI). Time spent on acquiring planning image datasets varied by as much as 30 min (Figure 2A) due to the difference in size of the targeted periosteum, proximity to critical structures and other factors, such as operator experience. Required MRI suite time decreased, as did the various

components of the procedure, especially after the first patient due to growing experience (Supplemental Figure 1A&B and Figure 3). Total MRI suite time averaged 140 ± 30 min. Total anesthesia time was, on average, 20 min longer (160 ± 40 min), as it included patient transfer to and from the MRI suite, intubation and extubation.



Supplemental Figure 1. Comparing durations of treatment components. A: Key MR-HIFU workflow component durations. B: Treatment duration closely tracks and correlates with the number of sonications per treatment (Spearman $r = 0.79$, $p = 0.0279$). Treatment duration includes therapy sonications and the cooling periods following these sonications (test sonications were not counted). Note that duration of treatment was <50% of the total MRI room time for all patients, with the difference attributable to imaging and treatment planning.

A cooling period followed each sonication, and while duration of individual sonications ranged 16 – 36 s, the cooling period was >3 min for most sonications. Including cool-down times, 5 – 20 sonications took 30 – 86 min, though only 3.4 ± 1.4 min of this time was spent on sonications

Chapter 6

(‘Effective sonication time’, Table) across all treatments. The rest of the treatment time was used for cooling between sonications and planning subsequent target locations. Treatment duration closely tracked and significantly correlated with the number of sonications (Spearman $r = 0.79$, $p = 0.0279$, Supplemental Figure 1B), meaning that the use of fewer, higher power sonications generally decreased treatment time.

The most time-consuming single component of the procedure were sonications, for most patients (Figure 2). However, all preparatory procedures taken together (Preparation, Positioning, as well as Imaging and Planning) were of comparable duration to the 30 – 86 min spent on treatment itself.

Table 3. Summary of sonication duration and power, as well as the resulting temperature and tissue perfusion changes. **Volume of lethal thermal dose was defined at one target location, whereas sonications at several target locations contributed to the total NPV volume.

	Mean \pm SD (median, range)	
Duration		
Number of therapy sonications	11 \pm 4	(11, 5 – 20)
Effective sonication time (min)	3.4 \pm 1.4	(3.2, 1.6 – 5.7)
Duration of one sonication (s)	18 \pm 5	(16, 16 – 36)
Duration of one sonication + cooling (min)	4.1 \pm 0.5	(3.9, 3.5 – 4.7)
Total treatment duration (min)	49 \pm 18	(47.5, 30 – 86)
Power and energy		
Sonication power (W)	50 \pm 30	(50, 15 – 160)
Total therapy energy (kJ)	10 \pm 7	(9.48, 2.1 – 24.1)
Energy/sonication (J)	970 \pm 700	(800, 240 – 3200)
Temperature and ablation		
Maximum temperature ($^{\circ}$ C)	83 \pm 3	(83.7, 77 – 87)
Volume of lethal thermal dose (cm ³)**	1.4 \pm 1.1	(1.23, 0.18 – 3.85)
NPV volume (cm ³)**	5 \pm 6	(2.2, 0.46 – 19.4)
NPV extent into soft tissue (mm)	5 \pm 6	(3.1, 1.0 – 19.1)
NPV extent into bone (mm)	9 \pm 3	(6.9, 5.5 – 14.9)

6.4.5 Thermometry, energy and spatial definition of target

The depth of the targeted OO nidus center from skin surface ranged 1.1 – 7.7 cm and all lesions were targetable with HIFU. Thick neocortex was encountered in two cases: one in femur and one in tibia (up to ~12 mm thickening), requiring a higher number of sonications of greater power and duration. Sonications resulted in highest temperatures and near-instantaneous ablation (>60°C) at the bone surface, with lethal thermal dose delivered to the adjacent soft tissue as well as bone, according to MR thermometry measurements (Figure & Figure).

MRI thermometry was used to monitor sonication progress in real time, while contrast-enhanced MRI allowed post-treatment assessment. Using NPV as an indicator of the ablated zone, the ablated region extended more into the bone than into soft tissue ($p = 0.01$, Mann Whitney). No significant correlation was found (Spearman $r = -0.43$, $p = 0.35$) between extent of ablation into the bone and its extent into adjacent soft tissue.

Estimated NPV was $5 \pm 6 \text{ cm}^3$, which was several fold greater than the $1.4 \pm 1.1 \text{ cm}^3$ estimate of a volume that achieved lethal thermal dose at one target location (Table). This discrepancy between NPV and lethal thermal dose volume is at least in part due to NPV incorporating the effects of 5 – 20 therapy sonications at 2 – 6 locations, while thermal dose was estimated at each location separately.

Acoustic power averaged $50 \pm 30 \text{ W}$ and total energy deposition, including all therapeutic sonications, averaged $10 \pm 7 \text{ kJ}$ across all eight patients, ranging widely (2.1 – 24.1 kJ, Table). Energy prescribed in individual therapeutic sonications varied widely as well, ranging 240 – 3200 J. Total treatment energy correlated significantly with the resulting NPV volume (Spearman $r = 0.952$, $p=0.001$). Energy used at each location did not correlate with the volume that achieved lethal thermal dose based on MRI thermometry (Spearman $r=0.260$, $p=0.22$).

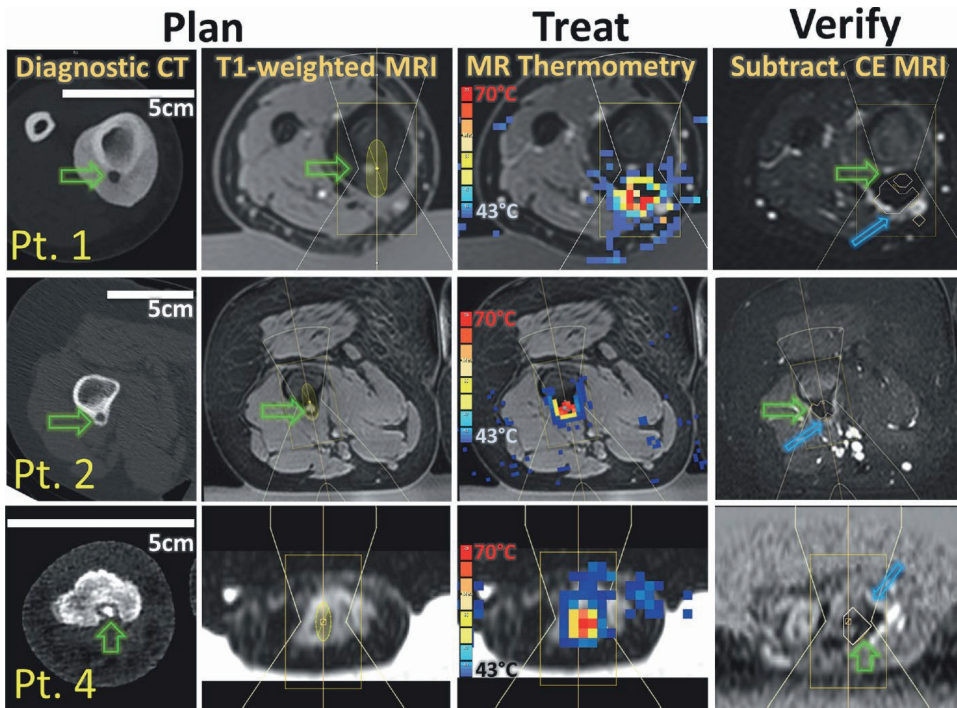


Figure 4. MR-HIFU ablation of osteoid osteoma: from diagnosis to post-treatment imaging. Patients 1, 2 and 4 had lesions in the tibia, the femur, and the hallux, respectively. Treatment Planning: Pre-procedure planning was performed using available diagnostic CT and MRI imaging. Note that the length of the 5-cm scale bar differs among patients, highlighting the size difference between the targeted limbs. Green arrows indicate the location of OO nidus. Pre-treatment T1-weighted high-resolution MRI dataset was used sonication cell size, orientation and location in the treatment area during treatment planning. MRI thermometry allowed for monitoring of heating during treatment (temperature at the end of sonication is shown with color bars ranging from 43 °C to 70 °C). Resulting lack of perfusion was evaluated using a subtraction image of MRI contrast enhancement. Blue arrows mark edema immediately after treatment.

6.4.6 Near field heating/cooling

Delineation of potentially vulnerable areas prior to treatment allowed close monitoring of their temperature and thermal dose during treatment in all imaged planes. However, some of the

targeted lesions had little tissue other than subcutaneous fat between the targeted lesion and the gel pad, making PRFS-based MRI thermometry impossible or difficult between the gel pad and the target. If no vulnerable structures were in the vicinity and insufficient thickness of muscle tissue precluded real-time temperature mapping in the near field, then sufficient MRI thermometry data for treatment monitoring was obtained using a slice in the gel pad that was parallel and adjacent to the skin in the HIFU beam path (Figure 2A).

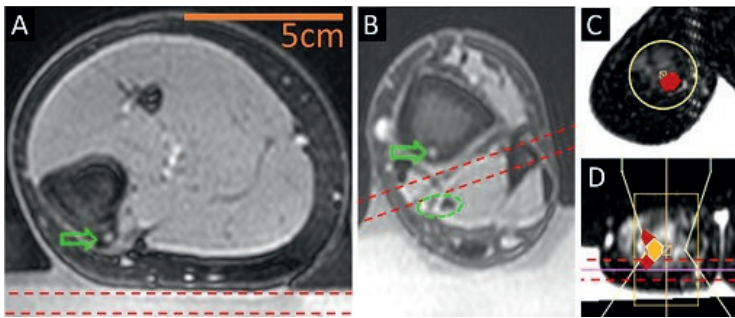


Figure 5. Estimation of near field heating and ensuring treatment safety. Bounds of an imaging slice (7 mm thick) dedicated to near field temperature monitoring are depicted using dashed lines. Green arrows indicate the location of OO nidus and a green dashed oval marks a neurovascular bundle that must be spared from ablation. A: Positioning a slice dedicated to near field temperature monitoring may not be possible in the muscle and skin temperature may be approximated at the gel-skin interface (OO in tibia, Patient 7). B: Near field monitoring slice may be placed between the targeted bone surface and a critical structure to ensure its safety (tibia, Patient 8). C: Near field image through muscle and fat in the OO vicinity (hallux, Patient 4). D: Orthogonal T1-weighted images show that monitoring of near-field temperature in the hallux. The HIFU beam is outlined along with areas of sub-lethal thermal effect (filled in red in C and D) and lethal thermal effect (white borders and yellow fill in D).

Chapter 6

Several patients had neurovascular tissue that needed to be spared nearby (Figure 5B). In such cases, MRI thermometry was performed on a slice in close proximity to the vulnerable structure, between the bone and the vulnerable structure. For one of the patients, near field MRI thermometry was performed 2.5 mm from the heated bone surface. This location was chosen in favor of placing the near field slice in the gel due to the signal being sufficient for MRI thermometry and due to the very shallow location of the OO nidus relative to the bone surface. At this location, the maximum cumulative thermal dose reached 300 CEM43 adjacent to the targeted region (Figure, Patient 4 and 6C&D). This thermal dose would be lethal in affected tissues ¹⁰. However, this thermal dose in only a few voxels of the near field monitoring slice. Furthermore, the imaging slices through the center of the HIFU beam indicated that these elevations in temperature were localized and would not affect the skin (Figure, Patient 3, third column), and therefore the procedure was completed despite the relatively high thermal dose in near field monitoring slice. As a result, no skin damage was observed. In all remaining patients, maximum temperature in the near field monitoring slices remained <50 °C, resulting in sub-lethal thermal doses (<10.5 CEM43), known to have only mild functional effects in tissue, if any ¹⁰.

4 mm, 16 s sonication, 160 W

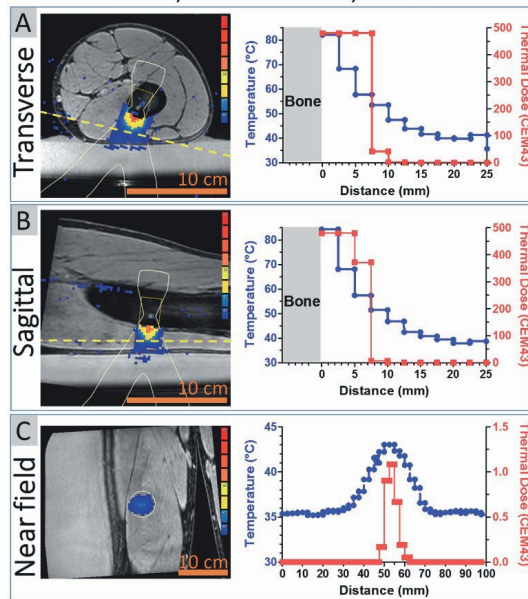


Figure 6. Heat distribution in muscle adjacent to neocortex at the end of sonication. The 4 mm target was sonicated at the maximum power available under our protocol for this cell size, producing 2560 J. Panels A, B, and C represent the three slices monitored with real-time MRI thermometry (blue-to-red color map), overlaid on corresponding magnitude images (grayscale) from a T1w planning scan with fat saturation. The near field slice (C) was positioned in the muscle, ~1.5 cm from the bone surface (yellow dashed line in sagittal and transverse slices). A&B: temperature and thermal dose vs. distance from the bone along the center of HIFU beam. C: Temperature and thermal dose profiles in the cross-section of the HIFU beam that intersects the near field MRI slice location (white oval in the image indicates the intersection).

6.4.7 Treatment safety and imaging findings

All patients were monitored for up to four hours after recovery from anesthesia/sedation and returned to their daily activities the following day. Close follow up over four weeks after treatment showed that these treatments were safe, causing no reportable treatment-related adverse events. For seven of the eight patients, complete or nearly complete resolution of OO-related pain

Chapter 6

followed within days and all but one patient were able to cease medication use 28 days following treatment.

Although temperature changes within the nidus could not be visualized during the sonications due to relatively low signal there, contrast-enhanced MRI performed immediately after ablation showed complete lack of enhancement (i.e. perfusion) of the OO nidus in six of eight patients, and partial nidus enhancement in two patients. In addition, these scans showed that NPV extended 1.4- to 12-fold deeper into bone than into soft tissue for all but one patient, whose NPV extended ~30% farther into soft tissue than into bone (9 ± 3 mm vs. 5 ± 6 mm, $p=0.01$, Mann Whitney).

6.5 Discussion

To highlight specific technical aspects relevant to MR-HIFU OO ablation in a young patient cohort, the following discussion compares and contrasts our experience to other recently published work. Among the most relevant, are the published experiences with MR-HIFU of OO in older patients using a different commercial clinical system and MR-HIFU ablation of painful bone metastatic cancer and larger soft tissue tumors.

6.5.1 Technical feasibility

All eight MR-HIFU ablation procedures were technically feasible with regard to successful patient positioning and coupling, treatment planning, sonication under real-time MRI monitoring and post-treatment visualization of the ablated target. Technical feasibility and treatment safety are both largely dependent on device design, treatment workflow and patient/lesion characteristics. In the case of OO, the bone lesions are relatively small and they are most commonly located in the extremities. This aspect required positioning aides and patient-specific positioning strategies to enable therapy for all eight patients. In the eight OO cases, a small number of sonications was sufficient to achieve lethal thermal dose around the periphery of the bone and cessation of perfusion in the neocortex surrounding the OO nidus and the nidus itself. While the tabletop-

integrated MR-HIFU design may be further tailored for OO treatment, its current design is capable of safely ablating OO.

6.5.2 Design of MR-HIFU: tabletop

In terms of geometric accessibility, the treated lesions were reached with either the focal point or the broad portion of the MR-HIFU beam as planned, and in this respect, tabletop and transducer positioning system provided sufficient lesion access. There is room for clinical MR-HIFU equipment optimization to accommodate ablation of bony lesions, especially in extremities. This device was originally designed for uterine fibroid ablation in adult patients positioned in prone position. For those patients, a large acoustic window at the center of the HIFU table allowed for ideal patient position to center the mid abdomen on the treatment window. The range of transducer motion was sufficient to target relatively large masses of soft tissue deep in the lower abdomen. In contrast to uterine fibroids, OO are small bone lesions that are most commonly found in extremities and at variable depths from the skin. These differences often necessitate centering patients at one of the ends of the MR-HIFU table and using a custom table extension (Figure 2 A & B). The need for such extensions has not been directly addressed by other groups that have performed MR-HIFU ablations in extremities, and our experience indicates that manufacturers should expand the variety of available shapes and sizes of table extensions to accommodate extremity treatments. Rotation and bending of the extremity that was required to center the lesion in the middle of the treatment window may not always be feasible. These difficulties may be addressed with a transducer that can be positioned manually over the target region. The use of these new systems for extremity sonications is currently under investigation.

Design of MR-HIFU: acoustic coupling and skin protection

Possibility of skin and other off-target tissue burns is a potential risk during MR-HIFU ablation. Skin burns may arise from inadequate acoustic coupling leading to air bubbles in the acoustic beam path as well as off-target heating in tissues adjacent to skin. Acoustic coupling to the skin

Chapter 6

was achieved using a combination of liquid and solid ultrasound gel (Figure 2 E&F). Air bubbles in the skin-gel interface were easily visible using an MRI sequence optimized for this purpose (Table 1). The risk of heat accumulation in off-target tissues is largely avoided by using “cooling periods” after each sonication that allow skin and other intervening tissues to cool. However, this safety measure noticeably impacts treatment time. Including the 3-min cooling periods between each sonication, the total sonication time per patient was 48 ± 15 min – more than 14 times greater than the time required for the actual sonications. Napoli et al. also reported that “effective treatment time” was several times shorter than “total length of treatment”. Reducing or eliminating cooling periods between sonications could potentially cut treatment duration by as much as an order of magnitude, which is especially relevant in younger patients, all of whom require anesthesia and sedation. This could be achieved by applying an initially acquired baseline scan to all sonications and ensuring adequate correction for magnetic drift, as recent work demonstrates. For example, an early implementation of some of these changes allowed for treatment of large uterine fibroids.

The concern over skin heating is further exacerbated by a lack of reliable real-time skin temperature measurement that would adequately capture the entire area at risk of off-target ablation. At best, MRI provides only a qualitative measurement of skin temperature, which cannot be obtained in real time¹¹. Patients undergoing OO ablation must remain sedated during the procedure, and therefore the risk of skin damage may be greater during OO ablation than with uterine fibroid ablation, where the patients were awake during all procedures and could respond to pain. Our experience thus far suggests that real-time MRI thermometry both in muscle and in the gel adjacent to the skin provided useful information on skin temperature. In absence of a robust real-time skin temperature measurement, and lacking feedback from sedated patients, we employed both direct cooling of the skin (gel pads were cooled to 4 °C prior to the procedure) and standard cooling periods of 3 min to minimize the possibility of skin damage. Altogether, these

precautions were effective, and no skin burns were detected in our clinical trial, even in cases of lesions located close to 1 cm from the skin.

In terms of geometric accessibility, the treated lesions were reached with either the focal point or the broad portion of the MR-HIFU beam as planned, and in this respect, tabletop and transducer positioning system provided sufficient lesion access. However, deep lesions that were shielded by thick cortex required treatment at the limits of the power and duration settings allowed for our clinical trial, suggesting that relaxing the software-imposed limits could help quicker treatment OO lesions with a thicker overlying cortex.

6.5.2 Choice of sonication power and duration

Precise ablation of small bony lesions with MR-HIFU can be leveraged only in lesions near the bone surface due to the high attenuation of ultrasound by bone. Thus, depth of neocortex over the targeted nidus relative to the skin is important for selecting sonication power and duration. In our patients, the nidus was 4 ± 5 mm beyond the surface of the neocortex and/or cortical bone. Heating within the bone occurs in large part via heat conduction from the cortex surface at the frequencies used in current clinical MR-HIFU devices (1.2 MHz herein). Practically, this means that the treatable depth beyond the surface of the bone cortex is limited by the extent of acceptable ablation of soft tissues adjacent to the bone. Our data demonstrate that the extent of ablation is significantly greater in the bone than in soft tissue (Table). If this preferential targeting of bone continues to hold true in subsequent treatments, its generalization may allow the treatment to be more closer to the skin and neurovascular tissues and treatment of OO nidus deeper under the surface of the bone. Use of computer simulations that incorporate tissue attenuation and geometry of prospective patients has the potential to further reduce overall treatment time and improve the safety of the procedure by providing the clinical team with initial sonication parameter values.

Chapter 6

Ultrasound energy is both attenuated and reflected by tissues between the transducer and the target. The targeted cortex of the OO lesions in our clinical trial was at an average depth of 3.2 ± 1.6 cm relative to the skin. The lesions appear similar to those treated in a recent trial of an older patient cohort by Geiger et al. and Napoli et al.^{8,9}. While they used an MR-HIFU by a different manufacturer, the sonication methodology relied on similar sonication durations (~ 22 s vs. 18 ± 5 s we used). Average sonication energy was also similar to our trial, albeit slightly greater (1180 ± 736 J compared to our 968 ± 700 J). Our approach included the use of a greater number of sonications overall, however (11 ± 4), whereas Geiger et al. used only 7 ± 3 sonications. Growing experience allowed sonication power to be increased more rapidly following initial test sonications, thus allowing us to decrease the overall number of sonications, reducing treatment duration in subsequent patients (Figure).

Due to the differences in lesion size and composition, ablation of OO is not easy to relate to earlier clinical trials of metastatic bone cancer or soft tissue lesions, such as uterine fibroids. OO lesions are much smaller than the malignant tumors reported to have been treated with MR-HIFU (median and range were 0.82 ($0.4 - 2.4$) cm^3 herein compared to a median and range of 75.4 ($0.4 - 1341$) cm^3 in metastatic disease¹² and several hundred cm^3 for uterine fibroids¹³). While the depth of bony metastases treated with MR-HIFU is not readily available, their primarily pelvic location¹² suggests that they are deeper than the typical OO lesions we have treated. The lesions we report on are also more shallow compared to the deeper sonications performed in uterine fibroids (6.8 ± 0.5 cm¹³). Many of the sonication parameters and approaches differ among these applications, and thus far, published reports show that large and deep soft tissue targets such as uterine fibroids are best treated with high-energy sonications at around 1 MHz¹³. In the case of bone targets, sonication power may be lower due to the ~ 50 -fold greater absorbance of ultrasound energy by cortical bone in the therapeutic frequency range available¹⁴. Larger bony lesions require more sonications at more distinct locations^{14,15}, which requires longer sonication times than the smaller OO lesions described herein. In contrast, OO may be targeted with only a few

high-energy sonications that cover the OO nidus and adjacent periosteum, with little risk to intervening tissues.

6.5.3 Initial safety findings and future directions

Since MR-HIFU ablation required anesthesia/sedation in all younger patients, strategies that reduce or limit total procedure duration are important. In this regard, positioning and scanning patients on the MR-HIFU table prior to induction of anesthesia/sedation was helpful for several reasons: 1) it allowed us to elicit patient feedback regarding areas of focal pressure and discomfort while the limb was positioned for treatment and decreased the likelihood of post-procedure pain and bruising due to inadequate padding on the MR-HIFU table, 2) it allowed us to ensure that selected MRI sequences optimally demonstrated the lesion and that it could be centered within the allowable treatment volume, and 3) it allowed us to confirm that the limb positioning required for coupling and lesion accessibility to the HIFU beam path was achievable. This cannot always be accurately predicted from diagnostic images which are obtained in standard axial, sagittal, and coronal anatomic planes rather than the position required for treatment. Thus, pre-positioning affords time for evaluation, discussion, and adjustment of patient position by the HIFU treatment team and prevents unnecessary anesthesia/sedation time. Similar pre-positioning steps were also used by other research groups in ablation of metastatic bone lesions with MR-HIFU ¹⁵.

In addition to development of MR-HIFU systems specifically designed for bone ablation, several improvements to the current tabletop-integrated systems have the potential to impact treatment quality. Overall treatment duration may be further improved with availability of HIFU-compatible MRI coils specifically designed for extremity imaging, which could allow 3D MR thermometry as well as reliable measurements of temperature in less vascularized regions such as the OO nidus. Software-based prediction of target and near field tissue cooling rate, and the use of a single baseline for more than one sonication could allow for the cooling time between sonications to be reduced or eliminated, reducing the total treatment time.

6.6 Conclusion

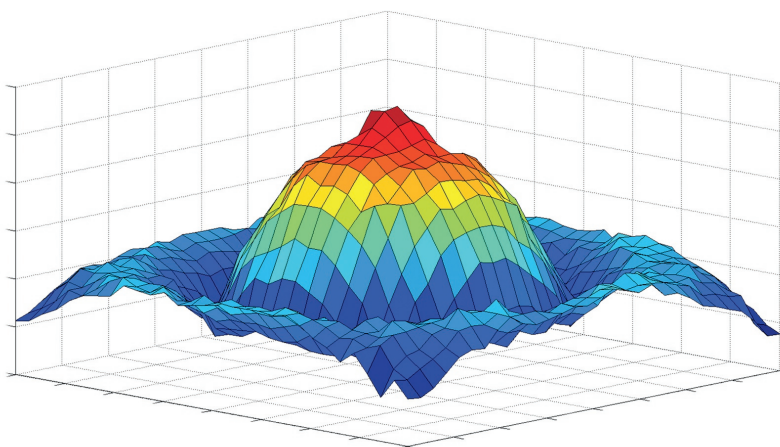
MR-HIFU ablation of OO in children and young adults was feasible and safe, without any serious treatment-attributable adverse events in 8 patients. There was a learning curve in all aspects of this procedure, ranging from patient positioning to selection of optimal sonication parameters to reduction of procedure duration. The data reported here provide technical guidance to teams and centers that are performing these novel treatments, potentially improving patient selection as well as treatment workflow and quality. There are opportunities to improve design of MR-HIFU hardware and software to optimize OO treatment. Such improvements may allow for treatment of lesions located deeper within bone as well as to improve real-time imaging feedback showing the extent of ablation during the procedure.

6.7 References

- 1 Atesok, K. I., Alman, B. A., Schemitsch, E. H., Peyser, A. & Mankin, H. Osteoid osteoma and osteoblastoma. *The Journal of the American Academy of Orthopaedic Surgeons* **19**, 678-689 (2011).
- 2 Peterson, J. J., Fenton, D. S., Czervionke, L. F., Education, M. F. f. M. & Research. *Image-guided Musculoskeletal Intervention*. (Saunders / Elsevier, 2008).
- 3 Cantwell, C. P., Obyrne, J. & Eustace, S. Current trends in treatment of osteoid osteoma with an emphasis on radiofrequency ablation. *European radiology* **14**, 607-617, doi:10.1007/s00330-003-2171-6 (2004).
- 4 Rosenthal, D. I., Hornicek, F. J., Torriani, M., Gebhardt, M. C. & Mankin, H. J. Osteoid osteoma: percutaneous treatment with radiofrequency energy. *Radiology* **229**, 171-175, doi:10.1148/radiol.2291021053 (2003).
- 5 Bruners, P., Penzkofer, T., Gunther, R. W. & Mahnken, A. [Percutaneous radiofrequency ablation of osteoid osteomas: technique and results]. *Rofa* **181**, 740-747, doi:10.1055/s-0028-1109424 (2009).
- 6 Hsiao, Y. H., Kuo, S. J., Tsai, H. D., Chou, M. C. & Yeh, G. P. Clinical Application of High-intensity Focused Ultrasound in Cancer Therapy. *J Cancer* **7**, 225-231, doi:10.7150/jca.13906 (2016).
- 7 Liberman, B. *et al.* Pain palliation in patients with bone metastases using MR-guided focused ultrasound surgery: a multicenter study. *Ann Surg Oncol* **16**, 140-146, doi:10.1245/s10434-008-0011-2 (2009).
- 8 Napoli, A. *et al.* Osteoid osteoma: MR-guided focused ultrasound for entirely noninvasive treatment. *Radiology* **267**, 514-521, doi:10.1148/radiol.13120873 (2013).
- 9 Geiger, D. *et al.* MR-guided focused ultrasound (MRgFUS) ablation for the treatment of nonspinal osteoid osteoma: a prospective multicenter evaluation. *The Journal of bone and joint surgery. American volume* **96**, 743-751, doi:10.2106/JBJS.M.00903 (2014).
- 10 Yarmolenko, P. S. *et al.* Thresholds for thermal damage to normal tissues: an update. *Int J Hyperthermia* **27**, 320-343, doi:10.3109/02656736.2010.534527 (2011).
- 11 Rieke, V. & Butts Pauly, K. MR thermometry. *J Magn Reson Imaging* **27**, 376-390, doi:10.1002/jmri.21265 (2008).
- 12 Hurwitz, M. D. *et al.* Magnetic resonance-guided focused ultrasound for patients with painful bone metastases: phase III trial results. *J Natl Cancer Inst* **106**, doi:10.1093/jnci/dju082 (2014).
- 13 Kim, Y. S. *et al.* Volumetric MR-HIFU ablation of uterine fibroids: role of treatment cell size in the improvement of energy efficiency. *Eur J Radiol* **81**, 3652-3659, doi:10.1016/j.ejrad.2011.09.005 (2012).
- 14 Huisman, M. *et al.* Feasibility of volumetric MRI-guided high intensity focused ultrasound (MR-HIFU) for painful bone metastases. *J Ther Ultrasound* **2**, 16, doi:10.1186/2050-5736-2-16 (2014).
- 15 Napoli, A. *et al.* MR imaging-guided focused ultrasound for treatment of bone metastasis. *Radiographics* **33**, 1555-1568, doi:10.1148/rg.336125162 (2013).

Chapter 7

Summary and General Discussion



Chapter 7

The goal of this dissertation was to develop, and characterize the BH parameter space using a clinical MR-HIFU system, for treating pediatric solid tumors. In addition, the goal was to study the immune-related effects of BH alone and in combination with immunotherapy in an established, large and refractory murine model of neuroblastoma. This work included a detailed acoustic and *in vitro*/tissue-mimicking phantom characterization of HIFU pulsing parameters that can produce BH effects on a clinical MR-HIFU system. This was further extended to study tissue structure and viability using these pulsing parameters in *ex vivo* liver, kidney and cardiac muscle tissues. Further, we selected a BH sonication parameter set, which was able to produce a consistent tissue fractionation, with spatially sharp boundaries, with minimal temperature effects. These parameters were used to study the immune effects *in vivo* using an established, large and refractory murine model of neuroblastoma. While using MRI guidance provides valuable thermometry information, it could also be challenging for most clinical and research sites to acquire a MR-HIFU system. In an effort to further translate this work using an ultrasound-guided HIFU system, we developed a tissue mimicking thermochromic phantom that is capable of permanent color change for temperatures greater than 63°C. Finally, this dissertation also demonstrates the applicability of HIFU ablation in treating patients suffering from osteoid osteoma, while highlighting the issues with current clinical system, and adjustments that could be made using the existing clinical HIFU system to treat patients with solid tumors in the limbs.

Bioeffects resulting BH sonications regimes produced using a clinical MR-HIFU system were investigated in tissue mimicking phantoms and three different *ex vivo* porcine tissue types. Characterization of lesion type and structure relative to achieved temperature is vital in distinguishing and deconvoluting thermal bioeffects from intermixed mechanical bioeffects when utilizing long HIFU pulsing regimes. In order to understand the sonication parameter-dependent bioeffects and lesion characteristics, sonication parameters were modified such as acoustic power, PRF, number of cycles/pulse, and total sonication time. In addition, MRI thermometry allowed quantification of the area of temperature > 45°C, area of thermal dose > 240 CEM43, and

T2 relaxation time. Findings from this study suggest mechanisms that may be modulated for non-invasive oncology therapies. Pulsed-HIFU sonications can produce varying lesion types in different tissues, and a clinical MRI system can differentiate the resulting mechanically fractionated from unfractionated regions. This work may inform the selection of sonication parameters to produce controllable thermal and mechanical bioeffects in liver, kidney, and cardiac muscle, and facilitate clinical exploration of this HIFU technique.

In addition, the success of thermoablative therapies depends on precise spatial targeting and controlled temperature elevation within target tissues. In addition, adjacent tissues and organs at risk (OAR) can be over heated or even ablated. Depending on the tumor volume, anatomical location and pathology, the organ of interest and surrounding tissues may be under treated or result in unnecessary ablation. Another issue is the ability of an extracorporeal HIFU transducer to access and successfully treat retroperitoneal tumors. HIFU thermal ablation has required MRI thermometry for sonication parameter optimization, assessment of targeting accuracy, and assurance of appropriate temperature elevation for coagulative necrosis. Temperature probes proximal to the HIFU focal zone have been used for ultrasound-guided HIFU applications. However, given the 3D nature of the focal acoustic pressure field and frequent utilization of volumetric heating concepts such as electronic steering of the focal point, the accuracy of volumetric temperature estimates depends on the number of probes and their location. Lack of MRI thermometry feedback while using ultrasound image-guided HIFU systems, may lead to damage to adjacent OAR's, leading to potentially significant iatrogenic effects. This thesis presents a novel tissue mimicking thermochromic phantom, which can be used to assess temperature by direct and permanent color change. The performance of this tissue mimicking phantom is characterized on two different HIFU systems. Post-HIFU TMTCP color changes were correlated with MRI thermometry and T2 maps, demonstrating the applicability of TMTCP in MR-HIFU use. This TMTCP facilitates characterization of HIFU devices, sonication parameters, and heating protocols without the need for real-time MRI or thermocouple-based thermometry. The

Chapter 7

HIFU-optimized TMTCP can provide quantitative information on absolute temperatures, ablation volume geometry, temperature uniformity, and spatial targeting accuracy, based on TMTCP color and/or T2 change. Consequently, the TMTCP can be used to evaluate HIFU device- and sonication parameter-specific heating characteristics in a controlled, predictable, and spatially uniform environment through simple visual or computational methods. Although yet to be demonstrated, such methodologies may have important training and treatment planning implications as well.

Guided by results of our experiments using BH in tissue mimicking phantoms and *ex vivo* tissues, we selected BH sonication parameter set that produced complete tissue fractionation with sharp boundaries and minimal heating to surrounding areas. This sonication parameter set was used in murine neuroblastoma tumor treatment, described in chapter 5. We demonstrated that partial tumor fractionation using BH in combination with α CTLA-4 + α PD-L1 results in abscopal effect and significantly prolongs survival in previously untreatable, large unilateral and bilateral refractory murine neuroblastoma tumors. We also reveal that this anti-tumor effect is mediated by up regulation of dendritic cells, tumor infiltrating T-cells, proinflammatory cytokines, and DAMP's, while concurrent downregulation of pro-tumor regulators such as Foxp3, IL-10 and VEGF-A. Furthermore, this combination therapy elicits a systemic effector memory response that results in rejection of tumor re-challenge and can be adoptively transferred. The key result of partial tumor fractionation using BH of refractory murine neuroblastoma tumors is enhancement of innate and adaptive cellular immunity, converting a 'cold' non-immunogenic tumor to a 'hot' immunogenic tumor.

Even with our encouraging results, some key technical and immunological issues need to be addressed. Firstly, it would be valuable to assess the role of priming the immune system with α CTLA-4 or PD-1 prior to BH, followed by α PD-L1 in evaluating the role of these T-cell priming and activation while reducing the potential effects of co-toxicity. Secondly, assessing the role of specific T-cell phenotypes after HIFU and in combination with checkpoint inhibitors may help

support outcomes observed in this study. Third, we treated ~2% of tumor volume. It may be interesting to assess the effect of tumor volumes in survival outcomes, and established an 'exposure-response' relationship. Finally, assessing the scalability of this technology solely rests on testing it in multiple murine models of pediatric and adult tumors for systemic immune response and survival benefit.

In conclusion, improving and tailoring HIFU energy delivery to noninvasively treat children with solid tumors by creating a systemic anti-tumor immune response, is paradigm shifting and could benefit patients who are not responding to other treatment options. When combined with immunotherapy, HIFU has demonstrated significant benefit in overall survival in mice. Once HIFU treatment scalability is addressed, it could potentially lead to sponsored clinical trials for patients with neuroblastoma and other solid tumors in combination with immunotherapy.

Review Committee

Prof. Dr. Jürgen Kuball (Chairman)

Professor and Chair

Department of Hematology,

Laboratory for Translational Immunology (LTI), Department of Medical Oncology

Utrecht Cancer Center, University Medical Center Utrecht, the Netherlands

Dr. Stefan Nierkens

Associate Professor and Chair

Utrecht center for Diagnostic Advances in Immunology Research (U-DAIR),

University Medical Center Utrecht & Princess Máxima Center for Pediatric Oncology, the Netherlands

Prof. Dr. Bas.W. Raaymakers

Professor

Experimental Clinical Physics Radiotherapy,

University Medical Center Utrecht, the Netherlands

Prof. Dr. Peter. R. Luijten

Professor

Functional Medical Imaging,

University Medical Center Utrecht, the Netherlands

Prof. Dr. Nico de Jong

Professor and Chair

Acoustical Wavefield Imaging,

Technical University of Delft, the Netherlands

Molecular Ultrasonic Imaging and Therapy,

Erasmus MC, the Netherlands

Acknowledgements

The work presented herein is based on research performed at Children's National Medical Center, in collaboration with National Institutes of Health, and University Medical Center Utrecht. This would not be possible without several people involved directly or indirectly in this thesis work.

I would like to express my sincere thanks to Dr.Chrit. T. W. Moonen for permitting to work with is group at UMC Utrecht, and spending time with me throughout my Ph.D to review results and bounce ideas. Your vision, guidance, and wisdom has helped shape my ideas. You continue to be a role model to many of us. My best wishes to you in bringing your HIFU ideas to the clinic.

I would also like to thank Dr.Mario. G. Ries for investing a significant amount of time to discuss ideas, review results, mentoring me, while helping me stay on track towards my Ph.D program. Mario, I will always be thankful, and look up to your hands-on approach in doing science.

My sincere thanks to Dr.Bradford. J. Wood for allowing me to work in his lab for the last 6 years. I am truly grateful for the time you spent with in reviewing my ideas, guiding me, and focus my ideas that can directly help patients in the clinic. I look up to your energy and ability to multitask.

Dr.Peter C.W. Kim, I will always be thankful to you for letting me work with your group and at NIH, and UMC. I have learnt a significant number of things from you, and have always be indebted to letting me walk in to your office and discuss data, ideas or issues, and teaching me write. Thank you for helping me stay clear of obstacles, and allowing me to focus on what mattered the most.

I also express my sincere gratitude to my lab mates, coauthors, and group members at Children's National (IGNITE) and National Institutes of Health (CIC). This work would not be possible without your support, and advice. I also thank you guys for all the discussions we have had over the years.

I am also blessed to have great friends and colleagues. Emmanuel Wilson, Ozgur Guler, Navid Farr, Ari Partanen, Ayele Negussie, Andrew Mikhail, Justin Opfermann, amongst several others: Thank you for your never ending patience, support, and all the good times. Would not be possible to complete this work without your help.

Beyond everything, I will always be grateful to my parents, Janaki and Prakasa Rao, for supporting me all my life, and providing unconditional love and encouragement. Thank you for believing in me. Big thanks to my sister, Manasa for all the support over the years.

To my beloved wife Asha: None of this would be possible without you. Your patience, love, support and positivity has helped me stay motivated, and work towards achieving my goals including finishing my thesis. Thank you for everything you do for me.

Publications

1. **Eranki, Avinash**, Navid Farr, Ari Partanen, Karun V. Sharma, Hong Chen, Christopher T. Rossi, Satya VVN Kothapalli et al. "Boiling histotripsy lesion characterization on a clinical magnetic resonance imaging-guided high intensity focused ultrasound system." *PloS one* 12, no. 3 (2017): e0173867.
2. **Eranki, Avinash**, Navid Farr, Ari Partanen, Karun V. Sharma, Christopher T. Rossi, Avi Z. Rosenberg, AeRang Kim et al. "Mechanical fractionation of tissues using microsecond-long HIFU pulses on a clinical MR-HIFU system." *International Journal of Hyperthermia* 34, no. 8 (2018): 1213-1224.
3. **Eranki, Avinash**, Andrew S. Mikhail, Ayele H. Negussie, Prateek S. Katti, Bradford J. Wood, and Ari Partanen. "Tissue-mimicking thermochromic phantom for characterization of HIFU devices and applications." *International Journal of Hyperthermia* 36, no. 1 (2019): 518-529.
4. **Eranki Avinash**, Priya Srinivasan, Mario Ries, AeRang Kim, Christopher A.Lazarski, Christopher T.Rossi, Tatiana D.Khokhlova, Emmanuel Wilson, Susan M.Knoblach, Karun V.Sharma, Bradford J.Wood, Chrit T.W.Moonen, Anthony D.Sandler, and Peter C.W.Kim. "Immune Sensitization and Therapeutic Impact in Refractory Murine Neuroblastoma by High Intensity Focused Ultrasound" *Clinical Cancer Research* (2019, in press).
5. Pavel S.Yarmolenko, **Avinash Eranki**, Ari Partanen, Haydar Celik, AeRang Kim, Matthew Oetgen, Viktoriya Beskin et al. "Technical aspects of osteoid osteoma ablation in children using MR-guided high intensity focused ultrasound." *International Journal of Hyperthermia* 34, no. 1 (2018): 49-58.

Author Biography



Avinash Eranki completed his Bachelor of Engineering in Electronics and Communication in 2007 from Visveswariah Technological University, Bangalore, India. He went on to receive his Master of Science degree in Electrical Engineering from George Mason University, Virginia, USA, with a thesis titled 'Measurement of Musculoskeletal Motion Using Vector Tissue Doppler Imaging', in 2011. He started working at Children's National Medical Center, Washington, DC, USA, and at National Institutes of Health, Bethesda, Maryland, USA as a Senior Research & Development Staff Engineer in 2014. He worked with Dr.Peter C.W.Kim, and, Dr.Bradford J.Wood on developing and translating novel High Intensity Focused Ultrasound (HIFU) techniques to treat pediatric and adult solid tumors non-invasively. While employed at Children's National and National Institutes of Health, he started pursuing his PhD degree in Medical Imaging in the Image-Guided Focused Ultrasound group of the University Medical Center Utrecht, under the guidance of Prof.Dr.Chrit T.W.Moonen, Dr.Mario G.Ries, Dr.Bradford J.Wood, and Dr.Peter C.W.Kim. The work presented in this dissertation is the outcome of a productive collaboration between UMC Utrecht, Children's National Medical Center and National Institutes of Health.

